Title
Multiscale Crystal Defect Dynamics: A Crystal Plasticity Theory Based on Dislocation Pattern Dynamics

Author
LYU, DANDAN

Publication Date
2018

Peer reviewed|Thesis/dissertation

Multiscale Crystal Defect Dynamics: A Crystal Plasticity Theory Based on Dislocation Pattern Dynamics

by

Dandan Lyu

A dissertation submitted in partial satisfaction of the

requirements for the degree of

Doctor of Philosophy

in

Engineering – Civil and Environmental Engineering

in the

Graduate Division

of the

University of California, Berkeley

Committee in charge:

Professor Shaofan Li, Chair
Professor Francisco Armero
Professor Per-Olof Persson

Spring 2018

Multiscale Crystal Defect Dynamics: A Crystal Plasticity Theory Based on Dislocation Pattern Dynamics

Abstract

Multiscale Crystal Defect Dynamics: A Crystal Plasticity Theory Based on Dislocation Pattern Dynamics

by

Dandan Lyu

Doctor of Philosophy in Engineering – Civil and Environmental Engineering

University of California, Berkeley

Professor Shaofan Li, Chair

Understanding the mechanism of plasticity is of great significance in material science, structure design as well as manufacture. For example, the mechanism of fatigue, one critical origin for mechanical failures, is governed by plastic deformation. In terms of simulating plasticity, multiscale methods have drawn a lot of attention by bridging simulations at different scales and yielding high-quality atomistic properties at affordable computational resources. The main limitation of some multiscale methods is that the accuracy in much of the continuum region is inherently limited to the accuracy of the coarse-scale model, even though much effort has been made to improve the existing multiscale models by developing adaptive refinement models. It is known that crystal defects play an important role in determining material properties at macroscale. Crystal defects have microstructure, and this microstructure should be related to the microstructure of the original crystal. Hence each type of crystals may have similar defects due to the same failure mechanism originated from the same microstructure, if they are under the same loading conditions. In this dissertation, a multiscale crystal defect dynamics (MCDD) model is proposed that modelling defects by considering their intrinsic microstructure derived from the microstructure or dislocation patterns of the original perfect crystal. The main novelties of present work are: (1) the discrete exterior calculus and algebraic topology theory are used to construct a scale-up (coarse-grained) dual lattice model for crystal defects, which may represent all possible defect modes inside a crystal; (2) a higher order Cauchy-Born rule (up to the fourth order) is adopted to construct atomistic-informed constitutive relations for various defect process zones, and (3) an hierarchical strain gradient theory based finite element formulation is developed to support an hierarchical multiscale process zone model for various defects in a unified formulation. The efficiency of MCDD computational algorithm allows us to simulate dynamic defect evolution at large scale while taking into account atomistic interaction. The MCDD model has been validated by comparing the results of MCDD simulations with that of molecular dynamics (MD) in the cases of nanoindentation, uniaxial tension and simple shear. Numerical simulations have shown that MCDD can capture not only material failure but also inelastic deformation in a multiscale

continuum simulation by considering the atomistic interaction. In addition, simulation of anisotropy demonstrates that MCDD is capable of capturing the influence of loading axis orientation and the loading directionality on dislocation nucleation.

To my family

Contents

Contents **ii**

List of Figures **iv**

List of Tables **vii**

1 Introduction **1**
1.1 Motivation and Background 1
1.2 Overview of the Dissertation 4

2 Dislocation Pattern Dynamics **6**
2.1 Experimental Observation of Dislocation Patterns 7
2.2 Molecular Dynamics Simulation of Dislocation Patterns 8
2.3 Dislocation Dynamics Simulation of Dislocation Patterns 10

3 Discrete Exterior Calculus and Non-Bravais Super Lattice **11**
3.1 Cell Complexes of a Crystal Lattice 11
3.2 Dual Lattice Complex 14
3.3 Discrete Crystal Defect Model–a Non-Bravais Super Lattice 16
3.4 Discrete Crystal Defect Model for FCC and BCC crystals 18

4 Dislocation Patterns of BCC and FCC Crystals **32**
4.1 Comparison of Dislocation Patterns in Relaxation System 32
4.2 Comparison of Dislocation Patterns with Experiments 33

5 Multiscale Constitutive Modelling **35**
5.1 Higher-order Cauchy-Born Rules 35
5.2 Multiscale Constitutive Models 38

6 Finite Element Formulation **41**
6.1 Multiscale Finite Element Formulation 41
6.2 Implementation of Third Order Process Zone Element: Rhombic Dodecahedron 45
6.3 Size of Dodecahedron Element 46

7 Numerical Analysis **48**
7.1 Crack Propagation 48
7.2 Uniaxial Deformation and Simple Shear 54
7.3 Nanoindentation in Copper 58
7.4 Crystal Slip and Dislocation Nucleation around a Void 64
7.5 Crystal Orientation Effects on Dislocation Nucleation at Grain Scale 67
7.6 Shear Band Formulation with Uniaxial Loading 69

8 Conclusions and Outlook **71**

Bibliography **74**

A Derivatives of the Six-node Honeycomb Wachspress Shape Function **83**

B Derivatives of Shape Functions **87**
B.1 The First Order Derivative of Shape Functions 87
B.2 The Second Order Derivative of Shape Functions 87
B.3 The Third Order Derivative of Shape Functions 88

C Finite Element Interpolation Functions for Rhombic Dodecahedron **89**

List of Figures

1.1 (a) Spoon bent when scooping hard ice cream and (b) plastic deformation. . . . 1
1.2 Different scales in plasticity modelling. 2
1.3 Slip planes for different types of crystal: (a) {111} slip plane in FCC crystal, (b) {110} slip plane in BCC crystal, and (c){0001} slip plane in HCP crystal. . . . 3

2.1 Schematic demonstration of the relation between axial orientation and dislocation pattern structure after deformation at (a) 5×10^{-4} and (b)5×10^{-3}[56]. (Reuse permission by Elsevier: License Number 4321590270613) 7
2.2 Formation illustration of various wall structures: (a)(b) DB-wall, (c)(d) labyrinth-wall, and (e)(f) cell-wall[55]. (Reuse permission by Elsevier: License Number 4321590556083) 8
2.3 (a)TEM picture of junction network at their intersections [59] and (b)a similar junction network by atomistic simulation[63]. (Reuse permission by APS: License Number RNP/18/APR/002932) 9
2.4 Dislocation patterns in (a) the Cu-Ni interface, (b) the twisted Cu-Ni interface, (c) the strained Cu-Ag interface, and (d)Cu-Ag interface[64]. (Reuse permission by Elsevier: License Number 4321601337651) 9
2.5 (a)Dislocation patterns from the Edge-Screw model, (b) resistive internal shear stresses in active slip plane, and (c) positive internal stresses on the same slip plane[76]. (Reuse permission by Elsevier: License Number 4323801067330) . . . 10

3.1 (a) Lattice complex of hexagonal (triangle) lattices, (b) its corresponding dual lattice complex, (c) the non-Bravais super lattice complex, and (d) the scaled lattice complex. 15
3.2 Lattice complex representation of BCC lattice and indexing scheme: (a) the primal BCC lattice basis, (b) the Wigner-Seitz cell of BCC crystal lattice–a truncated octahedron cell at the lattice site l, and (c)the formation of non-Bravais motif at sites of a super BCC lattice site. 19
3.3 BCC super lattice mesh and polytopal elements. 20
3.4 Lattice complex representation of the BCC lattice and indexing scheme: (a) 2^{nd} order process zone elements and (b)prism element 5. 21
3.5 Polytopal lattice complex representation of wedge elements. 22

3.6 Lattice complex representation of the BCC lattice and indexing scheme: (a)1^{st} order process zone elements and (b) wedge element 1. 23
3.7 Lattice complex representation of the BCC lattice and indexing scheme: 0^{th} order process zone elements. 24
3.8 Lattice complex representation of the BCC lattice and indexing scheme for the bulk element. 24
3.9 Lattice complex representation of the FCC lattice and indexing scheme: (a) FCC lattice basis vectors, (b) dual cell complex of $\sigma^0(l)$ (3^{rd} order process zone element), and (c) non-Bravais basis of FCC super lattice. 26
3.10 Lattice complex representation of the FCC lattice and indexing scheme: (a)2^{nd} order process zone elements and (b)prism element 11. 27
3.11 Lattice complex representation of the FCC lattice and indexing scheme: (a)1^{st} order process zone elements and (b)wedge element 1. 28
3.12 Lattice complex representation of the FCC lattice and indexing scheme for the wedge element. 29
3.13 Lattice complex representation of the FCC lattice and indexing scheme: 0^{th} order process zone elements. 30
3.14 Lattice complex representation of the FCC lattice and indexing scheme for the bulk element. 30
3.15 Construction process of FCC mesh. 31

4.1 Dislocation patterns of (a) FCC Cu and (b) BCC Mo, the colorbar is based on coordinate number and perfectly coordinated atoms are removed. (c) and (d)the corresponding mesh of MCDD. 33
4.2 Comparison of formation mechanisms of different dislocation patterns in different orientations[56, 49]. 34
4.3 Comparison of formation mechanisms of different wall structures in different orientations[55]. 34

5.1 FCC super lattice mesh. 35

6.1 FEM shape function of rhombic dodecahedron element with mean value coordinates: (a)overall view and (b)representation of tetrahedron. 45
6.2 Setup of 1D wave propagation model. 46
6.3 Wave shape before reflection at fixed boundary. 47
6.4 Wave shape after reflection after fixed boundary. 47

7.1 Schematic illustration of 2D plate and multiscale process zone mesh. 48
7.2 The process of process zone tiling: (1) yellow region: the 0-th order process zone, (2) blue region: the 1st process zone, and (3) green region: the 2nd process zone. 49
7.3 The Washspress shape function for the honeycomb element. 51
7.4 Schematic illustration of the quadrature rule for the regular hexagonal element. 52
7.5 Stress distributions in a crack propagation sequence. 53

7.6 Crack speed comparison between MCDD model and molecular dynamics. 54
7.7 A simple benchmark test of uniaxial stretch: (a) finite element mesh of MCDD specimen and (b) initial atom configuration of the MD cell. 55
7.8 (a) Comparison of the simulated stress-strain relations obtained from MCDD and MD under the uniaxial loading and unloading condition and (b) stress-strain relations at different strain rates from MCDD. 55
7.9 Comparison of the simulated stress-strain relations obtained from MCDD and MD under the uniaxial loading and different unloading strain: (a) unloading at 10 % relative strain, (b) unloading at 12 % relative strain, (c) unloading at 15 % relative strain, and (d) unloading at 18 % relative strain. 56
7.10 A benchmark test of simple shear: (a) finite element mesh of MCDD specimen and (b) initial atom configuration of the MD cell. 57
7.11 (a) Comparison of strain-stress curve of shear with MD and MCDD and(b) strain-stress curve of shear loop. 57
7.12 MCDD nanoindentation simulation: (a) MCDD simulation set-up and (b) configuration of the MD simulation. 58
7.13 Schematic of the coarse-grained contact model between rigid sphere and deformable domain. 61
7.14 MCDD simulation results: dislocation loop (blue) and stacking fault (green) formation in the copper substrate during the indentation. 62
7.15 Formation and movement of dislocation loops and crystal slips beneath the indenter. 63
7.16 Comparison of load-displacement curves obtained from MCDD and MD simulations of nanoindentation in copper. 64
7.17 Schematic of single crystal copper specimen: (a)the view of uniaxial tension and (b) half mesh with a rhombohedral void. 65
7.18 MCDD simulation results: (a) slip planes and (b) dislocation loops in the copper specimen. 66
7.19 Load-displacement curve of uniaxial tension of a copper specimen with an inside void. 66
7.20 Stereographic triangle showing the 29 crystallographic orientations. Each direction represents the uniaxial loading axis for single crystal deformation simulation. 67
7.21 Comparison of contour plots of tensile stress, compressive stress and the ratio of compressive stress and tensile stress: (a)results of MCDD and (b) MD results[107]. (Reuse permission by AIP Publishing LLC: License Number 4324321505819) 68
7.22 (a)Mesh of column and (b)strain-stress curve with uniaxial loading. 69
7.23 Formulation process of shear band in (111) plane with strain (a) 2%, (b)15%, (c)15%, and (d)25%. 70

List of Tables

7.1 Material parameters for copper 51
7.2 Material parameters of EAM-Mishin for copper[100] 60

C.1 Coordinates of 14 nodes in the reference coordinates 90

Acknowledgments

I would like to express my gratitude to Professor Shaofan Li for his guidance and support. His patience and inspiration help me on every step I need to make and overcome the difficulties in research as well as in life. I am grateful for having such a wise and caring person as my advisor and been working with him in our friendly group.

I owe my special thanks to Professor F. Armero and Professor P. Persson for serving on my thesis committee. The solid mechanics courses I took from Professor F. Armero and numerical analysis courses from Professor P. Persson have provided me the theoretical foundation and mathematical implementation skills for my research.

I would like to thank my colleagues Houfu Fan, Qi Tong, Qingsong Tu, Chunxiang Shi, Tiange Li and Yuxi Xie among others for their help and kindness, which gave me many happy memories of Berkeley.

I am grateful to my parents for supporting and encouraging me in all aspects. I find myself always be able to draw strength from their strong sense of responsibility towards family. I owe my thanks to my younger brother for sharing the responsibility of our family when I was away from home.

I dedicate this dissertation to my husband, Runze for his love and the happiness we share in our small family.

Chapter 1

Introduction

1.1 Motivation and Background

A metal spoon will keep its original shape under normal conditions of use. But when scooping hard ice cream as shown in Fig. 1.1(a), the spoon may be deformed too far to recover[1], which is called plasticity. The metal spoon consists of many crystalline grains and atoms are arranged in a regular array inside each grain. In order to bend the spoon permanently, atomic slip planes must slide past each other shown in Fig. 1.1(b). Strategies for understanding and modelling the plastic deformation are the topics of this dissertation.

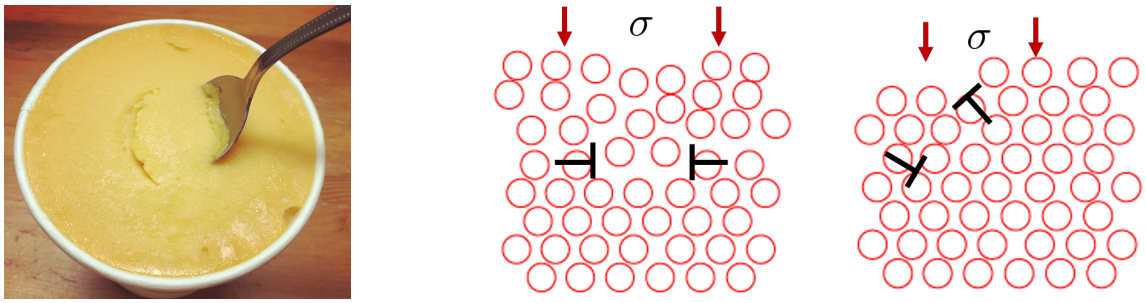

(a) (b)

Figure 1.1: (a) Spoon bent when scooping hard ice cream and (b) plastic deformation.

Many books and articles suggeste that 50% to 90% of mechanical failures are caused by fatigue(e.g. [2]), whose mechanism is governed by plastic deformation. Hence, in order to design better fatigue resistant materials and structures, we need to understand the mechanism of plasticity. In addition, both bulk-forming and sheet forming in the manufacturing processes involve plastic deformation[3]. Therefore, plasticity needs to be understood in the manufacturing processes design.
In terms of simulating plasticity, the most accurate method would be first principle-based

methods [4, 5, 6, 7] or molecular dynamics [8, 9, 10], because they can yield high-quality atomistic properties of a material without fitting parameters. However, they are way too expensive even if the most powerful computers available today are used. Another possible approach is to use the multiscale method (Fig. 1.2), which can bridge simulation at different scales and overcome the problem of lacking computation resources[11, 12, 13, 14, 15].

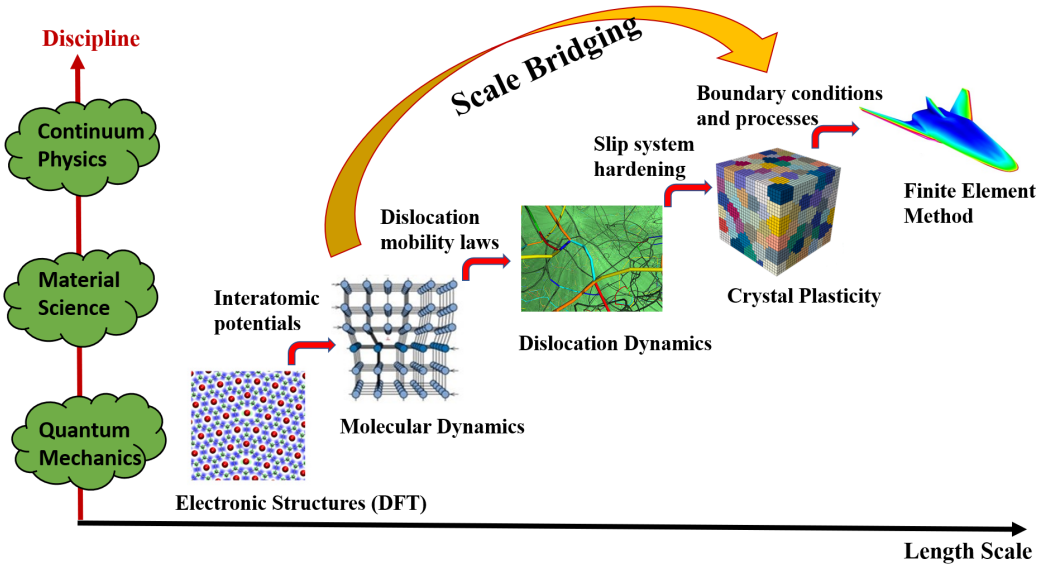

Figure 1.2: Different scales in plasticity modelling.

In general, multiscale method may be classified into two categories: sequential and concurrent. Sequential multiscale methods treat fine-scale simulations as a pre-processing step to the coarse-scale model. Then parameters or description from fine-scale simulation are passed to coarse-scale model. Such approaches usually use the fine-scale to derive the special form of the governing equations at the coarse-scale and lead to deep physical insight into the coarse-scale behaviors [16, 17, 18]. On the contrary, concurrent multiscale methods couple models at two or more scales simultaneously. Usually the physical problem is divided into two or more contiguous regions and each region is modelled at one distinct scale. There are several concurrent multiscale methods for modelling plasticity that employ domain decomposition, such as the coupled atomistic and discrete dislocation [19, 20, 21, 22, 23]. A critical issue in these domain decomposition methods is how to exchange information between the domains across an interface. In particular, it has been a challenge to pass the dislocation lines in the fine scale region across the multiscale interface to the continuum region in 3D simulations. On the other hand, the main shortcoming of some of the multiscale methods mentioned above is that the accuracy in much of the continuum region is inherently limited

to the accuracy of the coarse-scale model, even though much effort has been made to improve the existing multiscale models by developing adaptive refinement models.
Crystal defects play an important role in determining material properties at macroscale. For example, dislocations are the origin of metal plasticity; voids can pin down dislocations, and thus play a vital role in work-hardening plastic deformation. The macro-scale material behaviors are essentially determined by the microstructure of the material itself as well as the corresponding microstructure of the defects. To predict the overall material behaviors through the simulation of aggregated defect motion or evolution has been a long-standing challenge in mechanics of materials and materials science. In crystalline solid, there are a few types of lattice defects, namely dislocation, void, disclination, crystal slip(Fig. 1.3), and cracks.

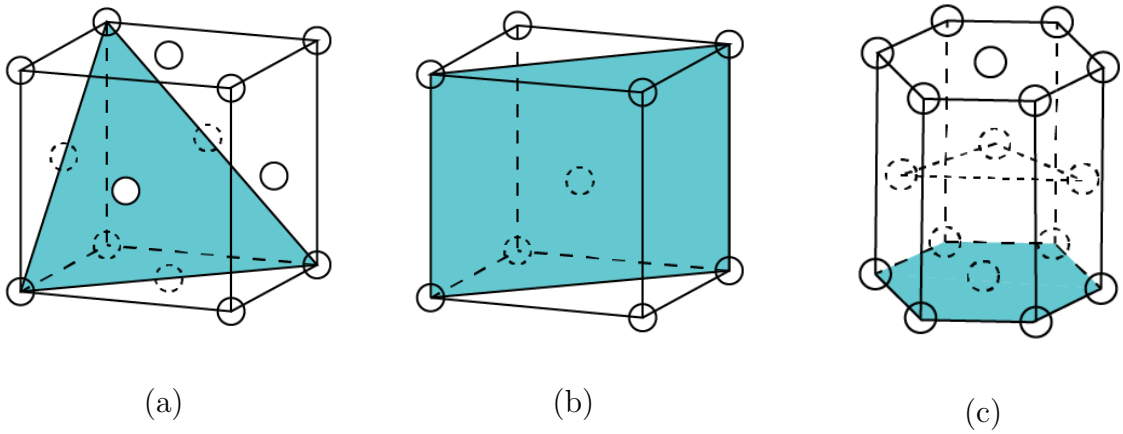

(a) (b) (c)

Figure 1.3: Slip planes for different types of crystal: (a) {111} slip plane in FCC crystal, (b) {110} slip plane in BCC crystal, and (c){0001} slip plane in HCP crystal.

Conventionally, various lower dimension geometric models, such as idealized surface(2D), line(1D), and vertex(0D) models are adopted to represent defects in crystalline solids. Discrete dislocation dynamics [24, 25] are examples of such approach. A recent example is the discrete mechanics of crystal lattice developed in [26], in which the defects are again treated as lower dimensional objects of lattice complex. For example the void is idealized as the point defect (0-cell), dislocation is idealized as the line defect (1-cell), and crystal slip is idealized as surface defect (2-cell)[27]. However, the inherent disadvantages in the lower dimensional idealization are: (1) it may unintentionally neglect the three-dimensional microstructure of the defects, which is crucial for defect interactions; (2) the lower dimensional defect model is valid only at atomistic scale so that the model has the limitation in scalability; (3) the related defect model has no length scale and thus fails to provide statistical insights and relevance to the original physical problems, and (4) most importantly, it needs ad-hoc and prescribed failure criteria such as interface cohesive law or dislocation mobility law to simulate defect evolutions, which may not be consistent with first-principle atomistic theory.

1.2 Overview of the Dissertation

The aim of this work is to construct a coarse-grained defect model for crystalline materials. Therefore, instead of using differential topology to analyze perfect crystal lattice complex, we are using the differential calculus to analyze the dual lattice, or more precisely, a non-Bravais super lattice, which may represent the microstructure of the defects. By doing so, we have developed a framework of hierarchical multiscale method in defect mechanics, where the term defect refers to disorder or damage state of lattice structure, such as voids, dislocations, slip planes or faults, and cracks. The theoretical formulation of the proposed method follows the construction of a multiscale process zone model developed by the present authors [28, 29, 30, 31, 27, 32, 33]. In present work, by extending the discrete crystal lattice developed in [26] into a non-Bravais super lattice, we have demonstrated how to systematically and rigorously construct a scalable multiscale defect mechanics model based on the microstructure of the original perfect crystal lattice, and it provides the mathematical and physical foundation for crystal defect dynamics.

Chapter 1 is the motivation and background of the dissertation. The phenomenon of plastic deformation is introduced with its significance in fatigue and manufacturing process. Then the limitations of numerical models both at single scale and multiscale are discussed. In order to address these problems, a different approach, multiscale crystal defect dynamics, is proposed to predict the overall material behaviors through the simulation of aggregated defect motion.

Chapter 2 gives a basic description of experimental observation and dislocation microstructure simulation, especially focuses on the mechanism towards plastic deformation, which lay the theoretical foundation for the proposal of multiscale crystal defect dynamic model.

In chapter 3, we shall first briefly outline the basic theory of discrete differential calculus that is needed to describe crystal lattices, and then we discuss how to construct the super lattice or the discrete crystal defect model via discrete exterior calculus formulation. The process of how to build the discrete crystal defect model for BCC and FCC crystals are discussed in detail.

An atomistic-informed strain gradient theory for different orders of process zones to model different types of defects in crystals are present in chapter 4. Specifically, the concepts of higher-order Cauchy-Born rules are discussed and different stress measures are derived based on embedded atom method(EAM) potential.

In chapter 5, the formulation and implementation of the multiscale finite element formulation based on the proposed multiscale crystal defect dynamics (MCDD) theory are discussed. In particular, the shape functions of third order process zone element, rhombic dodecahedron are formulated. In addition, one critical parameter in MCDD modelling, the scale factor for super lattice complex and the size of the third-order process zone element is investigated by simulating 1D wave propagation in a long thin plate.

Numerical investigations of MCDD are performed in chapter 6. First, MCDD model is validated by comparing with the results of molecular dynamics (MD) for 3D nanoindentation, uniaxial loading and simple shear of single crystal copper. Meanwhile, MCDD is employed

to simulate dislocation motion and crystal slip around a void in a copper specimen. To demonstrate that MCDD is an atomistically-determinant crystal plasticity theory, MCDD is employed to simulate anisotropic plasticity at grain scale, and use it to study the influence of crystal orientation on dislocation nucleation and slip system activation. Last, the formulation of shear band in a copper specimen is simulated.

Chapter 7 summarizes the work in this dissertation with discussions. Comments and perspectives of MCDD model are also given.

Chapter 2

Dislocation Pattern Dynamics

This chapter gives a basic description of experimental observation and dislocation microstructure simulation, especially focuses on the mechanism towards plastic deformation, which lays the theoretical foundation for the proposal of multiscale crystal defect dynamic model.
Due to its significance in numerous technological problems, including issues in aerospace industry, the development of plasticity theory in terms of dislocation mechanics has attracted a lot of attention in materials science [34]. Dislocations produced in a deformed metal tend to aggregate into different types of dense formations separated by relatively dislocation free regions [35], which have significant influences in work hardening and localization of plastic deformation, and finally are linked to properties in macroscopic response. For example, work hardening in plastic deformation of a crystal is related to important changes in dislocation microstructure. The spontaneous emergence of areas with low dislocation density and those with high dislocation density is generally associated with the increase in dislocation density [36]. These metastable structures are called dislocation patterns, which tend to occur in single crystals, polycrystals, pure metals and alloys.
Understanding the mechanism of dislocation patterns is not only an interest in condensed matter solid state physics, but also has important applications in materials science and engineering. In general, relatively uniform dislocation occurs at the beginning of plastic deformation; Then the original distribution tends to be unstable as the increase of deformation. Finally 3D dislocation patterns can be aggregated into clusters [35]. This pattern may be unstable again and further transformed into more complicated restabilized state. Each of these stages are connected to one or more characteristic dislocation patterns.
A lot of research efforts have been focused to investigate the formation of dislocation patters [37, 38, 39, 40, 41, 42, 43, 44, 45, 46] during the past several decades. Both Experimental observation and theoretical modelling, ranging from molecular dynamics simulation, dislocation dynamics, to continuum and phase-field models are performed.

2.1 Experimental Observation of Dislocation Patterns

Dislocation patterns are highly ordered spatial structures associated with dislocation reactions and rearrangements[47, 48]. While they demonstrate various kinds of patterns, their common characristic is the spatial periodically ordered structure with the alternate appearance of dislocation-intensive and dislocation-free regions [47, 48]. Depending on the slip geometry, external loading and temperature, various patterns form (e.g. veins [49], persistent slip bands (PSB) [50], cells structures [51, 48], labyrinth as well as surface extrusions and intrusions [50]) emerge [52].

The crystal orientation has become one of the most important effects on dislocation patterns of crystalline materials. Current research has shown that for single crystals, such as copper, nickel or silver, as shown in Fig. 2.1, the dislocation patterns can be divided into three regions in the stereographic triangle(see Fig. 2.1(a)): the [011] region, the [001] region and the [$\bar{1}$11] region [53]. The common feature in the [011] region are the formation of PSB-wall structures. The common feature in the [001] region is that it tends to form labyrinth structure. While in the region of [$\bar{1}$11], the vein structure with low strain and the cell or wall structure with high strain are regarded as the most common dislocation patterns [54]. In addition, Fig. 2.2 shows the formation mechanism of three types of dislocation patterns, which are corresponding to the dislocation structures at different orientations. In general, the formation of dislocation patterns significantly relies on the active slip systems. The labyrinth structure is more likely to be observed on the condition that the critical secondary slip system is easier to operate. The cell structure is more easier to be seen with activating the coplanar secondary slip system. While the wall structure is more prone to appear without activating secondary slip system [55].

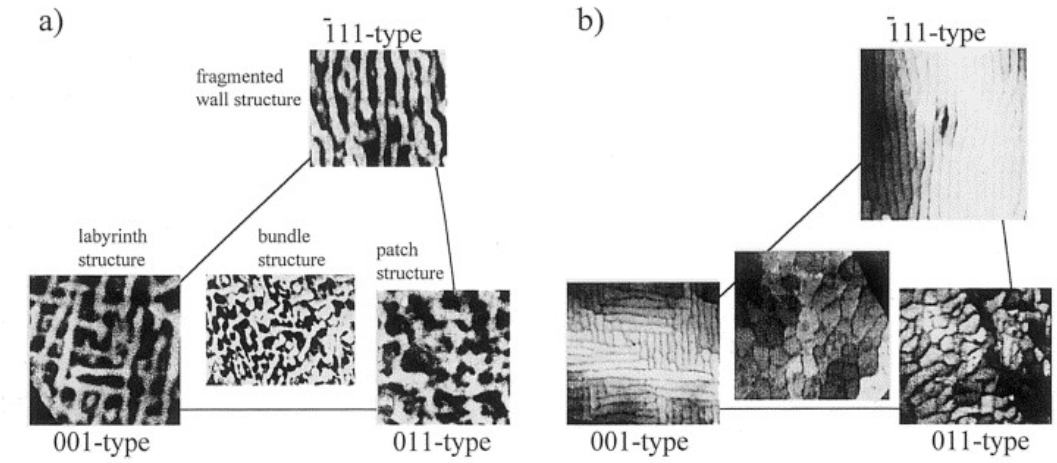

Figure 2.1: Schematic demonstration of the relation between axial orientation and dislocation pattern structure after deformation at (a) 5×10^{-4} and (b)5×10^{-3}[56]. (Reuse permission by Elsevier: License Number 4321590270613)

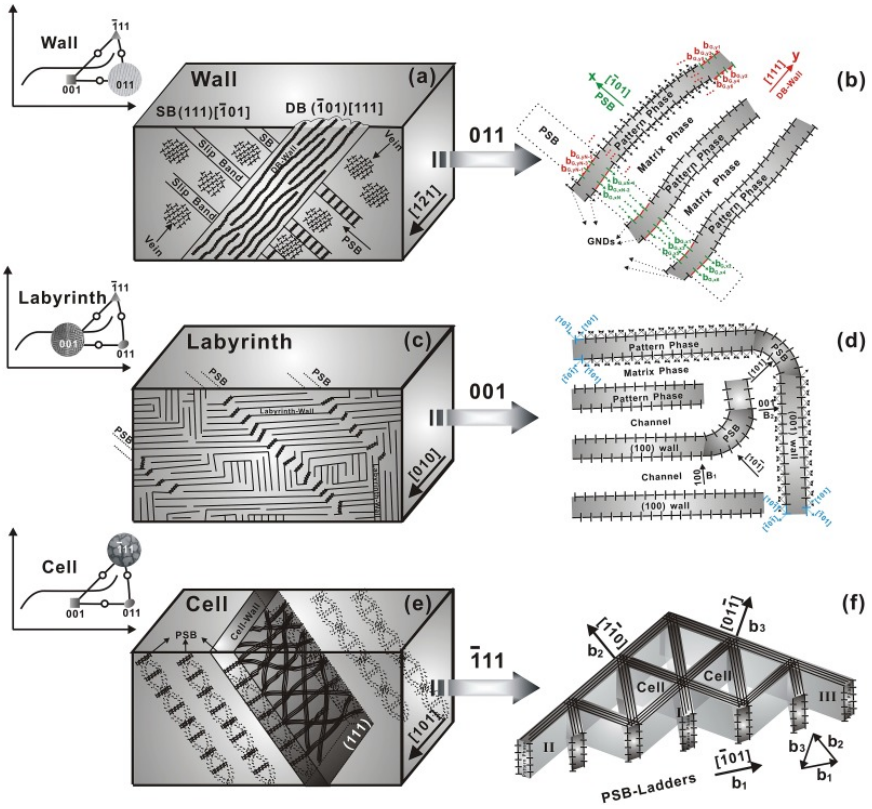

Figure 2.2: Formation illustration of various wall structures: (a)(b) DB-wall, (c)(d) labyrinth-wall, and (e)(f) cell-wall[55]. (Reuse permission by Elsevier: License Number 4321590556083)

2.2 Molecular Dynamics Simulation of Dislocation Patterns

Understanding the mechanisms and parameters of dislocation motion is key for the analysis of dislocation patterns and designing materials with improved properties [57, 58, 59]. Bulatov et al. [60, 61, 62, 63] adopted molecular dynamics to simulate dislocation mobility and the formation of dislocation network. Fig. 2.3 shows the comparison of junction network in TEM observation and dislocation dynamics simulation, as formed by the following dislocations:

$$\frac{1}{2}[111] + \frac{1}{2}[\bar{1}\bar{1}1] = [001] \tag{2.1}$$

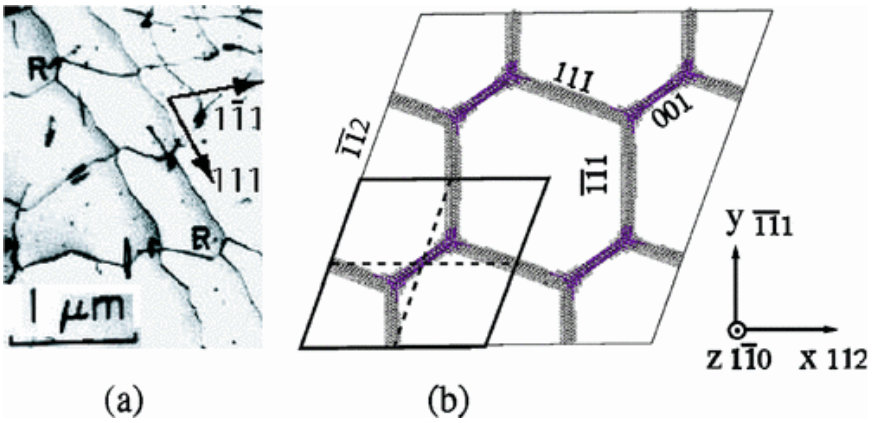

Figure 2.3: (a)TEM picture of junction network at their intersections [59] and (b)a similar junction network by atomistic simulation[63]. (Reuse permission by APS: License Number RNP/18/APR/002932)

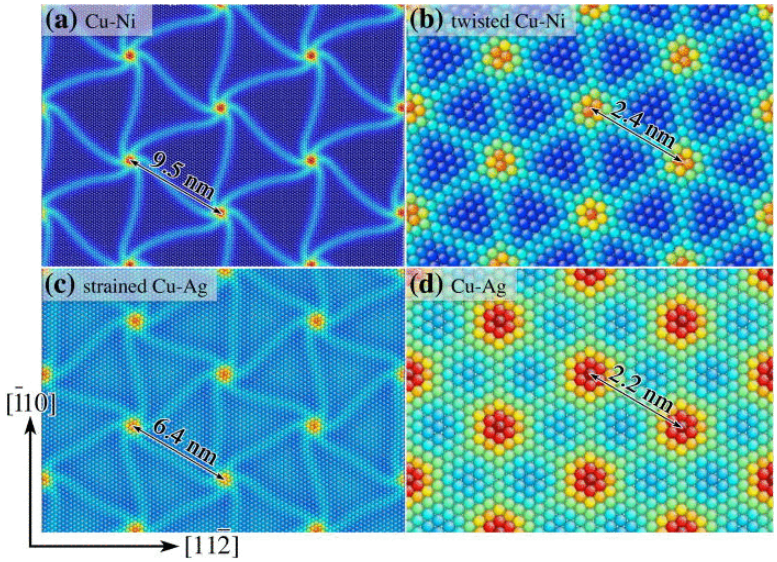

Figure 2.4: Dislocation patterns in (a) the Cu-Ni interface, (b) the twisted Cu-Ni interface, (c) the strained Cu-Ag interface, and (d)Cu-Ag interface[64]. (Reuse permission by Elsevier: License Number 4321601337651)

Shao et al. [65, 64, 66, 67] discussed the relaxation mechanisms, structure, and properties of semi-coherent interfaces based on atomistic simulations and dislocation theory, which can locate two stable structures and a high-energy structure by computing the generalized staking fault energy(GSFE) profile of the interface. Fig. 2.4 shows the misfit dislocation structures in the interface of Cu-Ni and Cu-Ag.

2.3 Dislocation Dynamics Simulation of Dislocation Patterns

Dislocation Dynamics (DD) is another popular direct approach that attempts to simulate the aggregate behavior of large dislocation ensembles at mesoscale by decomposing dislocation lines of arbitrary curvature and character into piecewise segments[68, 69, 70, 71, 72, 73, 74]. Kubin et al. [69] simulated the behaviours of collective dislocation structures by dislocation dynamics and can describe idealized situations in two dimensions, which may be useful in testing the effects on patterning of various properties or mechanism. Rhee et al. [75] developed a 3D dislocation dynamics model for short-range interactions, cross slip and long-range interactions of dislocation segments, which is capable of predicting macroscopic properties. Madec et al. [76] investigated the formation of patterned microstructures due to multiple slip in FCC crystals using dislocation dynamics, where cross-slip and short-range interactions have critical influences on the formation of dislocation patterns. Fig. 2.5 shows the simulated dislocation patterns in (1 1 1) foils of thickness 5 μm.

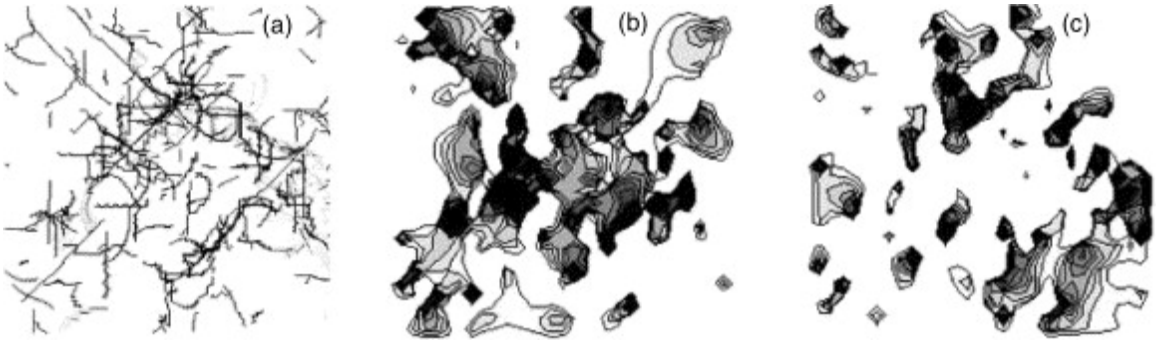

Figure 2.5: (a)Dislocation patterns from the Edge-Screw model, (b) resistive internal shear stresses in active slip plane, and (c) positive internal stresses on the same slip plane[76]. (Reuse permission by Elsevier: License Number 4323801067330)

However, the main limitation lies in that the characteristic length scale of dislocation patterns is an order of magnitude larger than the dislocation spacing [77, 68]. Therefore, quite large number of dislocation lines is needed in order to capture dislocation patterns in dislocation dynamics simulations, which is a rather hard task especially in 3D.
This chapter briefly summaries the dislocation patterns observed in experiments and modelled by molecular dynamics and dislocation dynamics, which gives the foundation for the proposed multiscale crystal defect dynamics model. In addition, the dislocation patterns provides evidence for the discrete calculus in the following chapters.

Chapter 3

Discrete Exterior Calculus and Non-Bravais Super Lattice

To make a consistent and self-contained presentation, in this chapter we first briefly introduce the basic definitions and notations of discrete exterior calculus notation, the elementary theory of chain complex of crystal lattice, and the concept of super lattice. The general topology structure of a lattice structure includes connections and connectivity among different geometric objects, such as edges, vertices, surfaces, and different order bulk elements may be described by using discrete differential topology. We shall mainly follow the notation and nomenclature of [78, 79, 80], and readers may consult them for further details. Since the application of discrete differential calculus to mechanics of materials is still at the stage of beginning, there is not a set of consented mathematical notations that are agreeable to both fields, in this dissertation we use the standard notations in both fields for convenience.

3.1 Cell Complexes of a Crystal Lattice

We first consider a set of $k+1$ linearly independent points, $\{v_0, v_1, \cdots, v_k\} \in \mathbb{R}^n, n > k$, that are called as vertices. The convex hull of these $k+1$ vertices

$$\sigma^k = \left\{ \mathbf{x} \in \mathbb{R}^n \;\middle|\; \mathbf{x} = \sum_{i=0}^{k} \mu^i v_i, \;\; with\ \mu^i \geq 0 \;\; and \;\; \sum_{i=0}^{k} \mu^i = 1 \right\} , \tag{3.1}$$

is defined as a k-simplex. We denote the boundary of σ^k as $\mathrm{B}d(\sigma^k)$, and the interior σ^k as $\mathrm{I}nt(\sigma^k) = \sigma^k \setminus \mathrm{B}d(\sigma^k)$. If σ^j is a proper face of σ^k, we write $\sigma^j \prec \sigma^k$. For example, a tetrahedron is a 3-simplex, a triangle is a 2-simplex, a line segment is a 1-simplex, a point is a 0-simplex, and the empty set is the unique (-1)-simplex. A face of a simplex is the convex hull of a subset of its vertices; in particular, a facet of a k-simplex is the convex hull of all but one of its vertices. Thus, every k-simplex has exactly $k+1$ facets and exactly $2k$ faces. Every face of a simplex is a simplex.

We then define the *G*eometric Simplicial Complex, or simplicial complex for short, as a set K of simplices in the Euclidean space $\mathbb{R}^n$, satisfying the following two conditions:
(1) Every face of a simplex of K is in K, and (2) The intersection of any two simplices of K is either a face of both of them, or it is empty.
The simplices in K are called the *c*ells.
In this work, we are interested in the so-called *P*olytopal Complex. Polytopal complexes (also called polyhedral complexes), which is a natural generalization of geometric simplicial complexes. Similar to the simplicial complex, a polyhedral complex is a set E of polytopes in the Euclidean space $\mathbb{R}^n, n > 0$, satisfying two conditions: (1) every face of a polytope in E is also in E, and (2) the intersection of any two polytopes in E is a face of both. The polytopes in E are called its cells. For example, the set of all faces of any convex polytope define a polytopal complex.
In general, both geometric simplicial complex and polytopal complex belong to a larger class of complexes — the CW complex. Roughly speaking, a CW complex is a Hausdorff space that can be partitioned into many open cells. The C stands for "closure-finite", and the W for "weak topology". In a CW complex, an open simplex, σ^k is homeomorphic to $\mathcal{B}^k$,

$$\mathcal{B}^k = \left\{ \mathbf{x} \in \mathbb{R}^k \;\middle|\; \|\mathbf{x}\|_2 \leq 1 \right\} . \Big\} \ . \tag{3.2}$$

Therefore we may also define a k-cell as:

Definition 3.1.1 *A k-cell, σ^k, is a topological space that is homeomorphic to the open k-unit ball i.e. int$(\mathcal{B}^p)$.*

In this work, we mainly consider polytopal cells in polytopal complex, which may be or may not be (geometrically) simplicial.
Before proceed further, we define the following operators

Definition 3.1.2 *The boundary operator is a homomorphism $\partial_k : \ C_k(K;\mathbb{Z}) \to C_{k-1}(K;\mathbb{Z})$, which is defined as follows,*

$$\partial_k \sigma^k = \partial_k([v_0, \cdots, v_k]) = \sum_{i=0}^{k} (-1)^i [v_0, \cdots, \hat{v}_i, \cdots v_k] \tag{3.3}$$

where $\sigma^k = [v_0, \cdots v_k]$ is a k-simplex, and $[v_0, \cdots, \hat{v}_i, \cdots v_k]$ is a (k-1)-simplex by omitting the vertex v_i.

Based on this definition, we have

$$\partial_k \sigma^k = \sum_{\sigma^{k-1} \prec \sigma^k} \pm \sigma^{k-1}, \tag{3.4}$$

where the sign is chosen as +(or -) if the orientation of σ^{k-1} coincides with or is the opposite to that induced by σ^k.
The above definition of boundary operator is for simplicial complexes. For polytopal complexes, some modifications may be needed.

Definition 3.1.3 *Consider a k-dimensional polytope P and $V(P)$ is the vertex set of of P. Let $\epsilon : \binom{V(P)}{k+1} \to \{-1, 0, 1\}$ be an orientation of P if the following subsequent conditions are satisfied:*

1. *$\epsilon(v_0, \cdots, v_k) = 0$ if and only of $v_0, \cdots, v_k$ are affinely dependent;*
2. *$\epsilon(v_0, \cdots, v_i', \cdots, v_k) = \epsilon(v_0, \cdots, v_i, \cdots .v_k)$ if v_i' and v_i are in the same open half-space of $\mathbb{R}^k$ delimited the hyperplane $v_0, \cdots, \hat{v}_i, \cdots v^k 0$ and $\epsilon(v_0, \cdots, v_i', \cdots, v_k) = -\epsilon(v_0, \cdots, v_i, \cdots .v_k)$ if not (the hat means a missing element);*
3. *$\epsilon(v_0, \cdots, v_k) = sign(\pi)\epsilon(v_{\pi(0)}, \cdots, v_{\pi(k)})$ for every permutation π.*

For every k-face σ of a polytopal complex P, an orientation ϵ of σ is an orientation of the associated polytope. We say then that (σ, ϵ) is an oriented face of P. When $]tau$ is a facet of σ, we defines the induced orientation of an orientation ϵ of σ as

$$\epsilon \Big|_\tau (v_0, \cdots, v_{k-1}) := \epsilon(v_0, \cdots, v_{k-1}, v_k) \ .$$

Based on above definitions, we can then define the boundary operator for the polytopal complex as

$$\partial(\sigma^k, \epsilon) = \sum_{\tau \ facets \ of \ \sigma} \left(\tau, \epsilon \Big|_\tau\right) \ .$$

For detailed discussions, readers may consult [81].
We may also define the coboundary operator for simplicial complexes as,

Definition 3.1.4 *The coboundary operator is the duality operator,*

$$\delta^k : C^k[K] \to C^{k+1}[K]$$

to the boundary operator, ∂_k, with respect to the bilinear form between discrete forms and chains, i.e

$$< \delta^k \alpha^k, c_{k+1} > = < \alpha^k, \partial_{k+1} c_{k+1} > \quad \to \quad \delta^k(\alpha^k) = \alpha^k \circ \partial_{k+1}, \tag{3.5}$$

where $\alpha^k \in \Omega_d^k(K)$ is a discrete k-form, and $c_{k+1} \in C_{k+1}(K, \mathbb{Z})$ is a chain.

Therefore, the coboundary operator may be also given by specifying $\delta^k \sigma^k$ on each oriented k-cell σ^k, namely

$$\delta^k \sigma^k = \sum_{\sigma^{k+1} \succ \sigma^k} \pm \sigma^{k+1}, \tag{3.6}$$

where the sign is chosen as +(or -), if the orientation of σ^k coincides with or is opposite to that induced by σ^{k+1}.
To be able to apply the concept of k-cell to study lattice dynamics, we require the collection of all k-cells to be translation and symmetric invariant. In this work, we define an n-dimensional

lattice complex to be a polytopal complex such that:
(I) The underlying space is all of $\mathbb{R}^n, n = 2, 3$.
(II) The set of all lattice points defines an n-dimensional lattice.
(III) The cell set is translational symmetric.
The formulation of crystal lattice is processed as follows: First, we use the simplicial complex to describe or define the lattice that we are interested. Second we exam for its dual lattice complex as a polytopal complex or a CW complex, and last we scale the dual-lattice complex to create a disjoined cover or a super lattice (with different set of lattice points) to cover the entire crystal physical space.

3.2 Dual Lattice Complex

A very important concept of the discrete exterior calculus is the dual cell and dual complex. To define dual cell of a lattice complex, we first define the circumcenter of a k-cell σ^k, which is given by the center of the related k-sphere that has all $k+1$ vertices of σ^k on its surface, and it is denoted as $c(\sigma^p)$. A cell is said to be well-centered if $c(\sigma^k) \in \mathrm{I}nt(\sigma^k)$.

Definition 3.2.1 *Let K be a well-centered primal mesh of dimension n and let σ^k be the k-cell in K. The circumcentric dual cell of σ^k is defined as,*

$$D(\sigma^k) := \bigcup_{r=0}^{n-k} \bigcup_{\sigma^k \prec \sigma_1 \cdots \prec \sigma_r} Int\Big(c(\sigma^k)c(\sigma_1)\cdots c(\sigma_r)\Big) \ . \tag{3.7}$$

Note that the subscripts here are not the numbers of space dimension, but unspecified sequence numbers. The closure of the dual cell of σ^k is denoted $\bar{D}(\sigma^k)$ and called the closed dual cell. We will also use the notation $\star$ to indicate dual cells, i.e.

$$\star\sigma^k := \bar{D}(\sigma^k) \ .$$

Each (n-k)-simplex on the points $c(\sigma^p); c(\sigma_1)\cdots c(\sigma_r)$ is called an elementary dual simplex of σ^k. The collection of dual cells is called the dual cell decomposition of K and denoted $\star K$. In this work, we are particularly interested in a special form of Eq. (3.7) i.e.

$$D(\sigma^0) = \Big(\mathrm{I}nt\big(c(\sigma^0)\big)\Big) \cup \bigcup_{\sigma^0 \prec \sigma_1} \mathrm{I}nt\big(c(\sigma^0)c(\sigma_1)\big) \cup \cdots \cup \bigcup_{\sigma^0 \prec \sigma_1 \cdots \prec \sigma_n} \mathrm{I}nt\big(c(\sigma^0)c(\sigma_1)\cdots c(\sigma_n)\big) \ .$$

We would like to point out the fact that the collection of the dual cells at a given lattice point $\sigma^0(l)$ is a polytope, and it is in fact a CW complex, if the primal lattice domain (space) K is a CW complex. We denote it as $\star(\sigma^0(l), K)$. Dual lattice complexes are defined relative to their corresponding primal lattice complexes or mesh. While they represent the same subset of $\mathbb{R}^n$ as their associated primal mesh, they create different lattice structures for the same geometrical information. For examples, both BCC and FCC lattices are Bravais lattices, while both dual lattices are Bravais lattice structure.

Unlike the discrete lattice mechanics proposed in [26], in which lower dimensional lattice simplexes $\sigma^p, p = 0, 1, 2$ are employed to build defect models, in this work we are interested in a different defect model. First, all the defect models are built on lattice complexes (not necessarily simplexes), and second the proposed defect theory is based on a non-Bravais lattice complex formulation. To construct the non-Bravais lattice complex, we first examine the dual lattice complex $\star(\sigma^0, K)$ of the primal lattice mesh K.

In physical modelling, there are two types of dual cells: Voronoi dual cell and Barycentric dual cell. In this work, the term dual cell is exclusively referred to as the Voronoi dual cell. Without loss of generality, we may assume that the dual lattice complex is simplicial complex. Hence, we can treat the dual lattice complex the same as the original lattice complex, and employ the algebraic topology approach to analyze them. For simplicity and convenience, in the rest of the paper, without further explanation and complication, we also treat all the dual p-cells $\star\sigma^p$ as the regular lattice complex or CW complex. Since a regular crystal lattice simplexes are physical objects, they consist of either atom or ion sites (σ^0), atomistic bonds (σ^1), packing planes (σ^2), and bulk space inside a lattice net (σ^3), e.g. Thompson Tetrahedron. On the other hand, the dual-lattice complex is a topological or geometrical object. To distinguish two, we denote the p dimensional lattice complex as τ^p. For example, $\tau^3(l) \sim \star\sigma^0(l)$.

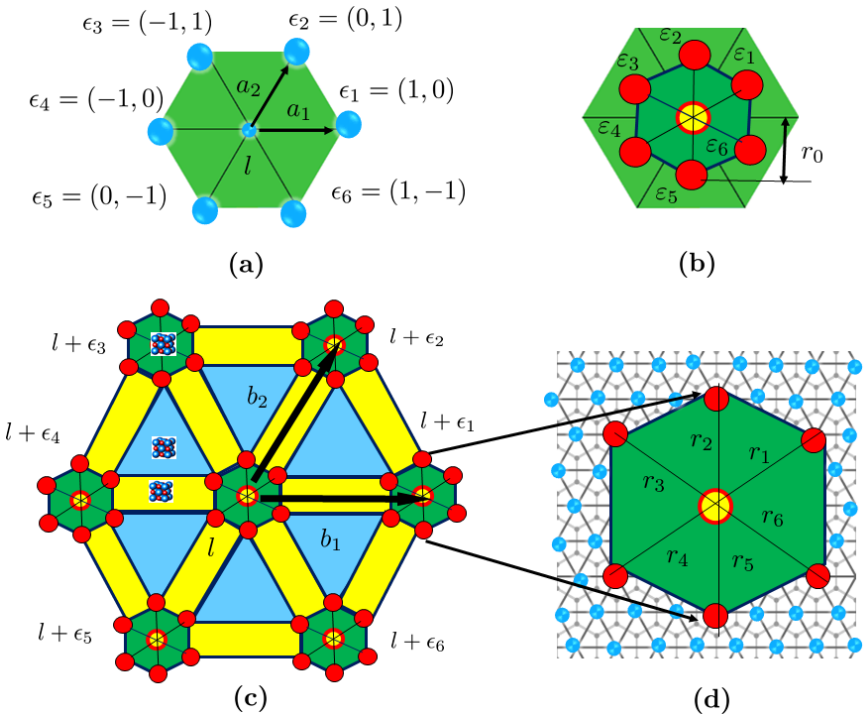

Figure 3.1: (a) Lattice complex of hexagonal (triangle) lattices, (b) its corresponding dual lattice complex, (c) the non-Bravais super lattice complex, and (d) the scaled lattice complex.

3.3 Discrete Crystal Defect Model–a Non-Bravais Super Lattice

In this work, we construct a non-Bravais super lattice, which is a lattice structure constructed based on $\bar{D}(\sigma^0(l))$ and the coarse graining procedure, where $l = (l^i), l \in \mathbb{R}^n,\ n = 2, 3$ is an integer position vector of the vertex $\sigma^0(l)$, if the primal lattice coordinate at l is expressed as

$$x(l) = l^i a_i, \quad i = 1, \cdots, n; \quad n = 2, 3$$

where a_i are lattice basis vectors, if we only consider the Bravais lattice.
For easy reference, in this dissertation, we follow the convention of lattice complex theory proposed in [26] without rehashing unless the content is new or it is worthy emphasizing. Without loss of generality, We may assume that a prime unit cell of a given crystal lattice as a CW lattice complex. If it has k-vertices, we may denote them as $\sigma^0(l+\epsilon_i),\ \ i = 1, 2, \cdots, k$ where i is the index of the coordination number of $\sigma^0(l)$, and ϵ_i is the integer coordinate of lattice point i relative to the lattice site l. It may be noted that the primal mesh of some crystals may involve part of the second nearest neighbors such as BCC crystals.
It should be noted that most crystals with non-Bravais dual lattices in three-dimensional space have Bravais lattices, For examples, the dual lattice of the FCC crystal is a BCC lattice (not crystal); while the dual lattice of the BCC crystal is a FCC lattice. However, for the discrete crystal defect model proposed in this work, all the super lattices are non-Bravais lattice.
To construct the non-Bravais super lattice, we select every vertex of the dual cell (closure) $\star\sigma^0(l) := \bar{D}(\sigma^0(l))$ together with $\sigma^0(l)$ as the basis at the lattice site l of the primal lattice mesh. To construct a super lattice, we need to scale both the primal lattice mesh as well as the non-Bravais basis, which is the dual-lattice cell. To scale the primal lattice mesh, we scale the primal lattice basis vectors as

$$(a_1, a_2, a_3) \ \rightarrow\ (b_1, b_2, b_3) = \beta_1(a_1, a_2, a_3), \quad \beta_1 > 0\ .$$

To scale the dual lattice cell, we scale the dual lattice constant r_0 i.e. the distance between the two close neighboring dual lattice points as

$$r = \beta_2 r_0\ , \quad \beta_2 > 0$$

where r_0 is the dual-lattice constant corresponding to the original lattice constant.
Since the dual cell is scaled, the distance between two lattice points in the dual cell may be much larger than that of the atomic bond distance in the primal lattice mesh. For a given coarse-grain defect model, one need to adjust the scale parameters, β_1 and β_2, to fix size of the super lattice constants (see Fig. 3.1). Moreover, a scaled dual cell may contain many atoms or ions, depending on the length scale of the coarse-graining model, i.e. β_1 and β_2. This is the reason why we do not call the proposed lattice defect model as the dual lattice, but as the *s*uper lattice denoted as $S \star (\sigma^0)$.

Note that when $\beta_1 >> \beta_2$ β_1 and β_2 may be chosen independently, this is because that β_1 is the scaling factor of the primal lattice mesh, whereas β_2 is the scaling factor of the dual lattice mesh. However, when β_1 and β_2 are comparable, certain constrain conditions may have to be imposed so that the distance between two dual lattice points (or sublattice points) must be less than the distance of two scaled (primal) lattice sites. By doing so, we create a non-Bravais lattice upon the primal lattice mesh with all the vertices of the dual lattice cell $\star e^0(l)$ as the basis for each lattice site. Assume that the dual lattice cell has k vertices. Now we have a super lattice in which an arbitrary lattice position vector may be expressed as

$$x(l,j) = l^i a_i + r_j, \quad l \in \mathbb{R}^n,\ n = 2,3 \ \ and \ \ j = 1,2,\cdots,k\ . \tag{3.8}$$

The coarse-grain parameters, β_1 and β_2, are the intrinsic embedding length scales of the multiscale formulation besides the original primal lattice constant, which is the length scale at fine scale or atomistic scale.

Remark 3.3.1 ***1****. In this work, we only consider the cases that the primal lattice is the Bravais lattice. By construction, comparing with the primal lattice, the corresponding super lattice is a non-Bravais lattice. We choose a scaled dual cell of the primal lattice complex as the basis or motif of the non-Bravais lattice.*
2*. The super lattice may be considered as a remesh of the primal lattice mesh. As* $\beta_1 \to 1$ *and* $\beta_2 \to 0$*, it recovers the primal lattice mesh.*
3*. As a remesh and coarsening of the primal lattice mesh, the super lattice points may not be the atom or ion sites.*

Now we demonstrate how to construct a super lattice by using dual lattice complex or polytopal cell complex for a give primal crystal lattice. To illustrate concepts, we first consider a two-dimensional example of triangle lattice. Fig. 3.1 shows a two-dimensional hexagonal (triangle) lattice. As shown in Fig. 3.1, the lattice basis $a_i, i = 1,2$, are given as,

$$a_1 = d_0\mathbf{e}_1 \quad and \ \ a_2 = d_0\Big(\cos\frac{\pi}{3}\mathbf{e}_1 + \sin\frac{\pi}{3}\mathbf{e}_2\Big),$$

where d_0 is the primal lattice constant. To scale the lattice basis pair, we let

$$b_1 = \beta_1 a_1 \ \ and \ \ b_2 = \beta_2 a_2, \quad \beta_1 > 0 \quad .$$

The integer coordinates of the nearest neighbors of lattice site l is given in Fig. 3.1.
In this case, the non-Bravais dual-lattice basis is in $\mathbb{R}^2$, and they are expressed as,

$$\varepsilon_i \ = \ r_0\Big(\cos\frac{(2i-1)\pi}{6}\mathbf{e}_1 + \sin\frac{(2i-1)\pi}{6}\mathbf{e}_2\Big),\ i = 1,2,\cdots,6$$

where r_0 is the dual lattice constant.
To scale the dual-cell, we let

$$r_i = \beta_2\varepsilon_i, \quad i = 1,2,\cdots,6\ .$$

As can be seen in Fig. 3.1(c), the super lattice mesh decomposes or partitions the lattice space into three different two-dimensional polytope cells $\tau_j^2, j = 1, 2, 3$. We label the blue triangle cell as the first 2D polytope ($j = 1$) element, the yellow rectangular cell as the second 2D polytope ($j = 2$) element, and the green hexagonal cell i.e. the dual cell as the third 2D polytope ($j = 3$) element. We interpret the triangle element as the bulk crystal element; the rectangular element as the interphase process zone element that may be associated with defects such as dislocation lines and cracks, and the green hexagonal element as the second order process zone element that might be associated to defects such as voids or cavities. At this stage, we have not inserted defects into a perfect crystal, but embedded possible defect modes, or defected DNAs if you will, into a perfect crystal lattice space or material. The atomistic potential in three different elements are exactly the same, and how defects will be developed in those process zone region will be discussed in Chapter 5.

Remark 3.3.2 ***1****. The three different polytopal complex cells $\tau_j^2, j = 1, 2, 3$ correspond to three lattice simplicial simplexes with different dimension $\sigma^j, j = 0, 1, 2$. When $\beta_1 \to 1$ and $\beta_2 \to 0$, $\tau_3^2 \to \sigma^0$ $\tau_2^2 \to \sigma^1$ and $\tau_1^2 \to \sigma^2$. This is the mathematical or physical foundation that we use τ_1^2 and τ_2^2 to model crystal defects. Using a more material science related term, we call them process zones or cohesive zones.*
2*. We would like to note that in [26] the exterior differential calculus approach is used to study the lattice complex as simplicial complex, whereas in this work we use the exterior differential calculus approach to study dual lattice complex, because the dual cell collection, $\star(\sigma^0(l), K)$, is a polytopal complex or CW complex in general.*

3.4 Discrete Crystal Defect Model for FCC and BCC crystals

To show that it is a universal truth that we can always mesh a given physical crystal space into a unique polytopal or polyhedral lattice complex mesh, and it is the intrinsic microstructure that is associated with every crystal lattices, in this section, we shall show how to create the super lattice mesh for both FCC and BCC crystals by using the discrete exterior calculus approach, and use them to create a multiscale process zone model to model various crystal defects.

The body-centered cubic (BCC) dual lattice

In this section, we shall create a non-Bravais super lattice mesh for a body-centered cubic(BCC) lattice. First, we are looking for the dual lattice complex for a given BCC lattice point $l = (l^1, l^2, l^3)$. The dual lattice cell complex for a given BCC lattice site is the so-called Wigner-Seitz cell (see Fig. 3.2 (b)), and the non-Bravais basis at each super lattice site is attached to a circumcentric dual cell of the BCC lattice. The primal lattice basis vectors

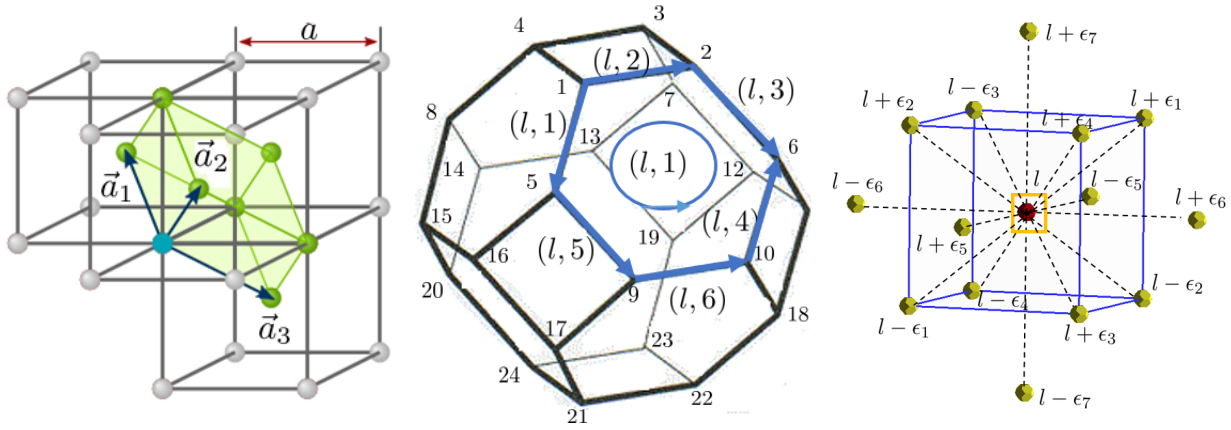

(a) (b) (c)

Figure 3.2: Lattice complex representation of BCC lattice and indexing scheme: (a) the primal BCC lattice basis, (b) the Wigner-Seitz cell of BCC crystal lattice–a truncated octahedron cell at the lattice site l, and (c)the formation of non-Bravais motif at sites of a super BCC lattice site.

(see Fig. 3.2(a)) are,

$$a_1 = (-\frac{a}{2}, \frac{a}{2}, \frac{a}{2}), a_2 = (\frac{a}{2}, -\frac{a}{2}, \frac{a}{2}), \text{ and } a_3 = (\frac{a}{2}, \frac{a}{2}, -\frac{a}{2}) \ .$$

First, we stretch the basis of BCC lattice uniformly,

$$b_i = \beta_1 a_i, \ i = 1, 2, 3 \ , \ \beta_1 > 1$$

to form lattice sites for the super lattice as shown in Fig. 3.2(c). Second, we choose the dual cell of BCC lattice as the non-Bravais motif or basis at each super lattice site. The Wigner-Seitz cell vertices of BCC lattice at the lattice site may be expressed as

$$\varepsilon_1 = a(1/2, 0, 1), \varepsilon_2 = a(0, 1/2, 1), \varepsilon_3 = a(-1/2, 0, 1), \varepsilon_4 = a(1, 0, 1/2), \varepsilon_5 = a(0, 1, 1/2),$$
$$\varepsilon_6 = a(-1, 0, 1/2), \varepsilon_7 = a(0, -1, 1/2), \cdots, \varepsilon_{23} = a(-1/2, 0, -1), \varepsilon_{24} = a(0, -1/2, -1) \ .$$

To scale the Wigner-Seitz cell, we can let $r_i = \beta_2 \varepsilon_i, \quad \beta_2 > 0$. Now we can express the non-Bravais super lattice sites as

$$x(l) = l^j b_j, \text{ and } x(l, \varepsilon_i) = l^j b_j + r_i, \quad i = 1, 2, \cdots, 24 \tag{3.9}$$

Since each super lattice site is attached with a truncated octahedron element, around the super lattice site l there are 14 adjacent truncated octahedron cells, which we also call as the 3^{rd} order process zone (for reason explained later). For the 15 truncated octahedron cells,

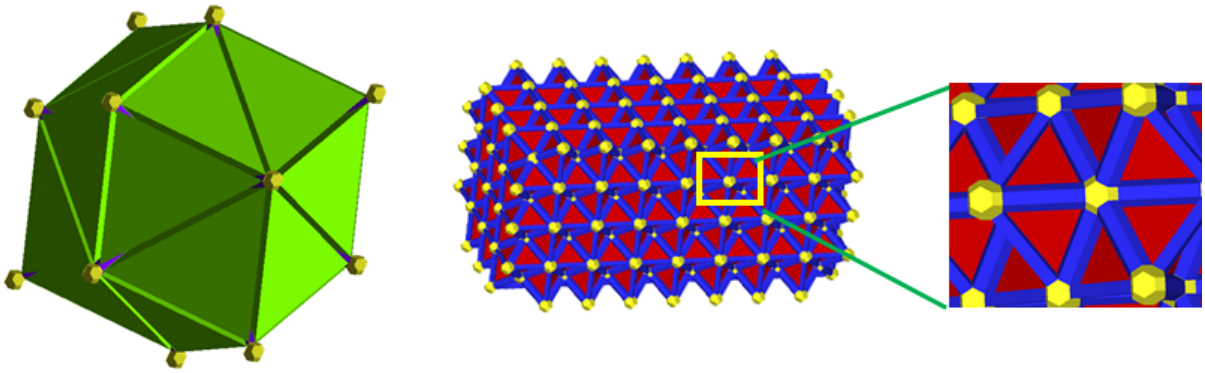

Figure 3.3: BCC super lattice mesh and polytopal elements.

we use the index system $l, l+\epsilon_1, l-\epsilon_1, l+\epsilon_2, ..., l-\epsilon_7$ label them as shown in Fig. 3.2(c) where

$$\begin{aligned} \epsilon_1 &= (1,0,0), \epsilon_2 = (0,1,0), \epsilon_3 = (0,0,1), \epsilon_4 = (1,1,1), \epsilon_5 = (0,1,1) \\ \epsilon_6 &= (1,0,1), \epsilon_7 = (1,1,0)\ . \end{aligned} \tag{3.10}$$

We denote the center of the middle octahedron as $c(\tau^3(l)) = \sigma^0(l)$. This is because that the dual cell of the BCC lattice is a well-centered circumentric cell.

As a non-Bravais lattice, each lattice site of BCC super lattice is attached to a stretched dual cell, which has 24 vertices. By connecting these 24 vertices with the vertices of the adjacent lattice site, it will form a partition mesh or decomposition of the entire super lattice space (see Fig. 3.3). This mesh only contains four types of non-overlapped 3D polytopal elements or complexes. We label them as $\tau_0^3(l(\ell)), \tau_1^3(l(\ell)), \tau_2^3(l(\ell))$, and $\tau_3^3(l(\ell))$, or $\tau_j^3(l(\ell)), j = 0, 1, 2, 3$, where the superscript i is the dimension of the polytope complex, and the subscript j is the type of polytopal element. Since for a given type of polytopal element j there can be more than one elements associated with a given super lattice site, we use the symbol $l(\ell)$ to distinguish them. In specific, we call $\tau_0^3(l(\ell))$ as bulk crystal elements, and there are 14 of them at each super lattice site, i.e. $\tau_0^3(l(\ell)), \ell = 1, 2, \cdots 24$; we call τ_1^3 as the wedge elements or 1st order process zones, and there are 36 of them at each lattice site, i.e. $\tau_1^3(l(\ell)), \ell = 1, 2, \cdots 36$; we call τ_2^3 as the prism elements or the 2nd order process zones, and there are 14 of them at each lattice site, i.e. $\tau_2^3(l(\ell)), \ell = 1, 2, \cdots 12$, and last we call τ_3^3 as the void element or the 3nd order process zones, there is only one at each lattice site, i.e. $\tau_3^3(l) := \tau_3^3(l(\ell)), \ell = 1$. It is in fact a scale-up dual cell or the Wigner-Seitz cell.

The closure of each 3D polytopal element is a union of many polytopal cells. In this paper, we introduce the following local cell index system to label them. We use the symbol, $\tau_j^i(l(\ell), m)$,

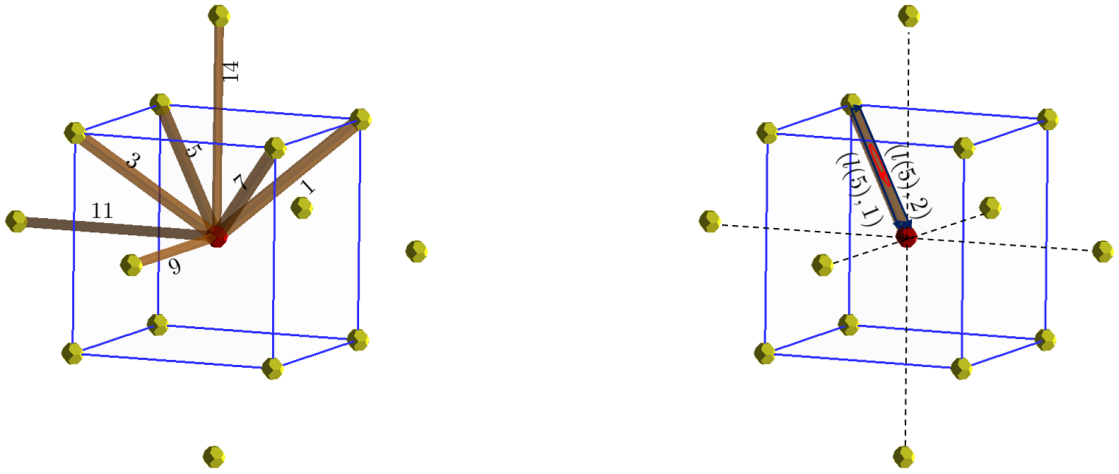

(a) (b)

Figure 3.4: Lattice complex representation of the BCC lattice and indexing scheme: (a) 2^{nd} order process zone elements and (b)prism element 5.

to label different polytope cells of different dimensions in the 3D polytopal element $\tau_j^3(l(\ell))$. Here the superscript i represents the dimension of the polytopal cell, subscript j denotes which type of 3D polytopal element that the cell is associated with, argument $l(\ell)$ denotes the number sequence of the 3D polytopal element at the lattice site l, and m is the number sequence of the polytopal complex indicated within the polytopal element $\tau_j^3(l(\ell))$. Simply speaking, for a given polytopal element $\tau_j^3(l(\ell))$, we use the symbol $\tau_j^3(l(\ell), m)$ to index its nodal points, edge lines, surface facets, and its volume. For example, we can define the local index for every vertices on as $\tau_3^3(l)$, i.e. $\tau_3^0(l, m), m = 1, 2, \cdots 24$, and then we can define the local index for every segment and facet cells on $\tau_3^3(l)$, i.e. $\tau_3^1(l, m), m = 1, 2, \cdots 36$, and $\tau_3^2(l, m), m = 1, \cdots, 14)$. Similarly, we can define the local index for every vertices on prism elements $\tau_2^3(l(\ell)), \ell = 1, 2, \cdots 14$, i.e. $\tau_3^0(l(\ell), m), m = 1, \cdots, 8)$, if the section of the prism element is square, or $\tau_3^0(l(\ell), m), m = 1, \cdots, 12$, if the section of the prism is hexagonal. Moreover, if the prism element has a square section, we can label the segment cell index as $\tau_1^2(l(\ell), m), m = 1, 2, \cdots, 12$, and the facet cell index as $\tau_2^2(l(\ell), m), m = 1, 2, \cdots, 6$; if the prism element has a hexagonal section, we can label the segment cell index as $\tau_1^2(l(\ell), m), m = 1, 2, \cdots, 16$, and the facet cell index as $\tau_2^2(l(\ell), m), m = 1, 2, \cdots, 8$. We can continue this process to define cell indices for wedge elements and bulk elements, until we have defined every local cell index for every 3D polytopal elements for a given lattice site l.

In passing, we note that this index system is redundant, and each cell complex will have multiple local indices with respect to different 3D polytopal elements. The array to map these local indices to the global indices is called the connectivity map, which is extensively used in the finite element method. Since we have not set up the global index for polytopal cells yet, for a convenient presentation, we use the following priority set of the local cell index

to represent the global cell index in the rest of the paper, which is based on the sequential order when the local cell index is defined. We define the local index for each polytopal cells on every 3D polytopal elements based on the sequence order of $\bar{\tau}_3^3(l(\ell)), \bar{\tau}_2^3(l(\ell)), \bar{\tau}_1^3(l(\ell))$, and $\bar{\tau}_0^3(l(\ell)$. For each polytopal cell, we choose the first defined local index to represent the global index.

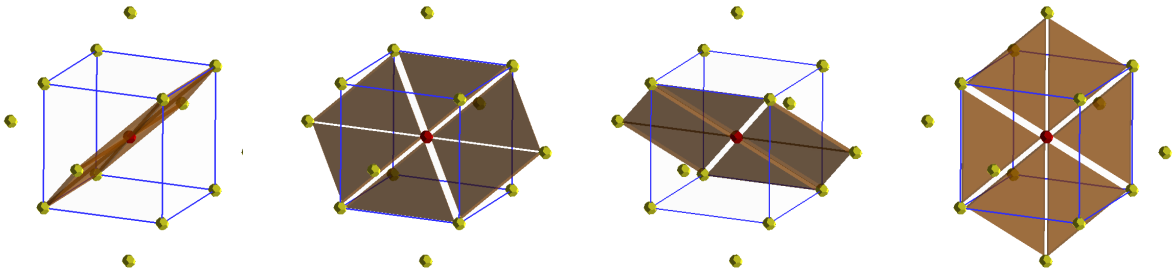

(a) (b) (c) (d)

Figure 3.5: Polytopal lattice complex representation of wedge elements.

Since each truncated octahedron cell has 24 vertices, 36 edges, and 14 faces. For the dual cell at the lattice site l, we label the 24 vertices as $\tau_3^0(l,m), j = 1, 2\cdots, 24$, the 36 edges as $\tau_3^1(l,m), m = 1, 2\cdots, 36$, and the 14 facets as $\tau_3^2(l,m), m = 1, 2, \cdots, 12$. These constitute the well-know Euler polyhedra formula,

$$\chi = V - E + F = 2 \quad \leftarrow \quad 24 - 36 + 14 = 2$$

in algebraic topology. Furthermore, one may note that the numbers of different types of process zone elements are also linked to the Euler characteristic.
Using boundary operator, we may represent the elementary segment and elementary area. For example, for the center dual cell, $\tau_3^3(l)$, we have,

$$\begin{aligned} \partial\tau_3^1(l,1) &= \tau_3^0(l,5) - \tau_3^0(l,1), && (3.11)\\ \partial\tau_3^2(l,1) &= \tau_3^1(l,1) + \tau_3^1(l,5) + \tau_3^1(l,6) + \tau_3^1(l,4), -\tau_3^1(l,2) - \tau_3^1(l,3) && (3.12) \end{aligned}$$

and in particular,

$$\begin{aligned} \partial\tau_3^3(l,1) = {} & \tau_3^2(l,1) + \tau_3^2(l,2) + \tau_3^2(l,3) + \tau_3^2(l,4) + \tau_3^2(l,5) \\ & + \tau_3^2(l,6) + \tau_3^2(l,7) - \tau_3^2(l,8) - \tau_3^2(l,9) - \tau_3^2(l,10) \\ & - \tau_3^2(l,11) - \tau_3^2(l,12) - \tau_3^2(l,13) - \tau_3^2(l,14)\ . \end{aligned} \tag{3.13}$$

Similar expressions may be derived for other types of 3D polytope cells. Considering the 14 polytope cells $\tau_2^3(l(i)), i = 1, 2, \cdots 14$ connecting to the lattice site l or the dual cell $\tau_3^3(l)$.

we call it as the prism element (see: Fig. 3.4). Its vertices, boundary edges, and boundary surfaces can be connected through boundary operators. For example, there are seven facets for the 5 prims element, i.e. $\partial\tau_2^1(l(5),j), j = 1,2,\cdots 7$. We express them analytically by using the boundary operator,

$$\partial\tau_2^1(l(5),1) = -\tau_3^0(l-\epsilon_3,9)+\tau_3^0(l,4), \tag{3.14}$$
$$\partial\tau_2^1(l(5),2) = -\tau_3^0(l-\epsilon_3,10)+\tau_3^0(l,3), \tag{3.15}$$

where the notation $\tau_3^0(l-\epsilon_i,j)$ denote that this is the j-th vertex ($j = 1,2,\cdots,24$) of on the $l\pm\epsilon_i, i = 1,2,\cdots 7$ polytopal cell, because we have 14 prism polytopal cells connecting to lattice site l or $\tau_3^3(l)$ as illustrated in Fig. 3.4.
Moreover, we have

$$\partial\tau_2^2(l(5),1) = \tau_2^1(l(5),1)-\tau_2^1(l(5),2)+\tau_3^1(l,7)-\tau_3^1(l-\epsilon_3,6), \tag{3.16}$$
$$\begin{aligned}\partial\tau_2^3(l,5) &= \tau_2^2(l(5),1)-\tau_2^2(l(5),2)+\tau_2^2(l(5),3)\\ &\quad +\tau_2^2(l(5),4)-\tau_2^2(l(5),5)-\tau_3^2(l,4)-\tau_3^2(l-\epsilon_3,10)\ .\end{aligned} \tag{3.17}$$

Furthermore, we may consider the polytope complex cell, $\tau_1^3(l,m), m = 1,2,\cdots 36$, which we refer to as the wedge elements (see Figs. 3.5 and 3.6) or the 1st order process zone. For small thickness of the wedge, it resemble fault plane or slip plane.

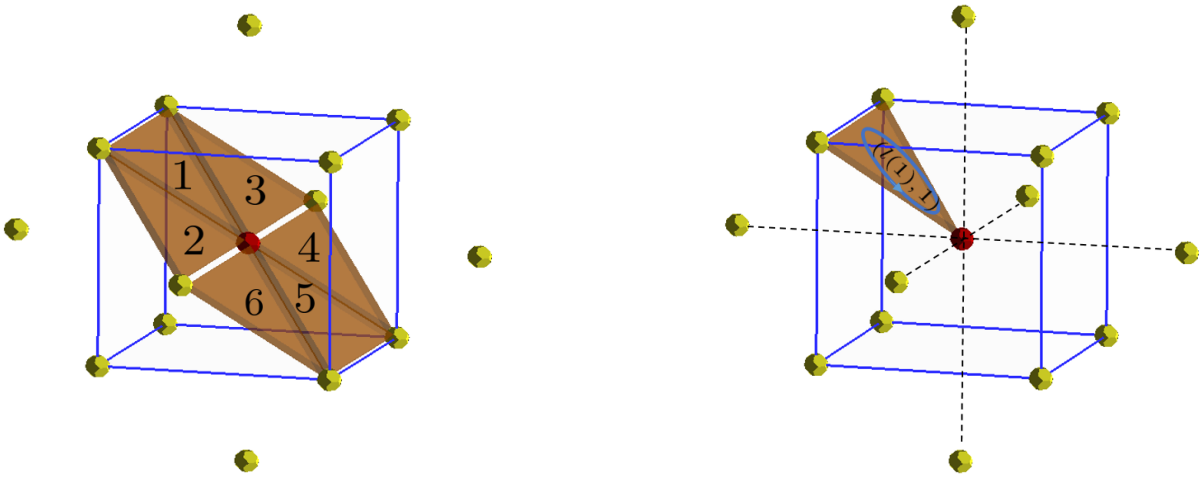

(a) (b)

Figure 3.6: Lattice complex representation of the BCC lattice and indexing scheme: (a)1^{st} order process zone elements and (b) wedge element 1.

The boundary of the wedge polytopal cells may be expressed by the boundary operator as follows,

$$\partial\tau_1^1(l(1),1) = \tau_3^0(l-\epsilon_3,9) - \tau_3^0(l+\epsilon_2,19), \quad (3.18)$$
$$\partial\tau_1^1(l(1),2) = -\tau_3^0(l-\epsilon_3,14) + \tau_3^0(l+\epsilon_2,23), \quad (3.19)$$
$$\partial\tau_1^2(l(1),1) = -\tau_2^1(l(5),1) + \tau_2^1(l(4),1) - \tau_1^1(l(1),1), \quad (3.20)$$
$$\partial\tau_1^2(l(1),2) = -\tau_2^1(l(5),2) + \tau_2^1(l(4),2) + \tau_1^1(l(1),2), \quad (3.21)$$
$$\partial\tau_1^2(l(1),3) = \tau_1^1(l(1),1) - \tau_3^1(l(5),10) - \tau_1^1(l(1),2) + \tau_3^1(l(4),12), \quad (3.22)$$
$$\partial\tau_1^3(l,1) = -\tau_2^2(l(5),1) - \tau_1^2(l(1),1) + \tau_2^2(l(4),1) + \tau_1^2(l(1),2) + \tau_1^2(l(1),3). \quad (3.23)$$

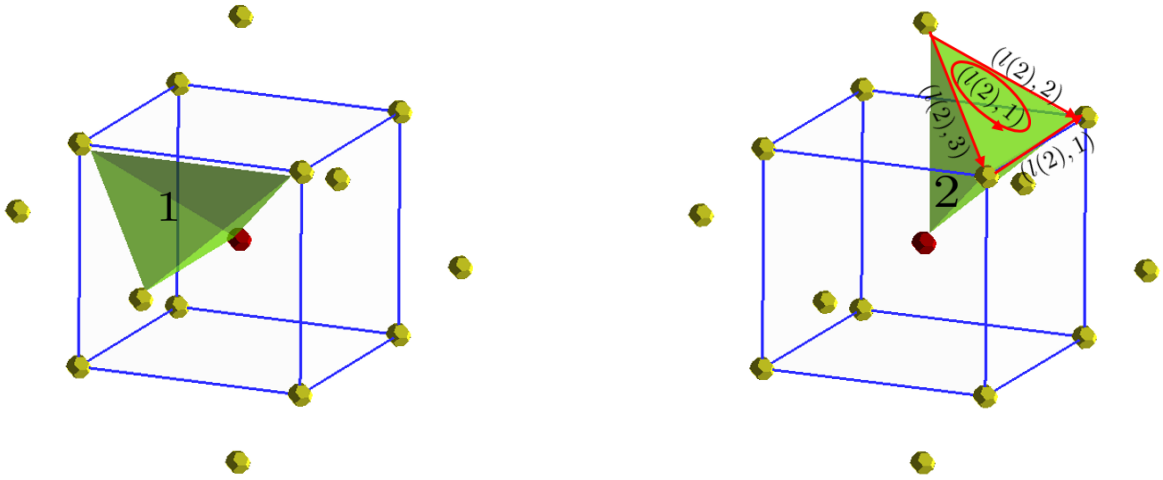

(a) (b)

Figure 3.7: Lattice complex representation of the BCC lattice and indexing scheme: 0^{th} order process zone elements.

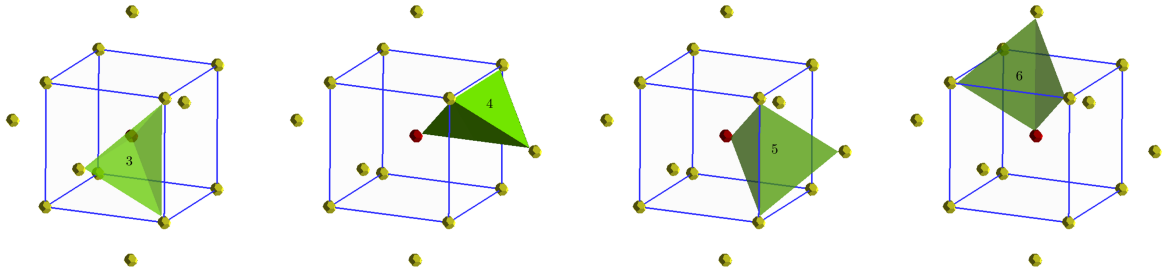

(a) (b) (c) (d)

Figure 3.8: Lattice complex representation of the BCC lattice and indexing scheme for the bulk element.

The last type of 3D polytope cells is the bulk element(Figs. 3.7 and 3.8), and BCC bulk polytopal cell is a tetrahedron, which is a simplicial simplex. For a given dual cell complex, it has 24 vertices, which corresponds to 24 bulk elements, i.e. $\tau_0^3(l,m), m = 1, 2, \cdots 24$.

$$\partial\tau_0^1(l(2),1) = \tau_3^0(l-\epsilon_1,14) - \tau_3^0(l+\epsilon_4,13) \tag{3.24}$$

$$\partial\tau_0^1(l(2),2) = \tau_3^0(l+\epsilon_1,14) - \tau_3^0(l+\epsilon_7,21) \tag{3.25}$$

$$\partial\tau_0^1(l(2),3) = \tau_3^0(l+\epsilon_4,13) - \tau_3^0(l+\epsilon_7,21) \tag{3.26}$$

$$\partial\tau_0^2(l(2),1) = \tau_0^1(l(2),1) - \tau_0^1(l(2),2) + \tau_0^1(l(2),3) \tag{3.27}$$

$$\partial\tau_0^3(l,2) = \tau_0^2(l(2),1) + \tau_0^2(l(2),2) - \tau_0^2(l(2),3) - \tau_0^2(l(2),4) \tag{3.28}$$

where the notation $\tau_1^2(l(i),j), i = 1, 2, \cdots, 36,\ j = 1, 2, 3, 4$ indicate that there are total 36 wedge elements $(\tau_1^3(l,i), i = 1, 2, \cdots, 36)$ connecting to at the lattice site l, and there are four facets: $j = 1, 2, 3, 4$ in each of these polytopal cells.

Remark 3.4.1 *The four different 3D polytope complex cells $\tau_j^3, j = 1, 2, 3, 4$ correspond to four lattice simplicial simplexes. When $\beta_1 \to 1$ and $\beta_2 \to 0$, $\tau_0^3 \to \sigma^3$, $\tau_1^3 \to \sigma^2$, and $\tau_2^3 \to \sigma^1$, and $\tau_3^3 \to \sigma^0$. This is the mathematical or physical foundation that we use τ_1^3, τ_2^3, and τ_3^3 as crystal defect models or material defect process zones or cohesive zones.*

The non-Bravais super lattice for face-centered cubic (FCC) lattice

In this section, we now construct the non-Bravais super lattice for FCC crystal lattices. The primal FCC Bravais lattice structure may be generated by the basis,

$$a_1 = (0, \frac{a}{2}, \frac{a}{2}), a_2 = (\frac{a}{2}, 0, \frac{a}{2}),\ \text{and}\ a_3 = (\frac{a}{2}, \frac{a}{2}, 0)$$

as shown in Fig. 3.9(a). To form the FCC super lattice, we stretch the FCC lattice basis as

$$b_i = \beta_1 a_i, \quad i = 1, 2, 3\ .$$

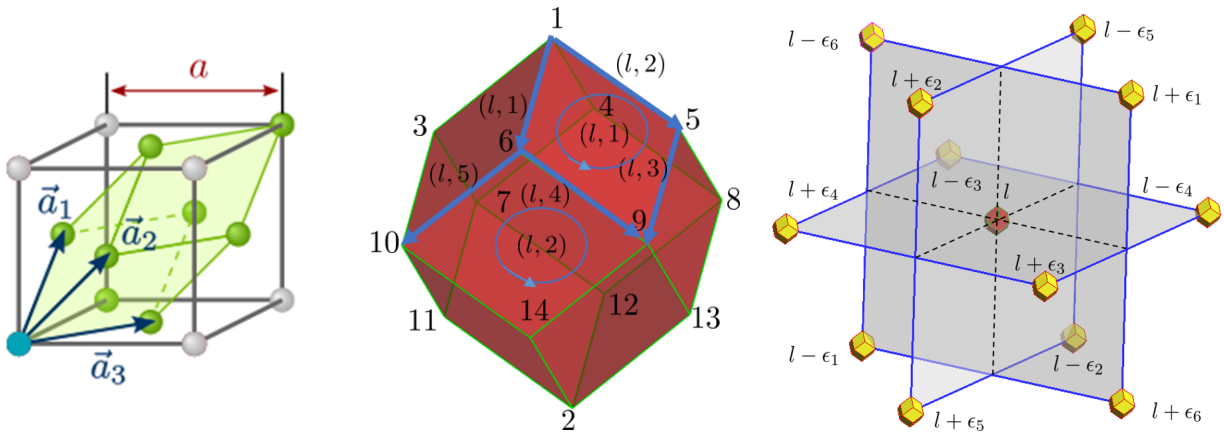

(a) (b) (c)

Figure 3.9: Lattice complex representation of the FCC lattice and indexing scheme: (a) FCC lattice basis vectors, (b) dual cell complex of $\sigma^0(l)$ (3^{rd} order process zone element), and (c) non-Bravais basis of FCC super lattice.

To construct the non-Bravais FCC super lattice, we select the all the vertices of the dual cell complex of $\sigma^0(l)$ i.e. $\tau(l) = \star(\sigma^0(l), K)$ and $\sigma^0(l)$ of the primal FCC lattice as the motif or the non-Bravais basis of the FCC super lattice. The dual cell complex of FCC is a rhombic dodecahedron as shown in Fig. 3.9(b), and it has 14 vertices. Among the fourteen vertices, the eight vertices where three faces meet at their obtuse angles have Cartesian coordinates,

$$\varepsilon_1 = (1,1,1), \varepsilon_2 = (1,1,-1), \varepsilon_3 = (1,-1,1), \varepsilon_4 = (1,-1,-1)$$
$$\varepsilon_5 = (-1,1,1), \varepsilon_6 = (-1,1,-1), \varepsilon_7 = (-1,-1,1), \text{ and } \varepsilon_8 = (-1,-1,-1) \ .$$

To stretch the dual lattice cell, we let

$$r_i = \beta_2 r_0 \varepsilon_i, \quad i = 1, 2, \cdots 14, \quad \beta_2 > 0$$

where $r_0 = a/\sqrt{3}$, so that the non-Bravais super lattice may be expressed as

$$x(l, \varepsilon_i) = l^j b_j + r_i, \quad i = 0, 1, 2, \cdots 14 \ . \tag{3.29}$$

In FCC lattice, there are twelve nearest neighbors for a given lattice site l, which can be located at the following relative position vectors: $l, l \pm \epsilon_1, , l \pm \epsilon_2, \cdots, l \pm \epsilon_6$ where

$$\pm\epsilon_1 = \pm(1,0,0), \pm\epsilon_2 = \pm(0,1,0), \pm\epsilon_3 = \pm(0,0,1)$$
$$\pm\epsilon_4 = \pm(-1,1,0), \pm\epsilon_5 = \pm(-1,0,1), \pm\epsilon_6 = \pm(0,-1,1) \ .$$

For FCC super lattice site l, there are 14 nearest neighbor sites, and we assign each neighboring super lattice site with a rhombic dodecahedron-shaped motif, which we also call as the 3^{rd} order process zone as shown in Fig. 3.9(c).

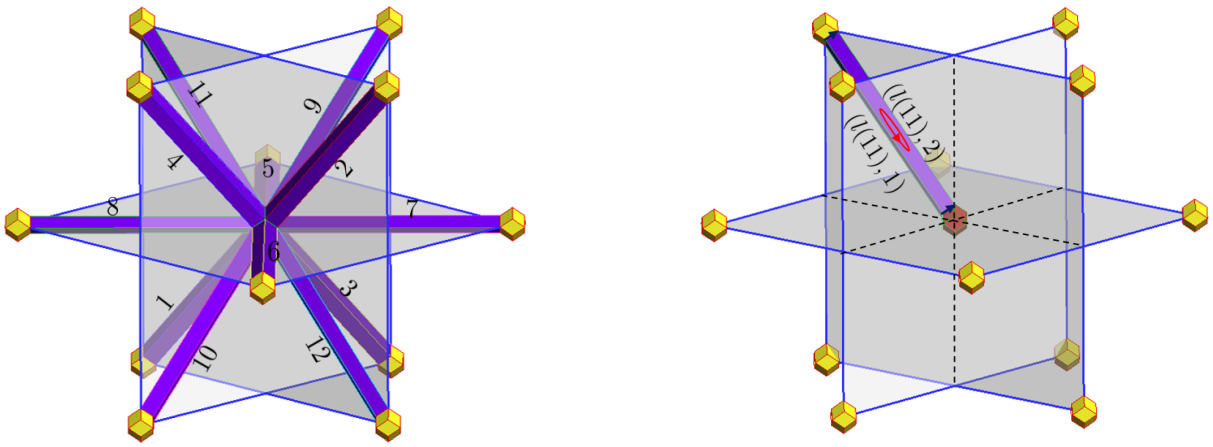

(a) (b)

Figure 3.10: Lattice complex representation of the FCC lattice and indexing scheme: (a)2^{nd} order process zone elements and (b)prism element 11.

Each rhombic dodecahedron element has 14 vertices, for the center dodecahedron l and their positions can be located as $x(l,j) = l^j b_j + r_j, j = 1,2,...,14$. Each rhombic dodecahedron element has 24 edges, i.e. $\tau_3^1(l,m), m = 1,2,\cdots 24$; it has 12 faces, i.e. $\tau_3^2(l,m), m = 1,2,\cdots 12$. Both elementary segment and elementary area can be represented by lower dimension polytopal cells by using boundary operator, e.g.

$$\partial\tau_3^1(l,1) = \tau_3^0(l,6) - \tau_3^0(l,1) \tag{3.30}$$

$$\partial\tau_3^2(l,1) = \tau_3^1(l,1) + \tau_3^1(l,4) - \tau_3^1(l,2) - \tau_3^1(l,3) \tag{3.31}$$

where for symbol τ_j^i in boundary construction, subscript i represents the dimension of object and superscript j denotes the j^{th} order process (cohesive) zone element.

$$\begin{aligned}\partial\tau_3^3(l,1) = {} & \tau_3^2(l,1) + \tau_3^2(l,2) + \tau_3^2(l,3) + \tau_3^2(l,4) + \tau_3^2(l,5) + \tau_3^2(l,6) \\ & - \tau_3^2(l,7) - \tau_3^2(l,8) - \tau_3^2(l,9) - \tau_3^2(l,10) - \tau_3^2(l,11) - \tau_3^2(l,12)\ .\end{aligned} \tag{3.32}$$

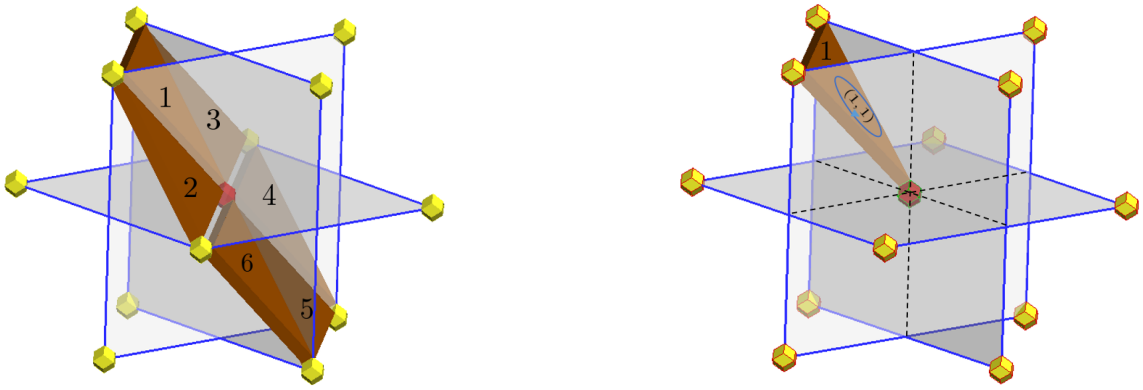

(a) (b)

Figure 3.11: Lattice complex representation of the FCC lattice and indexing scheme: (a)1^{st} order process zone elements and (b)wedge element 1.

By using the coboundary operator, we may further discover the connectivity structure of the polytopal mesh,

$$\delta\tau_3^0(l,6) = \tau_3^1(l,1) - \tau_3^1(l,4) - \tau_3^1(l,5) - \tau_2^1(1+\epsilon_1,2) - \tau_2^1(1+\epsilon_2,4) - \tau_2^1(1+\epsilon_3,1) \quad (3.33)$$

$$\delta\tau_3^1(l,4) = \tau_3^2(l,1) - \tau_3^2(l,2) - \tau_2^2(1+\epsilon_1,2) + \tau_2^2(1+\epsilon_3,4) \quad (3.34)$$

$$\delta\tau_3^2(l,1) = \tau_3^3(l) - \tau_2^3(l(2)) \ , \quad (3.35)$$

which are useful in finite element mesh generation and FEM connectivity array set-up. The polytopal cells on the prism element $\tau_2^3(l(11)$ (Fig. 3.10) may be constructed as following:

$$\partial\tau_2^1(l(11),1) = -\tau_3^0(l-\epsilon_6,14) + \tau_3^0(l,3), \quad (3.36)$$

$$\partial\tau_2^1(l(11),2) = -\tau_3^0(l-\epsilon_6,9) + \tau_3^0(l,1), \quad (3.37)$$

and

$$\partial\tau_2^2(l(11),1) = \tau_2^1(l(11),1) - \tau_2^1(l(11),2) + \tau_3^1(l,5) - \tau_3^1(l-\epsilon_6,10) \quad (3.38)$$

$$\partial\tau_2^3(l,11) = \tau_2^2(l(11),1) - \tau_2^2(l(11),2) + \tau_2^2(l(11),3) + \tau_2^2(l(11),4)) - \tau_3^2(l,4) - \tau_3^2(l-\epsilon_6,9) \ . \quad (3.39)$$

Similarly, we can construct the wedge element(Fig. 3.11) $\tau_1^3(l(1)$ by using the boundary operator,

$$\partial\tau_1^1(l(1),1) = \tau_3^0(l-\epsilon_6,9) - \tau_3^0(l+\epsilon_2,8), \quad (3.40)$$

$$\partial\tau_1^1(l(1),2) = -\tau_3^0(l-\epsilon_6,14) + \tau_3^0(l+\epsilon_2,12), \quad (3.41)$$

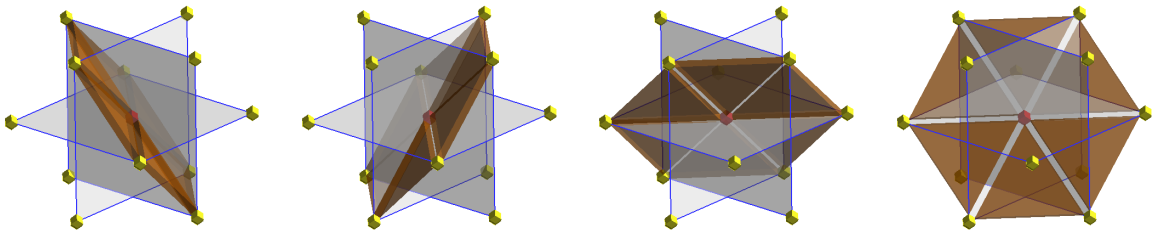

(a) (b) (c) (d)

Figure 3.12: Lattice complex representation of the FCC lattice and indexing scheme for the wedge element.

$$\partial\tau_1^2(l(1),1) = -\tau_2^1(l(11),1) + \tau_2^1(l(4),1) - \tau_1^1(l(1),1), \tag{3.42}$$
$$\partial\tau_1^2(l(1),2) = -\tau_2^1(l(11),2) + \tau_2^1(l(4),2) + \tau_1^1(l(1),2), \tag{3.43}$$
$$\partial\tau_1^2(l(1),3) = \tau_1^1(l(1),1) - \tau_3^1(l(11),10) - \tau_1^1(l(1),2) + \tau_3^1(l(4),12), \tag{3.44}$$

and

$$\partial\tau_1^3(l,1) = -\tau_2^2(l(11),1) - \tau_1^2(l(1),1) + \tau_2^2(l(4),1) + \tau_1^2(l(1),2) + \tau_1^2(l(1),3)\ . \tag{3.45}$$

Fig. 3.12 shows the indexing scheme for the wedge element.
For the bulk element number 2(Fig. 3.13), i.e. $\tau_0^3(l(2))$, we can construct its edges and surfaces by using the following boundary operators,

$$\partial\tau_0^1(l(2),1) = \tau_3^0(l-\epsilon_5,10) - \tau_3^0(l+\epsilon_1,7) \tag{3.46}$$
$$\partial\tau_0^1(l(2),2) = \tau_3^0(l+\epsilon_1,7) - \tau_3^0(l+\epsilon_2,8) \tag{3.47}$$

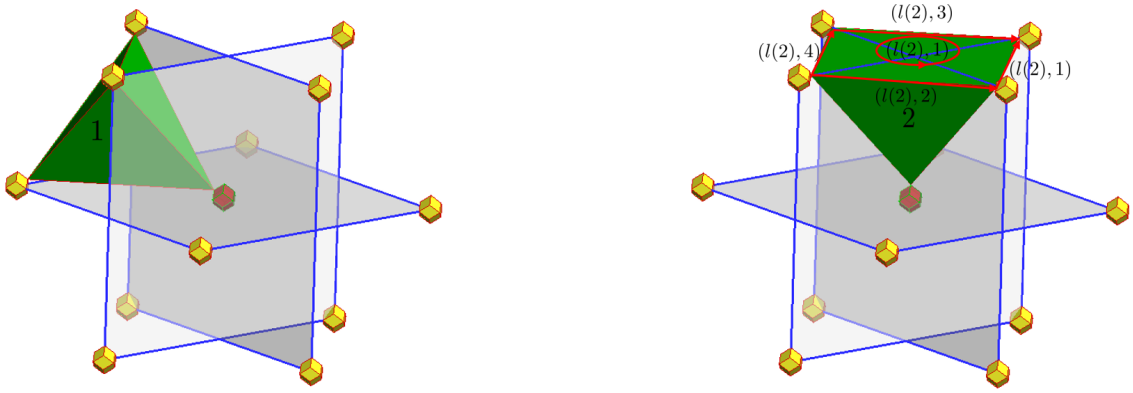

(a) (b)

Figure 3.13: Lattice complex representation of the FCC lattice and indexing scheme: 0^{th} order process zone elements.

$$\partial\tau_0^1(l(2),3) = \tau_3^0(l-\epsilon_6,9) - \tau_3^0(l-\epsilon_5,10) \tag{3.48}$$
$$\partial\tau_0^1(l(2),4) = \tau_3^0(l-\epsilon_6,9) - \tau_3^0(l+\epsilon_2,8) \tag{3.49}$$

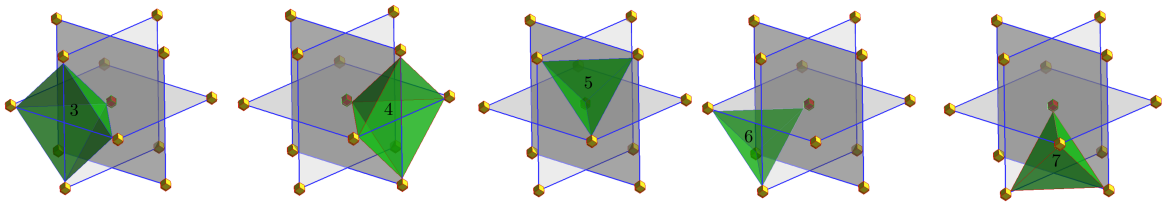

(a) (b) (c) (d) (e)

Figure 3.14: Lattice complex representation of the FCC lattice and indexing scheme for the bulk element.

and

$$\partial\tau_0^2(l(2),1) = \tau_0^1(l(2),2) + \tau_0^1(l(2),1) - \tau_0^1(l(2),3) - \tau_0^1(l(2),4) \tag{3.50}$$
$$\partial\tau_0^3(l,2) = \tau_0^2(l(2),2) - \tau_0^2(l(2),3) - \tau_0^2(l(2),4) + \tau_0^2(l(2),5) + \tau_0^2(l(2),1)\ . \tag{3.51}$$

Fig. 3.14 shows the indexing scheme for the bulk element.
Gluing all four types of polytopal elements together, we can have a non-Bravais FCC super lattice mesh as shown in Fig. 3.15. Again, for FCC super lattice, at each lattice site the

numbers of process zone elements, i.e. $\tau_0^3(l(v), v = 1, 2\cdots, 14$, $\tau_1^3(l(f), e = 1, 2, \cdots 24)$, and $\tau_2^3(l(f), f = 1, 2, \cdots, 12)$ satisfy the Euler characteristic formula,

$$\chi = V - E + F = 2 \quad \leftarrow \quad 14 - 24 + 12 = 2\ !$$

Fig. 3.15 illustrates the process of how to construct the mesh in terms of FCC lattice. For one representative atom, there are 12 nearest neighbors(Fig. 3.15(a)), each of which is shrinked to one rhombic dodecahedron. Such that there will be 13 rhombic dodecahedrons in total(Fig. 3.15(b)). Since a rhombic dodecahedron has 12 faces, so that we connect rhombic dodecahedron with 12 prism elements(Fig. 3.15(c)). Then a rhombic dodecahedron has 24 edges, and can connect to 24 wedge elements, which forms 4 (111) slip plane(Fig. 3.15(e)). Finally the gaps are filled with tetrahedron elements (Fig. 3.15(f)).

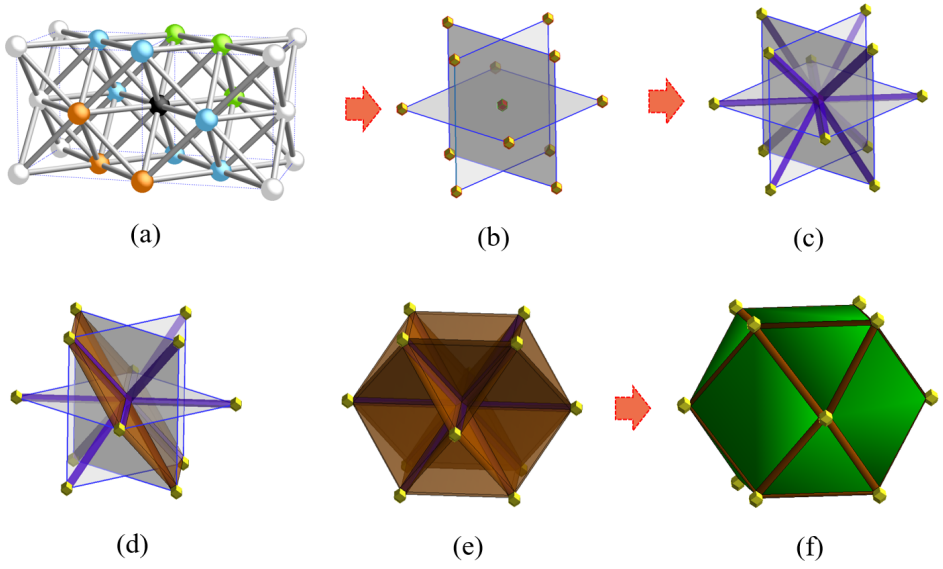

Figure 3.15: Construction process of FCC mesh.

Chapter 4

Dislocation Patterns of BCC and FCC Crystals

The main assumption in MCDD model is that material defects are related to its intrinsic microstructure derived from the microstructure of the original perfect crystal. This chapter simulate the dislocation patterns with molecular dynamics and compare the mesh embedded in MCDD with experimental observation.

4.1 Comparison of Dislocation Patterns in Relaxation System

To prove this assumption, dislocation patterns are simulated by direct atomistic simulation for both FCC and BCC crystals. Dislocation patterns are plotted by Atomeye[82]. For the dislocation patterns of Mo(Fig. 4.1(b)), a dipole of junction is generated by juxtaposition of four dislocation dipoles introduced along[112] and $[11\bar{2}]$ with Burgers vectors $\frac{1}{2}[111]$ and $\frac{1}{2}[11\bar{1}]$ respectively. The supercell is defined by its repeat vectors, $16[11\bar{2}] \times 19[1\bar{1}0] \times 16[112]$. The dislocation pattern is produced after relaxation[62, 63]. Similarly, the dislocation patterns of Cu (Fig. 4.1(a))is generated by juxtaposition of four dislocation dipoles introduced along$[10\bar{1}]$ and $[1\bar{2}1]$ with Burgers vectors $\frac{1}{2}[1\bar{1}0]$ and $\frac{1}{2}[01\bar{1}]$ respectively. The supercell is defined by its repeat vectors, $18[1\bar{2}1] \times 14[1\bar{1}1] \times 28[10\bar{1}]$. The dislocation patterns are produced after relaxation and are regarded as statble structures. Fig. 4.1(c) and 4.1(d) demonstrate the corresponding mesh in MCDD model, which prove that the dislocation patterns are actually embedded in the discrete mesh of MCDD model.

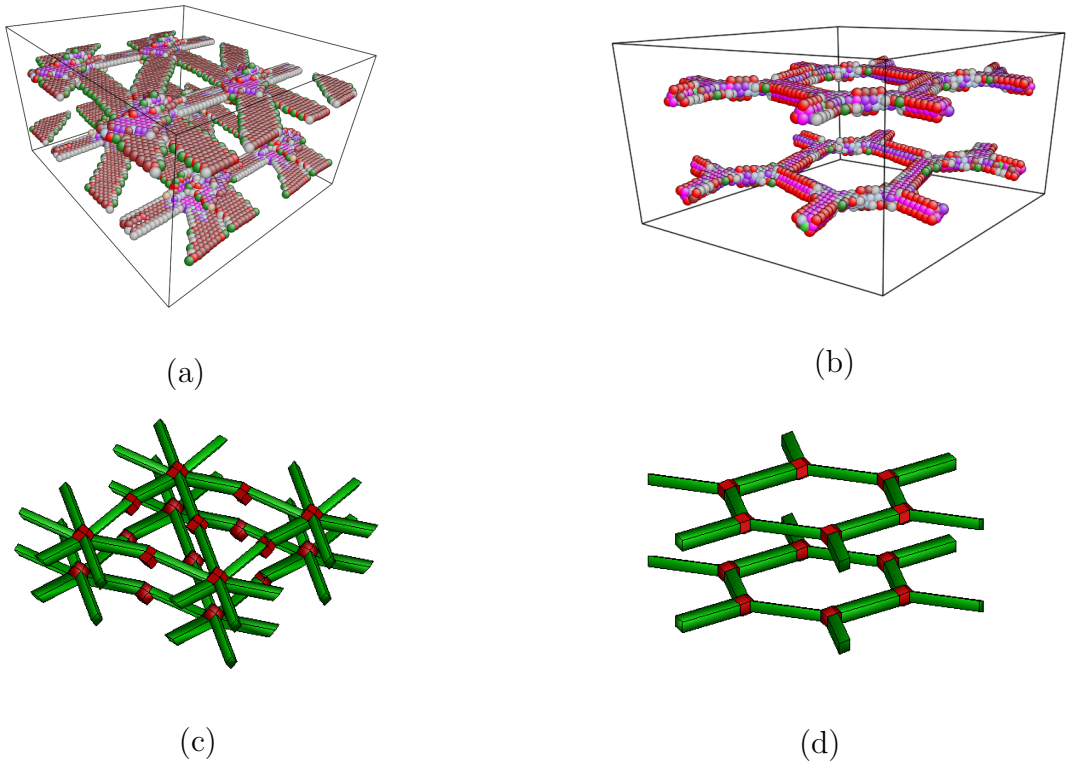

(a) (b)

(c) (d)

Figure 4.1: Dislocation patterns of (a) FCC Cu and (b) BCC Mo, the colorbar is based on coordinate number and perfectly coordinated atoms are removed. (c) and (d)the corresponding mesh of MCDD.

4.2 Comparison of Dislocation Patterns with Experiments

As shown in chapter 2, the formation of dislocation patterns significantly relies on the active slip systems[55]. Fig. 4.3 shows the formation mechanism of three types of dislocation patterns that are present in MCDD mesh, which are corresponding to the dislocation structures of different orientations as shown in Fig. 4.2. In addition, Fig. 4.3(a) shows the cell structure in experimental observation and the similar patterns in MCDD mesh in $[\bar{1}11]$ plane. Similarly, labyrinth structures can be observed in [001] plane both in experiments and MCDD mesh. While wall structures tend to seen in [011] plane(Fig. 4.3). This comparison demonstrates that MCDD model embeds all possible dislocation patterns into its mesh and these patterns will automatically emerge in the condition of plastic deformation.

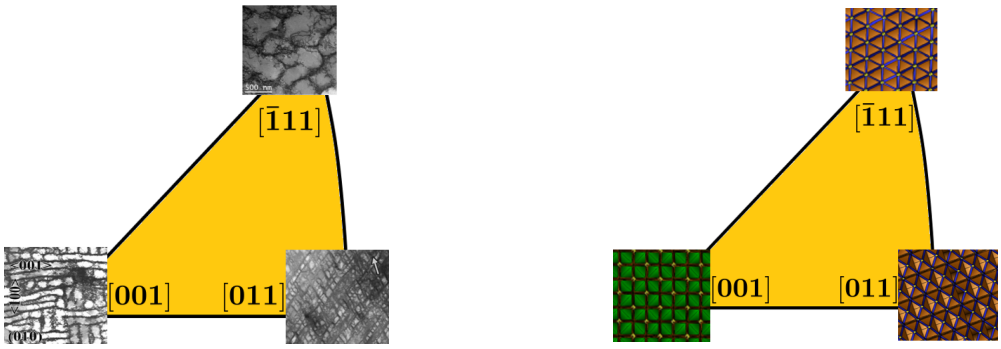

(a) (b)

Figure 4.2: Comparison of formation mechanisms of different dislocation patterns in different orientations[56, 49].

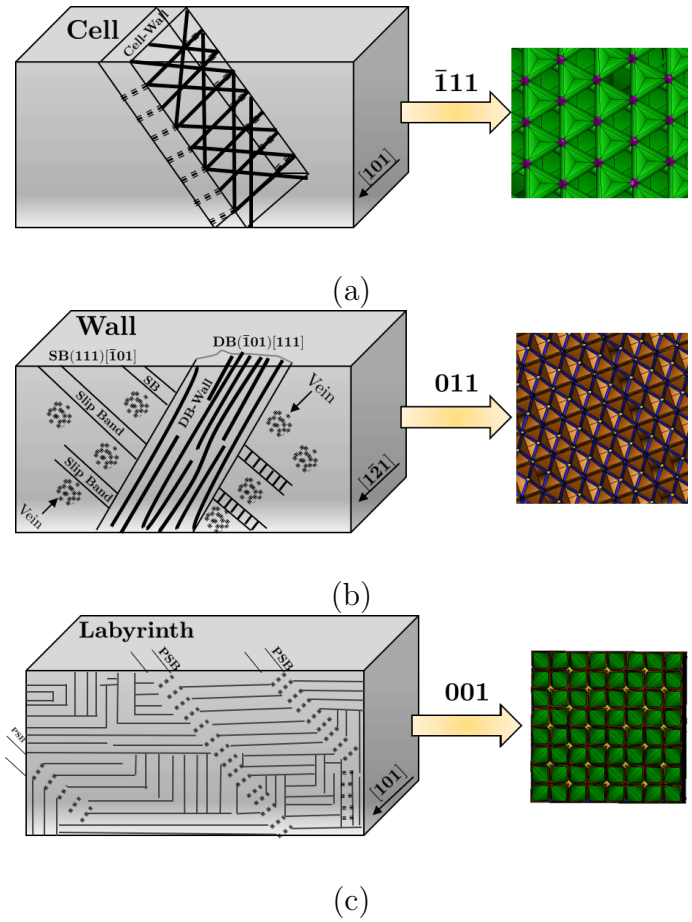

Figure 4.3: Comparison of formation mechanisms of different wall structures in different orientations[55].

Chapter 5

Multiscale Constitutive Modelling

In this chapter, we discuss how to derive the constitutive equation inside the bulk and process zone by using the higher-order Cauchy-Born rule. Before deriving stress-strain relation, we first explain what is Cauchy-Born rule.

5.1 Higher-order Cauchy-Born Rules

In the following, we first lay out the hierarchical higher order Cauchy-Born rules up to the fourth order.

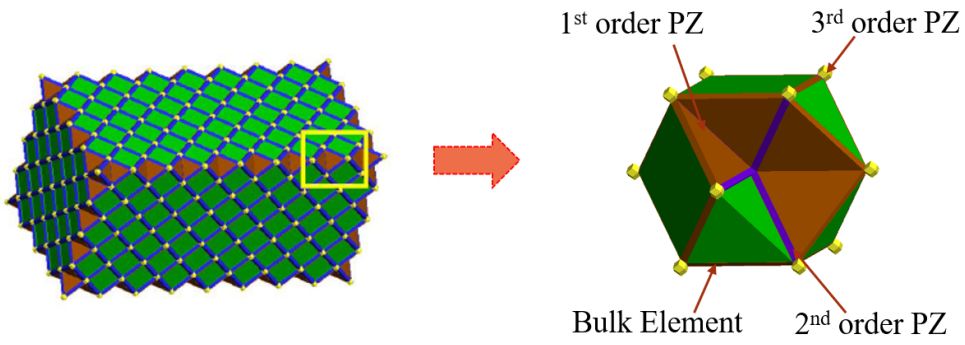

Figure 5.1: FCC super lattice mesh.

5.1.1 The 1st order Cauchy-Born rule in the 0th order process zone (bulk element)

In a crystalline bulk element, say element e, which usually is a part of single crystal or a single grain, we assume that the deformation is uniform, and thus the deformation gradient inside the whole element is the same, i.e.

$$\mathbf{F}_e(\mathbf{X}) = \frac{\partial \mathbf{x}}{\partial \mathbf{X}}\Big|_{\mathbf{x}} = const., \quad \forall \mathbf{X} \in \Omega_e$$

Note that in the entire solid domain we have $\mathbf{F}_e, e = 1, 2, \cdots n^b_{elem}$, where n^b_{elem} is the total number of bulk (superscript) elements (Fig. 5.1).
Then based on the first order Cauchy-Born rule, an arbitrary deformed chemical bond $\mathbf{r}_i$ between two atoms inside the element can be related to the original undeformed bond $\mathbf{R}_i$ as

$$\mathbf{r}_i = \mathbf{F}_e \cdot \mathbf{R}_i, \ i = 1, \cdots n_b \tag{5.1}$$

where index i denotes a chemical bond inside element e and n_b represents the total number of bonds the element. In practice, chemical bonds in a representative unit inside Ω_e.
With these definitions, the strain energy density in the bulk element e can be written as

$$W_{0e} = \frac{1}{2\Omega_0}\sum_{i=1}^{n_b}\phi(r_i) = \frac{1}{2\Omega_0}\sum_{i=1}^{n_b}\phi(\mathbf{F}_e \cdot \mathbf{R}_i) = W(\mathbf{F}_e), \tag{5.2}$$

where n_b again indicates the number of neighbouring bonds in a representative unit cell; Ω_0 is the volume of the unit cell in the referential configuration; $\phi(r_i)$ is the atomistic potential, and $r_i = |\mathbf{r}_i|$ is the current length of bond $\mathbf{r}_i$ in the unit cell. The energy density expression (5.2) is formulated based on the first order Cauchy-Born rule (see Eq. (5.1)), and the first Piola-Kirchhoff stress tensor inside the bulk crystal element can be found by

$$\mathbf{P} = \frac{\partial W_{0e}}{\partial \mathbf{F}}\Big|_{\mathbf{F}_e} .$$

5.1.2 The 2nd order Cauchy-Born rule in the 1st order process zone

For the first-order process zone element, which is usually a wedge element between two adjacent bulk crystal elements (Fig. 5.1), the second order Cauchy-Born rule is employed to establish the constitutive relation in it. The so-called second order Cauchy-Born rule assumes that in a representative 1st order process zone element e, a deformed chemical bond between two atoms may be expressed by the following expression,

$$\mathbf{r}_i = \mathbf{F}_e \cdot \mathbf{R}_i + \frac{1}{2}\mathbf{G}_e : (\mathbf{R}_i \otimes \mathbf{R}_i), \tag{5.3}$$

where

$$\mathbf{G}_e = \frac{\partial^2 \mathbf{x}}{\partial \mathbf{X} \otimes \partial \mathbf{X}} = \frac{\partial \mathbf{F}_e}{\partial \mathbf{X}} = const. \ \ \forall \mathbf{X} \in \Omega_e$$

Note that in this case, $\mathbf{F}_e \neq const.$

Taking into account the 1st order strain gradient effect on strain energy density, we may write the strain energy density in the 1st order process zone element e as

$$W_{1e} = \frac{1}{2\Omega_0} \sum_{i=1}^{n_b} \phi(r_i) = \frac{1}{2\Omega_0} \sum_{i=1}^{n_b} \phi \left(\left| \mathbf{F}_e \cdot \mathbf{R}_i + \frac{1}{2} \mathbf{G}_e : (\mathbf{R}_i \otimes \mathbf{R}_i) \right| \right) = W(\mathbf{F}_e, \mathbf{G}_e) \ , \qquad (5.4)$$

which is based on the second order Cauchy-Born rule (see Eq. (5.3). Subsequently, the constitutive relation inside the 1st order process zone can be expressed as,

$$\mathbf{P} = \frac{\partial W_{1e}}{\partial \mathbf{F}} \Big|_{\mathbf{F}_e, \mathbf{G}_e} \quad and \ \ \mathbf{Q} = \frac{\partial W_{1e}}{\partial \mathbf{G}} \Big|_{\mathbf{F}_e, \mathbf{G}_e} \ .$$

5.1.3 The 3rd order Cauchy-Born rule in the 2nd order process zone

For the second-order process zone element, which is a prism element (Fig. 5.1), the third-order Cauchy-Born rule is employed to derive its constitutive relation. In the third-order Cauchy-Born rule, a chemical bond can be expressed as

$$\mathbf{r}_i = \mathbf{F}_e \cdot \mathbf{R}_i + \frac{1}{2!} \mathbf{G}_e : (\mathbf{R}_i \otimes \mathbf{R}_i) + \frac{1}{3!} \mathbf{H}_e \vdots (\mathbf{R}_i \otimes \mathbf{R}_i \otimes \mathbf{R}_i), \qquad (5.5)$$

where $i = 1, \cdots n_b$ is the index of number of bonds in a unit cell, and

$$\mathbf{H}_e = \frac{\partial^3 \mathbf{x}}{\partial \mathbf{X} \otimes \partial \mathbf{X} \otimes \partial \mathbf{X}} = \frac{\partial^2 \mathbf{F}}{\partial \mathbf{X} \otimes \partial \mathbf{X}} = \frac{\partial \mathbf{G}}{\partial \mathbf{X}} = const. \ \ \forall \mathbf{X} \in \Omega_e \ .$$

Following the similar argument mentioned above, we can show that the strain energy density in the second-order process zone element e may be generally expressed in the form

$$W_{2e} = W(\mathbf{F}_e, \mathbf{G}_e, \mathbf{H}_e) \ .$$

Note that in this case $\mathbf{F}_e \neq const.$ and $\mathbf{G}_e \neq const.$.

By taking into account the first and second order strain gradients, we can derive the constitutive relations in the 2nd order process zone as

$$\mathbf{P} = \frac{\partial W_{2e}}{\partial \mathbf{F}} \Big|_{\mathbf{F}_e, \mathbf{G}_e, \mathbf{H}_e}, \quad \mathbf{Q} = \frac{\partial W_{2e}}{\partial \mathbf{G}} \Big|_{\mathbf{F}_e, \mathbf{G}_e, \mathbf{H}_e} \quad and \ \ \mathbf{U} = \frac{\partial W_{2e}}{\partial \mathbf{H}} \Big|_{\mathbf{F}_e, \mathbf{G}_e, \mathbf{H}_e} \ .$$

5.1.4 The 4th order Cauchy-Born rule in the 3rd order process zone

For the third-order process zone element, which is a rhombic dodecahedron (Fig. 5.1), the fourth-order Cauchy-Born rule is employed to derive its constitutive relation. By using the fourth-order Cauchy-Born rule, a chemical bond can be expressed as

$$\mathbf{r}_i = \mathbf{F}_e \cdot \mathbf{R}_i + \frac{1}{2!}\mathbf{G}_e : (\mathbf{R}_i \otimes \mathbf{R}_i) + \frac{1}{3!}\mathbf{H}_e \dddot{:} (\mathbf{R}_i \otimes \mathbf{R}_i \otimes \mathbf{R}_i) + \frac{1}{4!}\mathbf{K}_e :: (\mathbf{R}_i \otimes \mathbf{R}_i \otimes \mathbf{R}_i \otimes \mathbf{R}_i), \quad (5.6)$$

where $i = 1, \cdots n_b$ is the index of number of bonds in a unit cell, and

$$\mathbf{K}_e = \frac{\partial^4 \mathbf{x}}{\partial \mathbf{X} \otimes \partial \mathbf{X} \otimes \partial \mathbf{X} \otimes \partial \mathbf{X}} = \frac{\partial^3 \mathbf{F}}{\partial \mathbf{X} \otimes \partial \mathbf{X} \otimes \partial \mathbf{X}} = \frac{\partial^2 \mathbf{G}}{\partial \mathbf{X} \otimes \partial \mathbf{X}} = \frac{\partial \mathbf{H}}{\partial \mathbf{X}} = const. \ \ \forall \mathbf{X} \in \Omega_e \ .$$

Note that the dot product operation defined in this paper has the following equivalent indicial notation,

$$\mathbf{F} \cdot \mathbf{R}_i = F_{mn} R_n \mathbf{e}_m, \quad \mathbf{G} : (\mathbf{R}_i \otimes \mathbf{R}_i) = G_{\ell mn} R_m R_n \mathbf{e}_\ell, \quad and$$
$$\mathbf{H} \dddot{:} (\mathbf{R}_i \otimes \mathbf{R}_i \otimes \mathbf{R}_i) = H_{\ell mno} R_m R_n R_o \mathbf{e}_\ell, \quad and$$
$$\mathbf{K} :: (\mathbf{R}_i \otimes \mathbf{R}_i \otimes \mathbf{R}_i \otimes \mathbf{R}_i) = K_{\ell mnop} R_m R_n R_o R_p \mathbf{e}_\ell, \quad \ell, m, n, o, p = 1, 2, 3$$

where $\mathbf{e}_\ell, \ell = 1, 2, 3$ are the unit base vectors of the Cartesian coordinates.
Following the similar argument mentioned above, we can show that the strain energy density in the third-order process zone element e may be generally expressed in the form

$$W_{3e} = W(\mathbf{F}_e, \mathbf{G}_e, \mathbf{H}_e, \mathbf{K}_e) \ .$$

Note that in this case $\mathbf{F}_e \neq const.$ and $\mathbf{G}_e \neq const.$ and $\mathbf{H}_e \neq const.$ By taking into account the first and second order strain gradients, we can derive the constitutive relations in the 3rd order process zone as

$$\mathbf{P} = \frac{\partial W_{3e}}{\partial \mathbf{F}} \Big|_{\mathbf{F}_e, \mathbf{G}_e, \mathbf{H}_e, \mathbf{K}_e}, \quad \mathbf{Q} = \frac{\partial W_{3e}}{\partial \mathbf{G}} \Big|_{\mathbf{F}_e, \mathbf{G}_e, \mathbf{H}_e, \mathbf{K}_e},$$

$$\mathbf{U} = \frac{\partial W_{3e}}{\partial \mathbf{H}} \Big|_{\mathbf{F}_e, \mathbf{G}_e, \mathbf{H}_e, \mathbf{K}_e}, \quad \mathbf{V} = \frac{\partial W_{3e}}{\partial \mathbf{K}} \Big|_{\mathbf{F}_e, \mathbf{G}_e, \mathbf{H}_e, \mathbf{K}_e} \quad .$$

5.2 Multiscale Constitutive Models

For metallic materials, we can use the atomistic potential based on the embedded atom method (EAM) to construct the free energy density function for the crystal solid under consideration,

$$W = \frac{1}{\Omega_0} \sum_{i=1}^{n_b} \left(F(\bar{\rho}_i) + \frac{1}{2} \sum_{j \neq i} \phi(r_{ij}) \right), \quad r_{ij} = \mid \mathbf{r}_j - \mathbf{r}_i \mid . \quad (5.7)$$

where $i, j = 1, 2, \cdots, n_b$ is the bond number of pair potential in a unit cell. $\phi(r_{ij})$ is the pairwise interaction function. Since $\phi(r_{ij})$ is always shared by two atoms, there is a coefficient of $\frac{1}{2}$ for the pairwise interaction function. $F(\bar{\rho}_i)$ is the embedded energy function and the host electron density $\bar{\rho}$ is a function of the electron density

$$\bar{\rho} = \sum_{j \neq i} \rho(r_{ij}).$$

Since in this dissertation we only consider the Bravais type of primal crystal lattices, the potential energy density inside a unit cell can be further simplified as

$$W = \frac{1}{\Omega_0} \left(F(\bar{\rho}) + \frac{1}{2} \sum_j \phi(r_j) \right), \quad \bar{\rho} = \sum_j \rho(r_j) \ , \tag{5.8}$$

where $i, j = 1, 2, ..., n_b$ is the bond number of pair potential in a unit cell. With the above free energy density, the first Piola-Kichhoff stress can be obtained as

$$\mathbf{P} = \frac{\partial W}{\partial \mathbf{F}} = \frac{1}{\Omega_0} \sum_{j=1}^{n_b} \left(F'(\bar{\rho}) \rho'(r_j) + \frac{1}{2} \phi'(r_j) \right) \frac{\mathbf{r}_j \otimes \mathbf{R}_j}{r_j} \ . \tag{5.9}$$

Other useful formulas for stresses, such as the second Piola-Kirchhoff stress (Eq. 5.10) and Cauchy Stress (Eq. 5.11), as well as high order stress couples can also be derived as,

$$\mathbf{S} = \frac{1}{\Omega_0} \sum_{j=1}^{n_b} \left(F'(\bar{\rho}) \rho'(r_j) + \frac{1}{2} \phi'(r_j) \right) \frac{\mathbf{R}_j \otimes \mathbf{R}_j}{r_j}, \tag{5.10}$$

$$\boldsymbol{\sigma} = \frac{1}{\Omega} \sum_{j=1}^{n_b} \left(F'(\bar{\rho}) \rho'(r_j) + \frac{1}{2} \phi'(r_j) \right) \frac{\mathbf{r}_j \otimes \mathbf{r}_j}{r_j}, \tag{5.11}$$

$$\mathbf{Q} = \frac{\partial W}{\partial \mathbf{G}} = \frac{1}{2\Omega_0} \sum_{j=1}^{n_b} \left(F'(\bar{\rho}) \rho'(r_j) + \frac{1}{2} \phi'(r_j) \right) \frac{\mathbf{R}_j \otimes \mathbf{R}_j \otimes \mathbf{R}_j}{r_j}, \tag{5.12}$$

$$\mathbf{U} = \frac{\partial W}{\partial \mathbf{H}} = \frac{1}{6\Omega_0} \sum_{j=1}^{n_b} \left(F'(\bar{\rho}) \rho'(r_j) + \frac{1}{2} \phi'(r_j) \right) \frac{\mathbf{r}_j \otimes \mathbf{R}_j \otimes \mathbf{R}_j \otimes \mathbf{R}_j}{r_j} \ . \tag{5.13}$$

$$\mathbf{V} = \frac{\partial W}{\partial \mathbf{K}} = \frac{1}{24\Omega_0} \sum_{j=1}^{n_b} \left(F'(\bar{\rho}) \rho'(r_j) + \frac{1}{2} \phi'(r_j) \right) \frac{\mathbf{r}_j \otimes \mathbf{R}_j \otimes \mathbf{R}_j \otimes \mathbf{R}_j \otimes \mathbf{R}_j}{r_j} \ . \tag{5.14}$$

One may find that the stress tensor calculated based on the above Cauchy-Born rule depends on each grain's lattice orientation.

Remark 5.2.1 *We believe that the above discovered four intrinsic length scales in both FCC and BCC crystals exist in all other crystal solids. They not only have clearly physical meanings but also mathematical relevance in multiscale modeling. This multiscale structure regularize the first order Cauchy-Born rule based continuum formulations e.g. [83], in which the multiscale potential energy has multiple local minimum configurations at a local region. Thus the solution may not be unique, whereas the proposed MCDD model can stabilize the computation.*

Chapter 6

Finite Element Formulation

In this chapter, we discuss the formulation and implementation of the multiscale finite element formulation based on the proposed multiscale crystal defect dynamics (MCDD) theory.

6.1 Multiscale Finite Element Formulation

Let $\mathbf{u}(\mathbf{X}, t)$ and $\dot{\mathbf{u}}(\mathbf{X}, t)$ as the displacement and the velocity fields in the crystal continuum. We define the kinetic energy of the crystalline solid as,

$$\mathcal{T} = \int_V \frac{1}{2}\rho\dot{\mathbf{u}} \cdot \dot{\mathbf{u}} dV$$

where ρ is the mass density. We also denote the internal free-energy of crystal continuum as

$$\mathcal{W}_{int} := \int_V W(\mathbf{F}, \mathbf{G}, \mathbf{H}, \mathbf{K}) dV$$

where $W(\cdot)$ is the strain and strain gradient energy density. The Hamilton principle may then be written in terms of displacement variation for the fixed time interval between t_0 and t_1,

$$\delta \int_{t_0}^{t_1} (\mathcal{T} - \mathcal{W}_{int}) dt + \int_{t_0}^{t_1} \delta\mathcal{W}_{ext} dt = 0 \tag{6.1}$$

where $\mathcal{W}_{ext}$ is the external potential energy. The variation of kinetic energy is,

$$\delta\mathcal{T} = \int_V \rho\dot{\mathbf{u}} \cdot \delta\dot{\mathbf{u}} dV$$

and the internal virtual work is,

$$\delta\mathcal{W}_{int} = \int_V \left\{ \frac{\partial W}{\partial \mathbf{F}} : \delta\mathbf{F} + \frac{\partial W}{\partial \mathbf{G}} \vdots \delta\mathbf{G} + \frac{\partial W}{\partial \mathbf{H}} :: \delta\mathbf{H} + \frac{\partial W}{\partial \mathbf{K}} : \vdots \delta\mathbf{K} \right\} dV \tag{6.2}$$

By successive integration by parts of the above equation, one may obtain the following expression,

$$\begin{aligned}
\delta\mathcal{W}_{int} &= -\int_V \nabla_X \cdot \Big\{\mathbf{P} - \nabla_X \cdot \Big[\mathbf{Q} - \nabla_X \cdot \Big(\mathbf{U} - \nabla_X \mathbf{V}\Big)\Big]\Big\} \cdot \delta\boldsymbol{\varphi} dV \\
&+ \int_{\partial V} \Big\{\mathbf{N} \cdot \Big[\mathbf{P} - \nabla_X \cdot \Big(\mathbf{Q} - \nabla_X \cdot (\mathbf{U} - \nabla_X \cdot \mathbf{V})\Big)\Big]\Big\} \cdot \delta\boldsymbol{\varphi} dS \\
&+ \int_{\partial V} \Big\{\mathbf{N} \cdot \Big(\mathbf{Q} - \nabla_X \cdot (\mathbf{U} - \nabla_X \cdot \mathbf{V})\Big)\Big\} : \delta\mathbf{F} dS \\
&+ \int_{\partial V} \Big(\mathbf{N} \cdot (\mathbf{U} - \nabla_X \cdot \mathbf{V})\Big) \vdots \delta\mathbf{G} dS \\
&+ \int_{\partial V} \Big((\mathbf{N} \cdot \mathbf{V}\Big) :: \delta\mathbf{H} dS, \qquad (6.3)
\end{aligned}$$

which implies to the following form of natural boundary conditions,

$$\begin{aligned}
\bar{\mathbf{T}}_1 &= \mathbf{N} \cdot \Big\{\mathbf{P} - \nabla_X \cdot \Big(\mathbf{Q} - \nabla_X \cdot (\mathbf{U} - \nabla_X \cdot \mathbf{V})\Big)\Big\}, \quad \forall\, \mathbf{X} \in \partial V_t \qquad (6.4) \\
\bar{\mathbf{T}}_2 &= \mathbf{N} \cdot \{\mathbf{Q} - \nabla_X \cdot (\mathbf{U} - \nabla_X \cdot \mathbf{V})\}, \qquad \forall\, \mathbf{X} \in \partial V_t \qquad (6.5) \\
\bar{\mathbf{T}}_3 &= \mathbf{N} \cdot \{\mathbf{U} - \nabla_X \cdot \mathbf{V}\}, \qquad \forall\, \mathbf{X} \in \partial V_t \qquad (6.6) \\
\bar{\mathbf{T}}_4 &= \mathbf{N} \cdot \mathbf{V}, \qquad \forall\, \mathbf{X} \in \partial V_t\ , \qquad (6.7)
\end{aligned}$$

where $\mathbf{N}$ is the out-normal of the boundary ∂V_t.
Without lose of generality, for simplicity, we assume that on the boundary of the crystalline solid the higher order traction couple may be negligible, so that we may simplify the high order boundary conditions as,

$$\begin{aligned}
\bar{\mathbf{T}}_1 &= \mathbf{N} \cdot \Big\{\mathbf{P} - \nabla_X \cdot \Big(\mathbf{Q} - \nabla_X \cdot (\mathbf{U} - \nabla_X \cdot \mathbf{V})\Big)\Big\}, \quad \forall\, \mathbf{X} \in \partial V_t \qquad (6.8) \\
\bar{\mathbf{T}}_2 &\approx 0,\ \bar{\mathbf{T}}_3 \approx 0,\ and\ \ \bar{\mathbf{T}}_4 \approx 0, \qquad a.e. \quad \forall \mathbf{X} \in \partial V_t \qquad (6.9)
\end{aligned}$$

By doing so, the last three terms of the internal work may be neglected. Note that $\partial V = \partial V_t \bigcup \partial V_u$ and $\delta\boldsymbol{\varphi} = 0, \forall \mathbf{X} \in \partial V_u$.
Noting that the external virtual work of the system may be expressed as follows,

$$\delta\mathcal{W}_{ext} = \int_V \mathbf{b} \cdot \delta\mathbf{u} dV + \int_{\partial V_t} \bar{\mathbf{T}} \cdot \delta\mathbf{u} dS$$

where $\mathbf{b}$ is the body force, and $\bar{\mathbf{T}}$ is the traction vector on ∂V_t, one can derive the dynamics equations for the quasi continuous lattice system based on the Hamiltonian principle Eq.(6.1),

$$\nabla_X \cdot \Big(\mathbf{P} - \nabla_X \cdot [\mathbf{Q} - \nabla_X \cdot (\mathbf{U} - \nabla_X \cdot \mathbf{V})]\Big) + \mathbf{b} = \rho\ddot{\mathbf{u}},\ \forall \mathbf{X} \in V, \qquad (6.10)$$

with the boundary conditions: Eqs. (6.8) and (6.9).

Based on the strong form of the crystal defect dynamics equations (Eq. (6.10)), the Galerkin weak form of the MCDD may be written as

$$\begin{aligned}&\int_\Omega \Big[\rho\ddot{\mathbf{u}}\cdot\delta\mathbf{u}+\mathbf{P}:\delta\mathbf{F}+\mathbf{Q}\vdots\delta\mathbf{G}+\mathbf{U}::\delta\mathbf{H}+\mathbf{V}:\vdots\delta\mathbf{K}\Big]dV\\&=\int_\Omega \mathbf{b}\cdot\delta\mathbf{u}dV+\int_{\partial\Omega_t}\bar{\mathbf{T}}\cdot\delta\mathbf{u}dS\end{aligned}\tag{6.11}$$

The above expression is an generic form for every point in the domain. However, some of the higher order stresses and strain gradients are set to zero in the bulk elements or lower order process zone elements. Moreover, to avoid imposing higher order stress boundary condition, we either let them vanish at the boundary or simply avoid the higher order process element overlap with traction boundary $\partial_t\Omega_0$.
To take into account these factors, we rewrite Eq. (6.11) into the form of element Galerkin weak formulation,

$$\begin{aligned}&\sum_{e=1}^{n_{elem}^{p_0}}\left\{\int_{\Omega_{p_0}^e}\rho_0\ddot{\mathbf{u}}^h\cdot\delta\mathbf{u}^hdV+\int_{\Omega_{p_0}^e}\mathbf{P}:\delta\mathbf{F}^hdV\right\}\\+&\sum_{e=1}^{n_{elem}^{p_1}}\left\{\int_{\Omega_{p_1}^e}\rho_0\ddot{\mathbf{u}}^h\cdot\delta\mathbf{u}^hdV+\int_{\Omega_{p_1}^e}\Big(\mathbf{P}:\delta\mathbf{F}^hdV+\mathbf{Q}\vdots\delta\mathbf{G}^h\Big)dV\right\}\\+&\sum_{e=1}^{n_{elem}^{p_2}}\left\{\int_{\Omega_{p_2}^e}\rho_0\ddot{\mathbf{u}}^h\cdot\delta\mathbf{u}^hdV+\int_{\Omega_{p_2}^e}\Big(\mathbf{P}:\delta\mathbf{F}^h+\mathbf{Q}\vdots\delta\mathbf{G}^h+\mathbf{U}::\delta\mathbf{H}^h\Big)dV\right\}\\+&\sum_{e=1}^{n_{elem}^{p_3}}\left\{\int_{\Omega_{p_3}^e}\rho_0\ddot{\mathbf{u}}^h\cdot\delta\mathbf{u}^hdV+\int_{\Omega_{p_3}^e}\Big(\mathbf{P}:\delta\mathbf{F}^h+\mathbf{Q}\vdots\delta\mathbf{G}^h+\mathbf{U}::\delta\mathbf{H}^h+\mathbf{V}:\vdots\delta\mathbf{K}^h\Big)dV\right\}\\&=\sum_{i=0}^{3}\sum_{e_i=1}^{n_{elem}^{p_i}}\left\{\int_{\Omega_{p_i}^{e_i}}\rho_0\mathbf{b}\cdot\delta\boldsymbol{\varphi}^hdV\right\}+\sum_{e_0=1}^{n_{elem}^{p_0}}\int_{\partial_t\Omega_{p_0}^{e_0}}\bar{\mathbf{T}}\cdot\delta\boldsymbol{\varphi}^hdS\end{aligned}\tag{6.12}$$

where $\mathbf{b}$ is the body force, $\Omega_{p_i}^{e_i}$ is the e_i element in the p-th process zone, $\partial_t\Omega_{p_i}^{e_i}$ is the interception between the traction boundary and the boundary of the e_i-th element in the i-th process zone Ω_{p_i}.
In the computer implementation, we choose the following local finite element interpolation scheme in an element of the i-th order process zone,

$$\mathbf{u}^h(\mathbf{X},t)=\sum_{I_i=1}^{n_{d_i}}N_{I_i}(\boldsymbol{\zeta})\mathbf{d}_{I_i}(t),\quad i=0,1,2,3\tag{6.13}$$

where n_{d_i} is total number of nodes in the process zone element, and $i=0,1,2,3$ indicates the order of the process zone. Here we call the bulk crystal element as the 0^{th} order process

zone, the thin plate elements as the 1^{st} order process zone, the prism elements as the 2^{nd} order process zone, and the Wigner-Seitz vertex element as the 3^{rd} process zone. Note that all kinematic fields with the superscript 'h' are the fields derived from the FEA interpolation field rather than the exact value.
Substituting FE interpolation Eq. (6.13) into the weak forms Eqs. (6.11) and (6.12), one may derive the following discrete algebraic equations,

$$\mathbf{M}\ddot{\mathbf{d}} + \mathbf{f}^{int}(\mathbf{d}) = \mathbf{f}^{ext} \tag{6.14}$$

where

$$\mathbf{M} = \mathop{\boldsymbol{A}}_{e=1}^{n_{elem}} \int_{B_0^e} \rho_0 \mathbf{N}^{eT}\mathbf{N}^e dV$$

$$\mathbf{f}^{int} = \mathop{\boldsymbol{A}}_{e=1}^{n_{elem}} \left\{ \int_{B_0^e} \mathbf{B}^{eT}\mathbf{P}^e(\mathbf{d}) dV + \int_{C_0^e} \left[\mathbf{C}^{eT}\mathbf{Q}^e(\mathbf{d}) + \mathbf{D}^{eT}\mathbf{U}^e(\mathbf{d}) + \mathbf{E}^{eT}\mathbf{V}^e(\mathbf{d}) \right] dV \right\}$$

$$\mathbf{f}^{ext} = \mathop{\boldsymbol{A}}_{e=1}^{n_{elem}} \left\{ \int_{B_0^e} \mathbf{N}^{eT}\mathbf{b}^e dV + \int_{\partial_t B_0^e} \mathbf{N}^{eT}\bar{\mathbf{T}}^e dS \right\}$$

in which $\boldsymbol{A}$ is the element assembly operator (see [84]), $\mathbf{N}^e$ is the element shape function matrix, $\mathbf{B}^e$ is the element strain-displacement matrix, $\mathbf{C}^e, \mathbf{D}^e, \mathbf{E}^e$ is defined as following:

$$\mathbf{C}^e := \frac{\partial^2 \mathbf{N}^e}{\partial \mathbf{X} \otimes \partial \mathbf{X}}, \tag{6.15}$$

$$\mathbf{D}^e := \frac{\partial^3 \mathbf{N}^e}{\partial \mathbf{X} \otimes \partial \mathbf{X} \otimes \partial \mathbf{X}}, \tag{6.16}$$

$$\mathbf{E}^e := \frac{\partial^4 \mathbf{N}^e}{\partial \mathbf{X} \otimes \partial \mathbf{X} \otimes \partial \mathbf{X} \otimes \partial \mathbf{X}} \ . \tag{6.17}$$

The above FEM discretization is a generic form for every element. In this way, we can use a unified weak formulation for all elements. In actual numerical computations, we can set the higher order stress couples or strain gradients to zero inside the lower order process zone elements by letting $\mathbf{C}^e = 0, \mathbf{D}^e = 0$ and $\mathbf{E}^e = 0$ (see [27]).
On the other hand, in order to have non-zero valued $\mathbf{C}^e, \mathbf{D}^e$ and $\mathbf{E}^e$ matrices in the higher order process zone elements. The boundary integration, bubble mode, and p-version of finite element techniques are employed in the computer implementation. For detailed information, the readers may consult [32, 33, 85].
The explicit time integration is used to obtain the nodal velocities and displacements, which is based on the Newmark-β method with $\beta = 0$ and $\gamma = 0.5$ [86].

6.2 Implementation of Third Order Process Zone Element: Rhombic Dodecahedron

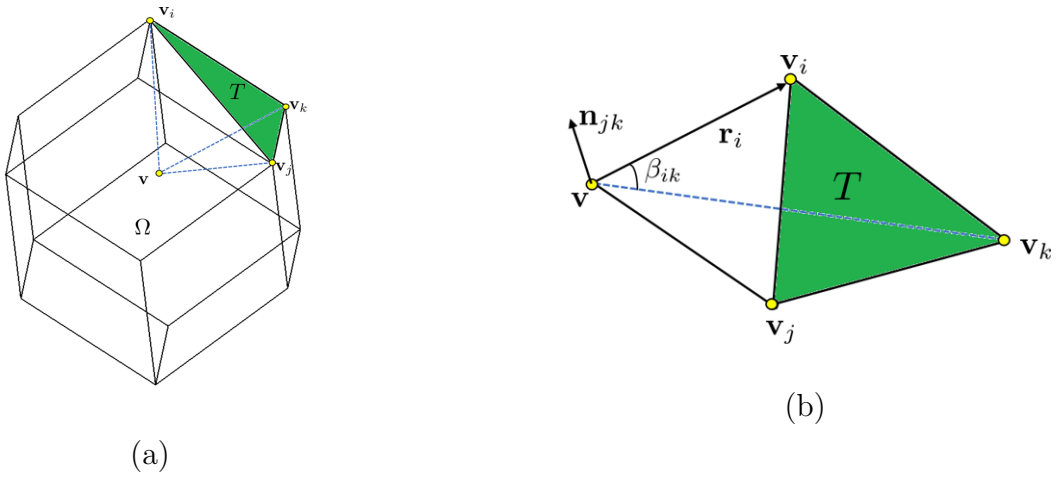

(a) (b)

Figure 6.1: FEM shape function of rhombic dodecahedron element with mean value coordinates: (a)overall view and (b)representation of tetrahedron.

In this section, we discuss the process of constructing finite element shape function for the dual cell of FCC lattice, which may provide a defect model for micro-voids and vacancies. Previously, we have used three-dimensional tetrahedron, pentahedron, and hexahedron elements to represent the bulk element (0^{th} order), 1^{st} and 2^{nd} order process zone elements. While the construction finite element interpolation function for the 3^{rd} order process zone element, which is a rhombic dodecahedron volume, is non-trivial.
In FEM implementation, we adopt the mean value coordinates[87] to construct the shape function for the 14-node rhombic dodecahedron. Considering a rhombic dodecahedron called Ω, we can pick a triangle $\mathbf{T}$ on the boundary of Ω (see: Fig. 6.1(a)). For any $\mathbf{v} \in \Omega$, each oriented triangle $[\mathbf{v}_i, \mathbf{v}_j, \mathbf{v}_k] \in \mathbf{T}$ defines a tetrahedron $[\mathbf{v}, \mathbf{v}_i, \mathbf{v}_j, \mathbf{v}_k]$ with positive volume. The shape function λ_i is then expressed as,

$$\lambda_i = \frac{w_i}{\sum_{j=1}^{14} w_j}, \tag{6.18}$$

where the weight function w_i is given by

$$w_i = \frac{1}{r_i} \sum_{T \ni \mathbf{v}_i} \mu_{i,T} \ , \tag{6.19}$$

in which $\mu_{i,T}$ is defined as

$$\mu_{i,T} = \frac{\beta_{jk} + \beta_{ij}\mathbf{n}_{ij} \cdot \mathbf{n}_{jk} + \beta_{ki}\mathbf{n}_{ki} \cdot \mathbf{n}_{jk}}{2\mathbf{e}_i \cdot \mathbf{n}_{jk}}, \tag{6.20}$$

where the unit vector $\mathbf{e}_i = (\mathbf{v}_i - \mathbf{v})/r_i$, $r_i = \| \mathbf{v}_i - \mathbf{v} \|$; $\beta_{ik} \in (0, \pi)$ is the angle between the two line segments $[\mathbf{v}, \mathbf{v}_i]$and $[\mathbf{v}, \mathbf{v}_k]$; and $\mathbf{n}_{ij}$ denotes the unit normal to the face $[\mathbf{v}, \mathbf{v}_i, \mathbf{v}_k]$, i.e. $\mathbf{n}_{ij} = (\mathbf{e}_i \times \mathbf{e}_j)/ \| \mathbf{e}_i \times \mathbf{e}_j \|$, which is pointing into the tetrahedron $[\mathbf{v}, \mathbf{v}_i, \mathbf{v}_j, \mathbf{v}_k]$ as shown in Fig. 6.1(b). For detailed derivations of above equations, interested readers are referred to Appendix C or [88, 87].

6.3 Size of Dodecahedron Element

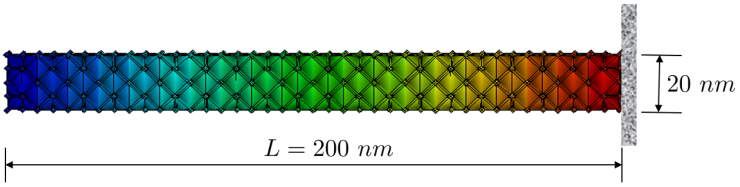

Figure 6.2: Setup of 1D wave propagation model.

One critical parameter in MCDD simulation is the scale factor for super lattice complex and the size of the third-order process zone element, which essentially determine the sizes of all process zone elements. The scale parameters β_1 and β_2 are shown in Fig. 3.1. In this dissertation, the ratio of β_1/β_2 is set as 10 and the size of dodecahedron element is varying. Considering the third-order process zone element is rhombic dodecahedron, so that the size depends on the edge length of each dodecahedron element. In order to find optimal size of the third-order process zone element, simulation of 1D wave propagation in a long thin plate (see Fig. 6.2). The boundary at the right side is fixed, and the left boundary is subjected a prescribed longitudinal displacement condition. The initial displacement $u(x, 0)$ is expressed by Gaussian wave as:

$$u(x, 0) = u_g \exp\Big(\frac{-x^2}{2\sigma_g^2}\Big), \tag{6.21}$$

where the values of u_g and σ_g are set as 0.2 and 10 nm, respectively.

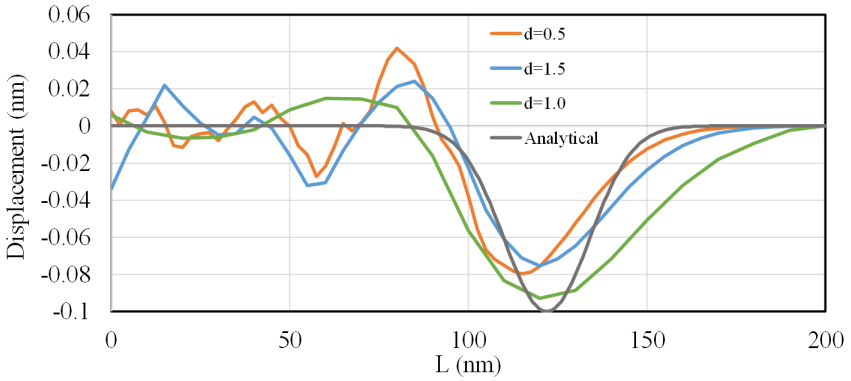

Figure 6.3: Wave shape before reflection at fixed boundary.

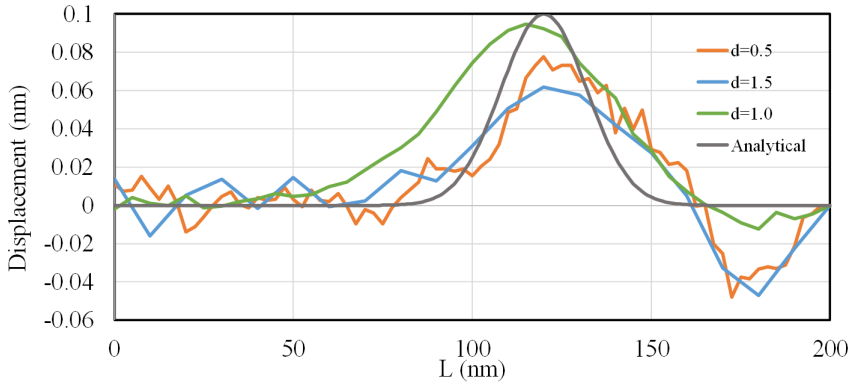

Figure 6.4: Wave shape after reflection after fixed boundary.

As shown in Fig. 6.3 and Fig. 6.4, the edge length of $d = 0.5\ nm$ causes much oscillations before and after the wave reflection at the fixed boundary. When d increases to 1 nm, the displacement becomes smooth. However, several sharp turning points occur if d is increased to 1.5 nm. Therefore, for the edge length of each dodecahedron element we may choose its edge length in the order of 1 nm.

Chapter 7

Numerical Analysis

In order to validate the proposed MCDD method, in this chapter we present several numerical examples of MCDD simulations and compare the results of MCDD simulations with that of molecular dynamics simulation.

7.1 Crack Propagation

In the first example, we present a study of three-scale process zone modelling and simulation of crack propagation in a 2D plate of single crystal copper. The bulk crystal element is treated as the zero-th order process zone, i.e. a non-defect identity; The interphase zone is modeled as the first order process zone, and the potential void zone as the second order process zone. The simulation specimen and its boundary condition are shown in Fig. 7.1.

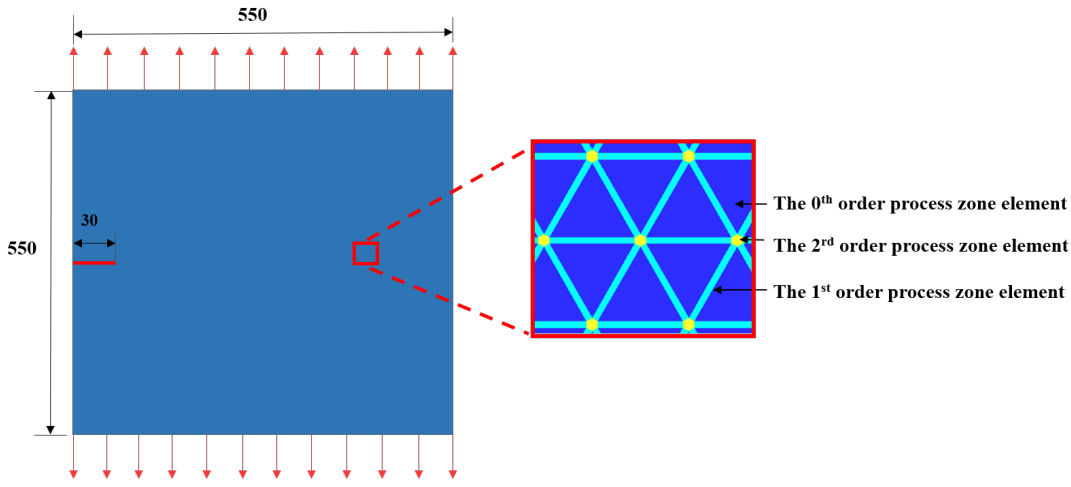

Figure 7.1: Schematic illustration of 2D plate and multiscale process zone mesh.

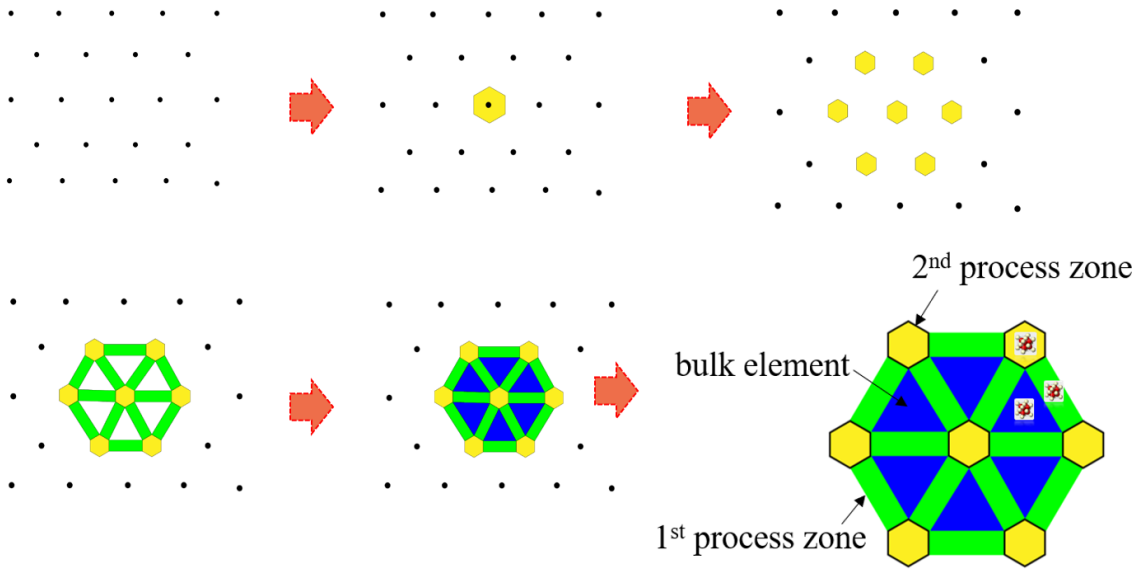

Figure 7.2: The process of process zone tiling: (1) yellow region: the 0-th order process zone, (2) blue region: the 1st process zone, and (3) green region: the 2nd process zone.

To validate MCDD method, the simulation results are compared with that of corresponding molecular dynamics simulation [89]. Since the (111) plane is the most susceptible slip plane in the FCC single crystal, so that the material on (111) plane must be weaker than that of bulk crystals. Therefore we would like to study the crack propagation within the (111) plane. As shown in Fig. 7.1, a high strain rate boundary condition is prescribed to initiate mode-I fracture. The finite element mesh contains the 0th (triangular element), 1st (rectangular element) and 2nd (honeycomb element) order process zone elements, which are shown in the zoomed region of Fig. 7.1. Details of process zone mesh are provided in Fig. 7.2. At each vertex, there is one triangle, two rectangles and one hexagon. In this example, it is assumed that bulk elements only contain uniform deformations, which are described by the first-order Cauchy-Born rule. The rectangular and honeycomb elements can support non-uniform deformations, which are modeled by the second-order and third-order Cauchy-born rules.

7.1.1 Embedded atom method (EAM) potential

In this example, an analytical EAM potential is adopted to describe material constitutive relation in the fracture simulation [89]. The EAM potential is explicitly given as,

$$W = \frac{1}{\Omega_0}\sum_{i=1}^{n_b}[(1-\chi)F(\bar{\rho}_i) + \frac{1}{2}\chi\sum_{j\neq i}\phi(r_{ij})], \quad \bar{\rho}_i = \sum_{j\neq i}\rho(r_{ij}), \tag{7.1}$$

where χ is a weighting parameter between zero and one; the parameter $\chi = \frac{1}{3}$ is set based on the embedded atom method [90]; $F(\bar{\rho})$ is the embedded energy function; and $\phi(r)$ is the pairwise interaction function, whose expression can be written as follows:

$$F(\bar{\rho}) = \epsilon \frac{d(d+1)}{2} e\bar{\rho} \ln \bar{\rho} \tag{7.2}$$

and

$$\phi(r) = \begin{cases} \chi\psi(r), & r < r_{spl} \\ \chi \left\{ \psi(r_{spl}) + \dfrac{\partial \psi}{\partial r}(r_{spl})(r - r_{spl}) - \dfrac{1}{6} A (r - r_{max})^3 \right\}, & r_{spl} \le r < r_{max} \\ 0, & r_{max} \le r \end{cases} \tag{7.3}$$

where r_{spl} is the reflection point in the potential; r_{max} is the cutoff distance; and the potential function can be of different types based on specific problems. In this example, we choose

$$\psi(r) = \epsilon \left[\left(\frac{r_0}{r} \right)^{12} - 2 \left(\frac{r_0}{r} \right)^6 \right], \tag{7.4}$$

and the constant A in Eq. (7.3) is defined as

$$A = \frac{8(\frac{\partial \psi}{\partial r}(r_{spl}))^3}{9(\psi(r_{spl}))^2} \tag{7.5}$$

where ϵ is the depth of the potential well, and r_0 is the equilibrium distance. The inflection point r_{spl} can be obtained by solving the following equation

$$\frac{\partial^2 \psi}{\partial r^2}(r_{spl}) = 0 \ . \tag{7.6}$$

A solution of r_{spl} may be found as $r_{spl} = 1.244455 r_0$. The cutoff distance is given by

$$r_{max} = r_{spl} - \frac{3\psi(r_{spl})}{2\frac{\partial \psi}{\partial r}(r_{spl})} \ . \tag{7.7}$$

A practical value of r_{max} in numerical computation is found as $r_{max} = 1.547537 r_0$. The electron density function is given by

$$\rho(r) = \begin{cases} \dfrac{\bar{\rho}_0}{d(d+1)} (\dfrac{r_{max}^2 - r^2}{r_{max}^2 - 1})^2 & 0 < r < r_{max} \\ 0 & r_{max} \le r \end{cases} \tag{7.8}$$

where $\bar{\rho} = \sum_j \rho(r_j); \bar{\rho}_0 = 1/e$, and d is the dimensionality.

For easy reference, the material parameters used in this example, the depth of the potential well ϵ and the equilibrium distance r_0 for copper, are listed in Table. 7.1, in which a comparison between the numerical value and the experimental measured value [91] is made.

Table 7.1: Material parameters for copper

Parameter		Experiment	EAM-Holian
C_{1111}	$[GPa]$	169	168.2
C_{1122}	$[GPa]$	122	117.5
C_{1212}	$[GPa]$	75.3	83.2
ϵ	$[eV]$	—	0.43894774
r_0	[Å]	—	2.57110688

7.1.2 Barycentric finite element method and its quadrature rule

For finite element implementation, linear triangular shape functions are adopted for the bulk element, bilinear quadrilateral shape functions with bubble mode are selected for the first-order process zone element, and the shape functions for the hexagonal elements are employed in the second-order process zone. Implementing the hexagonal element and calculating the strain gradient field inside is not a trivial task.

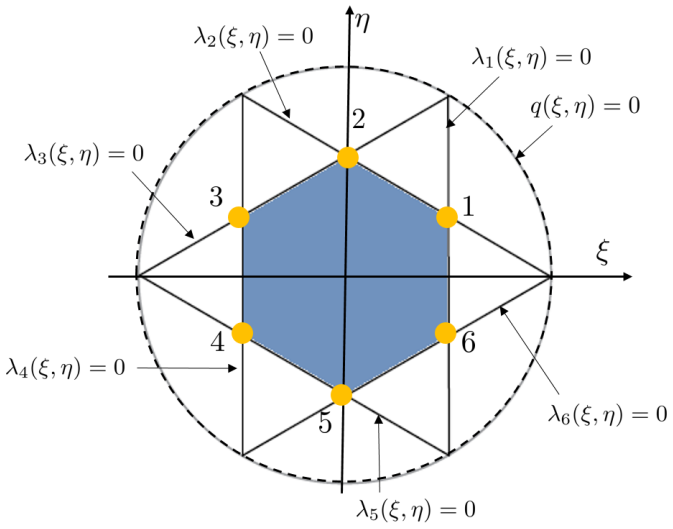

Figure 7.3: The Washspress shape function for the honeycomb element.

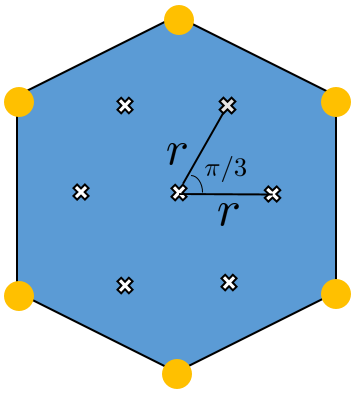

Figure 7.4: Schematic illustration of the quadrature rule for the regular hexagonal element.

In this work, the 6-point honeycomb Wachspress element [92] is used to model the second-order process zone. The local finite element interpolation field is as follows:

$$\mathbf{u}(X,Y,t) = \sum_{I=1}^{6} N_I(\xi,\eta)\mathbf{u}_I(t) \tag{7.9}$$

Let Ω_e denote the regular hexagonal domain (see Fig. 7.3). The shape function N_i, corresponding to node i is given by:

$$N_i(\xi,\eta) = c_i \frac{\lambda_{i+2}(\xi,\eta)\lambda_{i+3}(\xi,\eta)\lambda_{i+4}(\xi,\eta)\lambda_{i+5}(\xi,\eta)}{q(\xi,\eta)}, i = 1,2,3,4,5,6 \tag{7.10}$$

where $\lambda_{i+1}(\xi,\eta) = 0$ represents the line segment connecting i and $i+1$. A circumference circle

$$q(\xi,\eta) = \xi^2 + \eta^2 - R^2 = 0 \tag{7.11}$$

encompasses the points of intersection of the extensions of the edge. The normalizing factor is defined as:

$$c_i = \frac{q(\xi_i,\eta_i)}{\lambda_{i+2}(\xi_i,\eta_i)\lambda_{i+3}(\xi_i,\eta_i)\lambda_{i+4}(\xi_i,\eta_i)\lambda_{i+5}(\xi_i,\eta_i)} \tag{7.12}$$

For the numerical integration of hexagonal element, the symmetric quadrature rules are adopted, which are proposed by Lyness and Monegato [93]. As illustrated in Fig. 7.4, the quadrature rule is invariant under 60° rotation due to the hexagonal symmetry of the integration region, which can be expressed:

$$\int_{\Omega_e} f d\Omega = \omega_0 f(0,0) + \sum_{j=1}^{N}\sum_{i=1}^{6} \omega_j f(r_j, \alpha_j + \frac{\pi i}{3}) \tag{7.13}$$

where ω_j denotes the weight corresponding to the Gauss point at distance r_j from the center of the hexagon and angle $\alpha_j + \frac{\pi i}{3}$ from the horizonal axis for $1 \leqslant i \leqslant 6$. In this work, $N = 1$

is chosen, which has 7 quadrature points including the point in the center, as shown in Fig. 7.4.

The simulation domain is discretized into 82,212 nodes, 27,404 bulk elements, 40,873 first-order process zone elements, and 13,470 second-order process zone elements. Comparing with the full molecular dynamics simulation, the reduction ratio in the number of degrees of freedom is about 1-to-4. A pre-notched crack is set in the specimen, which has an initial length 30 in the reduced unit. The time increment of time integration is 0.0033 ps, and the constant velocity applied at top and bottom is $0.03r_0/t$, which is consistent with the strain rate of 1.12×10^{-4} in [89]. Fig. 7.5 shows the simulation results of stress distribution during crack propagation.

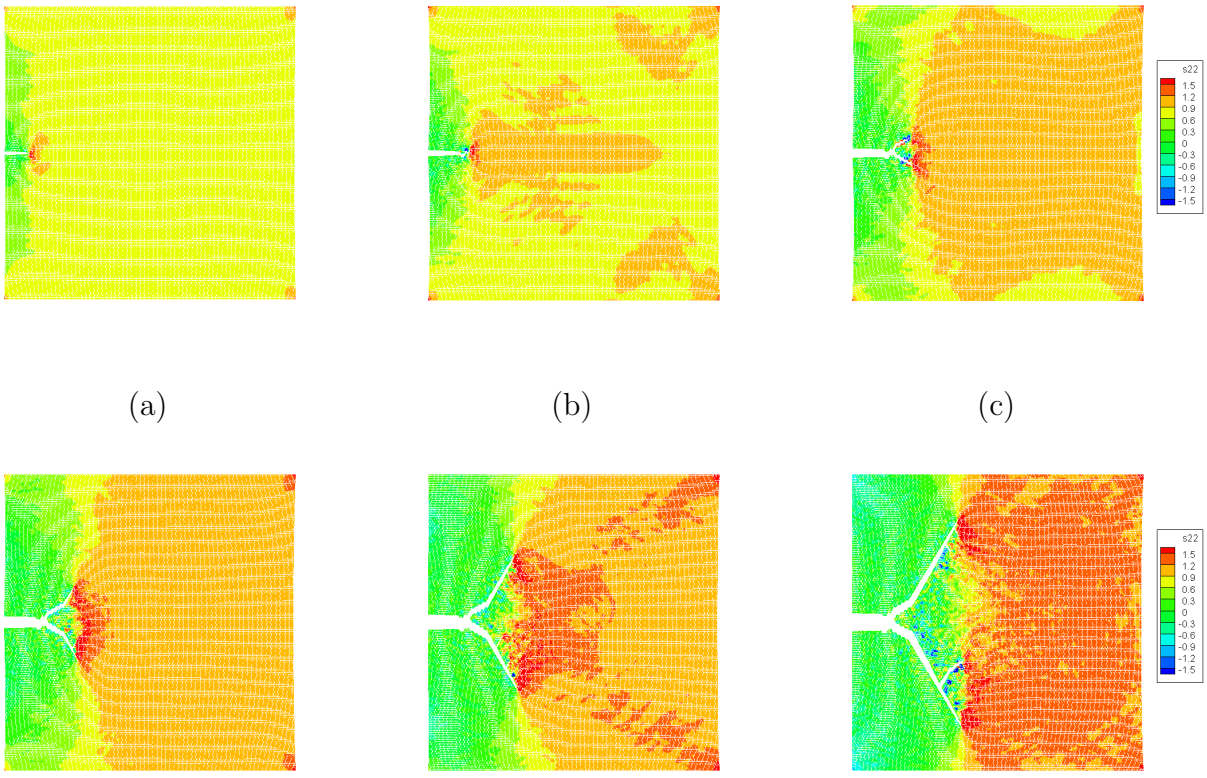

Figure 7.5: Stress distributions in a crack propagation sequence.

It is not difficult to find that at beginning the crack propagates horizontally and then it bifurcates due to the perturbation of acoustic wave reflected from the boundary. It can be noticed that the crack demonstrates unsymmetry between the bottom and top portion, which may be caused by high nonlinearity and instability of the simulated example. Moreover,

Fig. 7.6 compares the crack speed history in this present work with that obtained in a MD simulation[89]. The agreement is very good except that process zone model predicts a slightly late crack growth. The crack speed can be compared with the speed of shear wave or Rayleigh wave in this specimen. Considering the material constants given in Table. 7.1, the shear wave and Rayleigh wave speed are 2895 m/s and 2666 m/s, respectively[94]. The ratio of peak crack speed to Rayleigh wave speed is about 0.4, which is comparatively low compared to the ratio of 0.8 in Linder and Armero [95, 96] and 1.0 in Falk et al.[97]. One of the reasons lies in that the work of [95, 96] considers the materials as isotropic, which may result in certain difference with the materials described by EAM potential in this dissertation.

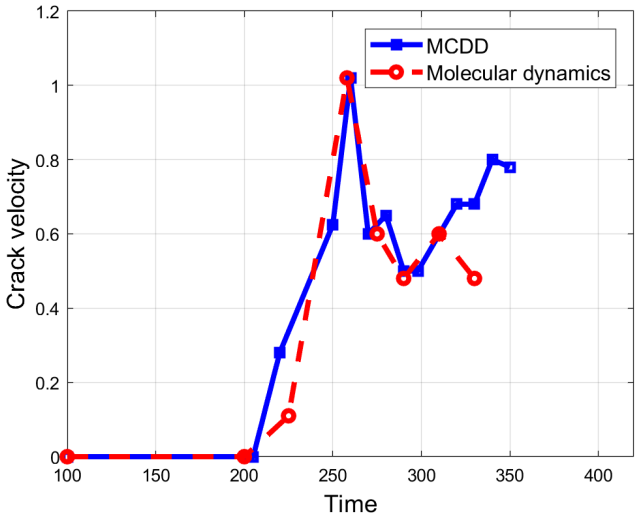

Figure 7.6: Crack speed comparison between MCDD model and molecular dynamics.

7.2 Uniaxial Deformation and Simple Shear

To verify the effectiveness of MCDD method, a simple benchmark test was conducted by comparing the stress-strain relation of uniaxial deformation with MD simulation. The length of simulation cubic is $10nm$, which includes 280 bulk elements, 256 wedge elements(first-order process zone), 78 prism elements (second-order process zone) and 13 rhombic dodecahedron elements(third-order process zone). The edge length of MD model is $10nm$, which comprises about 88 thousands atoms. Constant velocity boundary conditions are applied at the top and bottom boundary with strain rate $10^{-2}/ps$, as shown in Fig. 7.7.

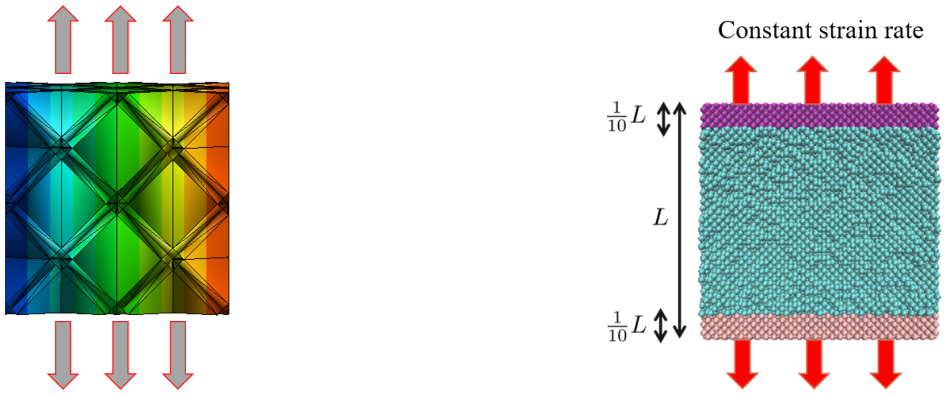

(a) (b)

Figure 7.7: A simple benchmark test of uniaxial stretch: (a) finite element mesh of MCDD specimen and (b) initial atom configuration of the MD cell.

The comparison of stress-strain relation in uniaxial loading and unloading with MD simulation is shown in Fig. 7.8(a). In this figure, the constitutive relations of bulk element are always simulated by the first-order Cauchy-Born rule. '1st order' means the constitutive relations of process zone element are simulated by first-order Cauchy-Born rule, while '2nd order' represents process zone element are simulated by the second-order Cauchy-Born rule and '3rd order' represents the second and third order process zone element are simulated by using the third-order Cauchy-Born rule.

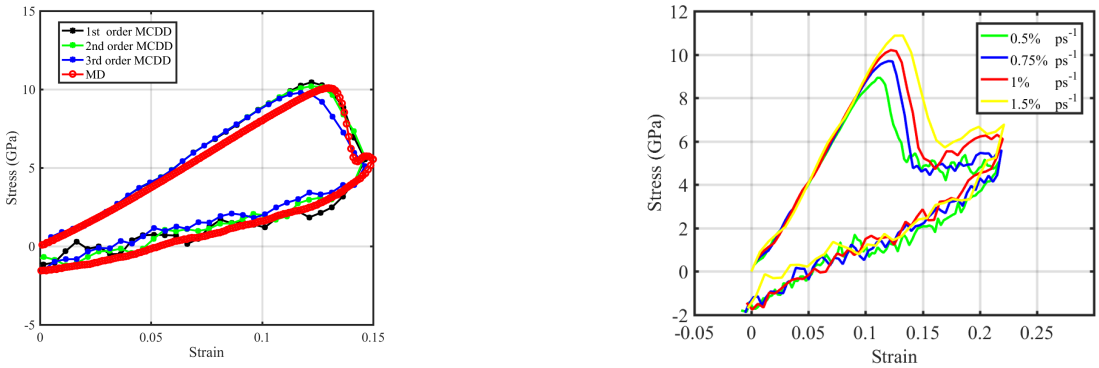

(a) (b)

Figure 7.8: (a) Comparison of the simulated stress-strain relations obtained from MCDD and MD under the uniaxial loading and unloading condition and (b) stress-strain relations at different strain rates from MCDD.

Fig. 7.8(a) shows that the yield stress value obtained by using the first-order Cauchy-Born

based stress-strain relation is the highest, that obtained from the stress-strain relation based on the second-order Cauchy-Born rule is second highest, and that obtained from the stress-strain relation based on the third-order Cauchy-Born rule is the lowest. This implies that the third order process zone element will always fail first. This tendency is consistent with the benchmark test reported in [27]. In addition, permanent strain can be observed in the unloading part of the stress-strain relation, which proves that MCDD method has the ability to simulate inelastic deformation as MD does. To the best of the authors' knowledge, it may be the first time that we can use the Cauchy-Born rule based multiscale method to simulate inelastic deformation without any empirical constitutive data. Fig. 7.8(b) shows stress-strain relations at different strain rates obtained by using MCDD, which implies the yield stress increases with the increase of the strain rate.

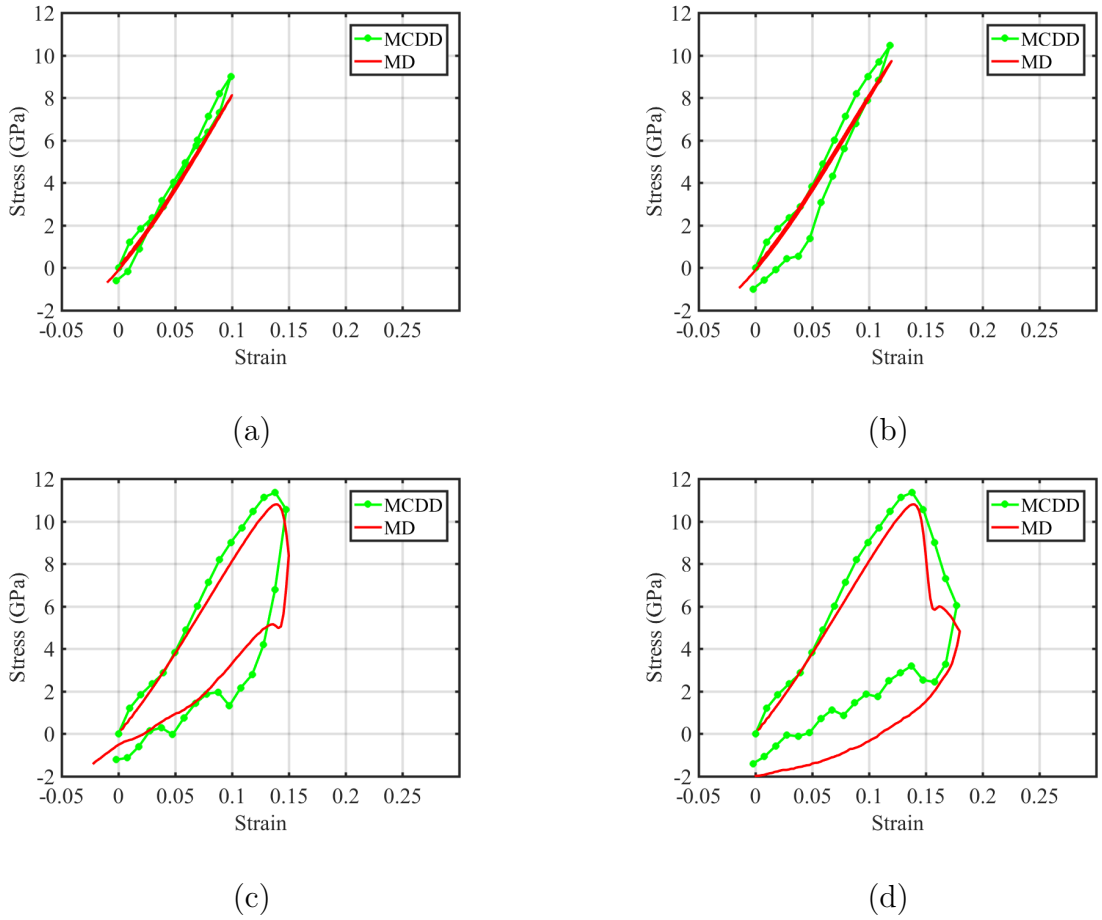

Figure 7.9: Comparison of the simulated stress-strain relations obtained from MCDD and MD under the uniaxial loading and different unloading strain: (a) unloading at 10 % relative strain, (b) unloading at 12 % relative strain, (c) unloading at 15 % relative strain, and (d) unloading at 18 % relative strain.

Fig. 7.9 also shows stress-strain hysteresis relation at different unloading strain levels, which are obtained by using the second order Cauchy-Born rule. These results clearly indicate that MCDD method is able to capture mesoscale plastic deformation and history-dependent constitutive behaviors.

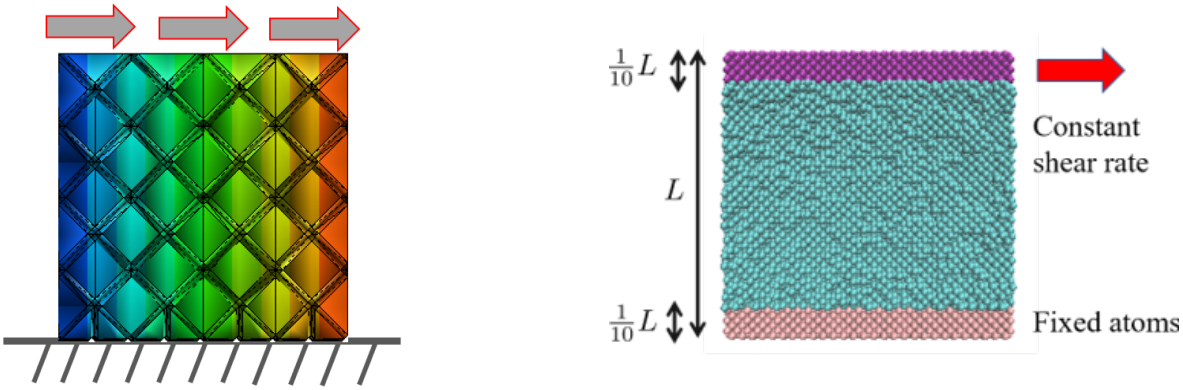

(a) (b)

Figure 7.10: A benchmark test of simple shear: (a) finite element mesh of MCDD specimen and (b) initial atom configuration of the MD cell.

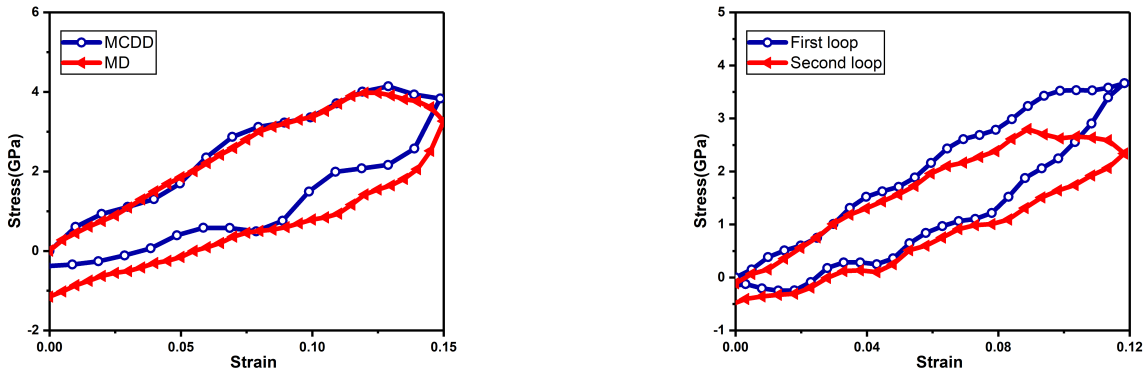

(a) (b)

Figure 7.11: (a) Comparison of strain-stress curve of shear with MD and MCDD and(b) strain-stress curve of shear loop.

Fig. 7.10 shows the boundary conditions of simple shear model, where horizonal velocity is applied at the top boundary. The comparison of stress-strain relation with MD simulation are shown in Fig. 7.11(a), which shows good agreement with MD simulation. Fig. 7.11(b)

shows the difference of stress-strain relation for the first and second loop, which indicates that MCDD may be able to simulate the mechanism of fatigue. Clearly the numerical results have demonstrated that MCDD method can be used to simulate inelastic deformation and may be capable of simulating fatigue deformation.

7.3 Nanoindentation in Copper

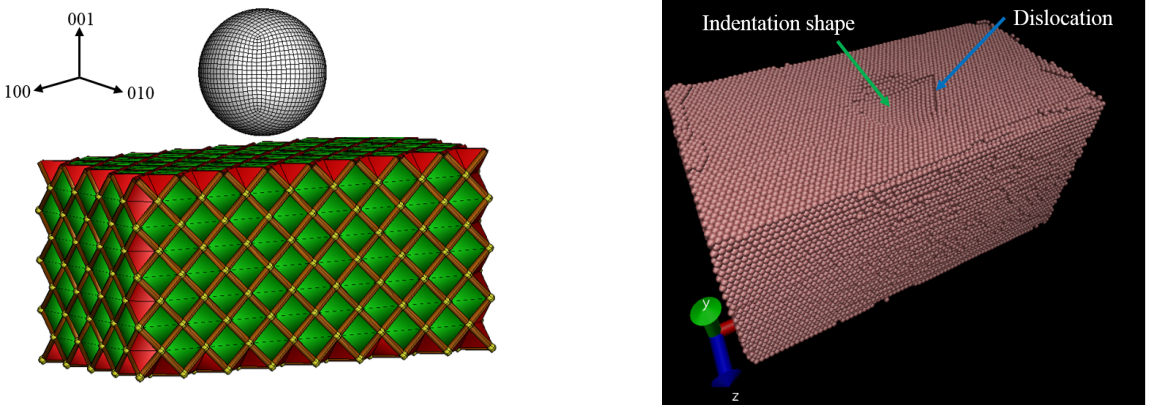

(a) (b)

Figure 7.12: MCDD nanoindentation simulation: (a) MCDD simulation set-up and (b) configuration of the MD simulation.

In this numerical example, MCDD is employed to simulate a three-dimensional nanoindentation of single crystal copper, which had been carefully studied in the numerical simulations by using both molecular dynamics as well as interatomic potential finite element method (FEM) [98, 99]. In order to compare with the numerical results obtained in a molecular dynamics simulation [98], we use the same EAM Mishin potential for copper (see: [100]) in the MCDD simulation. The pair part of the EAM Mishin potential is given as,

$$\begin{aligned}\phi(r) = &[E_1 M(r, r_0^{(1)}, \alpha_1) + E_2 M(r, r_0^{(2)}, \alpha_1) + \delta]\psi(\frac{r - r_c}{h}) \\ &- \sum_{n=1}^{3} H(r_s^{(n)} - r) S_n (r_s^{(n)} - r)^4\end{aligned} \tag{7.14}$$

where

$$M(r, r_0, \alpha) = \exp[-2\alpha(r - r_0)] - 2\exp[-\alpha(r - r_0)]$$

is the Morse function,$H(\cdot)$ is the Heaviside function and the cut-off function for the pair potential is defined as,

$$\psi(x) = \begin{cases} 0 & x \geq 0 \\ \dfrac{x^4}{(1+x^4)} & x < 0 \end{cases} \tag{7.15}$$

The last term in Eq.(7.14) is used to control the strength of pairwise repulsion between atoms at short distances. Here, $E_1, E_2, r_0^{(1)}, r_0^{(2)}, \alpha_1, \alpha_2, \delta, r_c, h, r_s^{(1)}, r_s^{(2)}, r_s^{(3)}, S_1, S_2$ and S_3 are the material parameters. The electron density function is given in the form

$$\rho(r) = [a\ \exp(-\beta_1(r - r_0^{(3)})^2) + \exp(-\beta_2(r - r_0^{(4)})^2)]\psi(\frac{r - r_c}{h}) \tag{7.16}$$

where $a, r_0^{(3)}, r_0^{(4)}, \beta_1$ and β_2 are additional material parameters. The embedding function for the EAM-Mishin potential is given as follows,

$$F(\bar{\rho}) = \begin{cases} F^0 + \frac{1}{2}F^2(\bar{\rho}-1)^2 + \sum_{n=1}^{4} q_n(\bar{\rho}-1)^{n+2} & \bar{\rho} < 0 \\ \dfrac{F^0 + \frac{1}{2}F^2(\bar{\rho}-1)^2 + q_1(\bar{\rho}-1)^3 + Q_1(\bar{\rho}-1)^4}{1 + Q_2(\bar{\rho}-1)^3} & \bar{\rho} > 1 \end{cases} \tag{7.17}$$

where $F^{(0)}, F^{(2)}, q_1, q_2, q_3, q_4, Q_1$ and Q_2 are the additional materials parameters. For clarity, the values of the twenty eight material parameters are shown in Table 7.2.

In this numerical example, 3D simulations of nanoindentation by a rigid spherical indenter is performed for the purpose to demonstrate the capacity of MCDD to capture and quantify the critical state of dislocation nucleation as a direct numerical simulation (DNS). The set-up of the numerical experiment is shown as in Fig. 7.12. The simulation-based prediction is given as to when and where the dislocation will nucleate within the crystal, and which oriented crystal slip and stacking fault will take place. In simulations, the spherical indenter is modeled as a frictionless and analytic rigid sphere, and the rigid spherical indenter is pressed onto the (111), (110) and (100) surfaces of single crystal copper. The size of the substrate of copper is $20nm \times 20nm \times 40nm$, and the radius of the rigid indenter is $9nm$. The following boundary conditions are imposed to the copper specimen: the displacements at the bottom of the specimen are constrained to be zero, while the displacements of lateral surfaces are constrained in the normal directions. The coarse grained contact model [101]is adopted to simulate the contact between the indenter and the substrate.

Coarse grained contact model

This section gives a brief description of how to derive the equations in coarse grained contact model, which is employed to capture the macroscopic interaction between deformable solids considering the microscopic interactions between individual atoms or molecules in adjacent bodies[102]. As shown in Fig. 7.13, there are two bodies, Ω_1 and Ω_2 occupying the

Table 7.2: Material parameters of EAM-Mishin for copper[100]

Parameter	Value	Parameter	Value
r_c[Å]	5.50679	$S_3[eV/Å^4]$	1.15000×10^3
h[Å]	0.50037	a	3.80362
$E_1[eV]$	2.01458×10^2	$r_0^{(3)}$[Å]	-2.19885
$E_2[eV]$	6.59288×10^{-3}	$r_0^{(4)}$[Å]	-2.61984×10^2
$r_0^{(1)}$[Å]	0.83591	$\beta_1[Å^{-1}]$	0.17394
$r_0^{(2)}$[Å]	4.46867	$\beta_2[Å^{-1}]$	5.35661×10^2
$\alpha_1[Å^{-1}]$	2.97758	$F_0[eV]$	-2.28235
$\alpha_1[Å^{-1}]$	1.54927	$F_2[eV]$	1.35535
$\delta[eV]$	0.86225×10^{-2}	$q_1[eV]$	-1.27775
$r_s^{(1)}$[Å]	2.24000	$q_2[eV]$	-0.86074
$r_s^{(2)}$[Å]	1.80000	$q_3[eV]$	1.78804
$r_s^{(3)}$[Å]	1.20000	$q_4[eV]$	2.97571
$S_1[eV/Å^4]$	4.00000	Q_1	0.40000
$S_2[eV/Å^4]$	40.00000	Q_1	0.30000

physical domains. The 12-6 Lennard-Jones potential is used to represent inter-body particle interaction in this dissertation as follows:

$$\phi(r) = \epsilon \left[(\frac{\sigma_0}{r})^2 - 2(\frac{\sigma_0}{r})^6 \right] \tag{7.18}$$

where ϵ is the potential well and σ_0 is the equilibrium distance. Then the overall interaction potential energy summing up all the particles in these two bodies can be expressed as:

$$\Pi^c = \int_{\Omega_1} \int_{\Omega_2} \beta_1 \beta_2 \phi(r) dv_1 dv_2 \tag{7.19}$$

where β_1 and β_1 denote the particle densities for arbitrary points $x_1 \in \Omega_1$ and $x_2 \in \Omega_2$. The contact force between two infinitesimal volume dv_1 and dv_2 can be expressed as

$$d\mathbf{f} = -\beta_1 \beta_2 \frac{\partial \phi(r)}{\partial \mathbf{x}_1} dv_1 dv_2 = \beta_1 \beta_2 \frac{\partial \phi(r)}{\partial \mathbf{x}_2} dv_1 dv_2 \tag{7.20}$$

where $\mathbf{x}_1$ and $\mathbf{x}_2$ are position vectors of arbitrary particles in body Ω_1 and Ω_2, respectively. The total contact force between Ω_1 and Ω_2 requires the double volume integration. Then it is not difficult to notice that the interaction force density in Ω_2 due to Ω_1 can be expressed as:

$$\hat{\mathbf{b}}_2 = \int_{\Omega_1} \frac{d\mathbf{f}}{dv_2} dv_1 = \int_{\Omega_1} \beta_1 \beta_2 \frac{\partial \phi(r)}{\partial \mathbf{x}_2} dv_1 \tag{7.21}$$

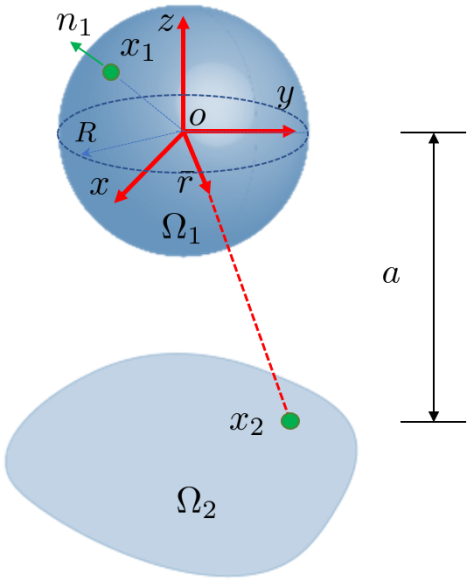

Figure 7.13: Schematic of the coarse-grained contact model between rigid sphere and deformable domain.

In this work, Ω_1 is a rigid sphere, the analytic solution by integrating over Ω_1 can be derived as follows.

$$\begin{aligned}\hat{\mathbf{b}}_2 &= \int_{\Omega_1} \beta_1\beta_2 \frac{\partial\phi(r)}{\partial \mathbf{x}_2} dv_1 \\ &= \int_0^{2\pi}\int_0^{\pi} \beta_1\beta_2 R^2 sin\psi\phi(r)\mathbf{n}_1 d\psi d\theta \\ &= 8\beta_1\beta_2 R^3\pi a {r_0}^6\epsilon \frac{[-5(a^2-R^2)^6 + 2(a^2+R^2)(5a^4+22a^2R^2+5R^4){r_0}^6]}{5(a^2-R^2)^{10}}\bar{\mathbf{r}}\end{aligned} \tag{7.22}$$

where R is the radius of rigid body Ω_1, a is the distance between the sphere center of Ω_1 and arbitrary particle in Ω_2. r_0 is the equilibrium distance of inter-body particle interaction. $\bar{r}$ is the unit vector that connect the sphere center to the any point in Ω_2. It will reduce the double volume integration to only one-layer volume integration and save computational resources.

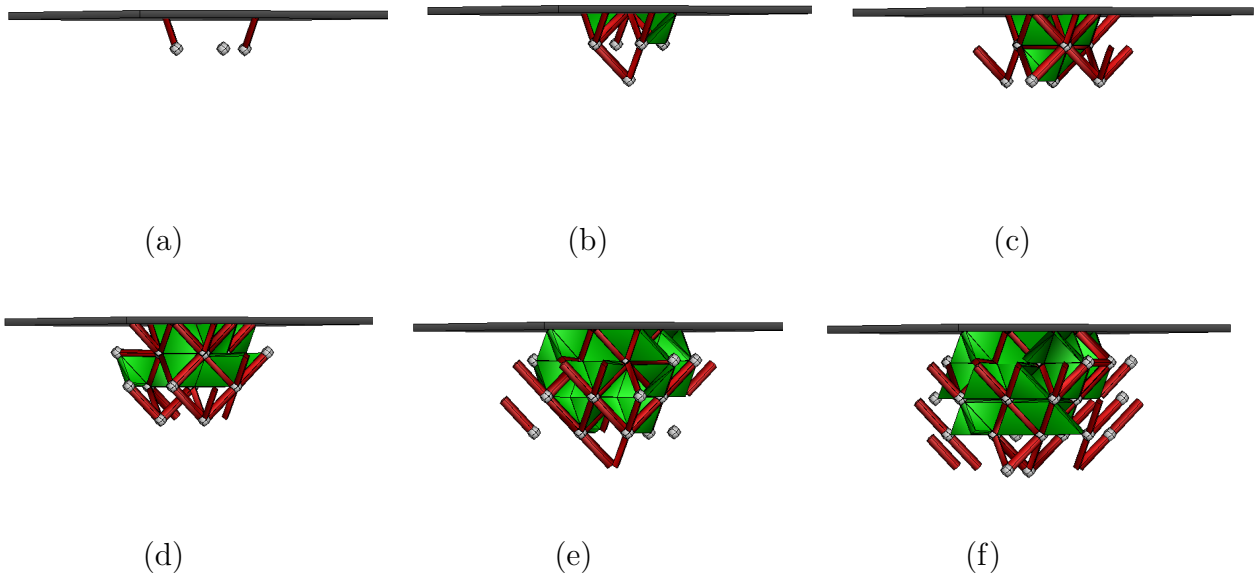

Figure 7.14: MCDD simulation results: dislocation loop (blue) and stacking fault (green) formation in the copper substrate during the indentation.

The substrate mesh comprises 5952 bulk elements (0th-order process zone), 4096 wedge elements(first-order process zone), 3264 prism elements (second-order process zone) and 612 rhombic dodecahedron elements(third-order process zone). The indenter is moved down in displacement control at a very low rate. Fig. 7.14 shows the 3D dislocation loop and slip planes during the indentation process. The dislocation loops are in red and the corresponding slip planes are in green, which follow the direction of the effective strain.
Molecular Dynamics(MD) simulation of nanoindentation in copper is conducted using LAMMPS [103] to compare the results with that of MCDD. The dimension of copper substrate is $20nm \times 20nm \times 40nm$, which comprises about 1.4 million atoms. The loading rate is 0.05 Å $/ps$ and the indentation depth is 20 Å. The simulation temperature is 10K and the time step is $0.002ps$. In this work,we have exploited the fact that a centrosymmetric material (such as FCC crystals) will remain centrosymmetric under homogeneous elastic deformation[104]. In a centrosymmetric material, each atom has pairs of equal and opposite bonds to its nearest neighbors. As the material is distorted, these bonds will change direction and length, but they will remain equal and opposite. When a defect appears nearby, this equal and opposite relation no longer holds for all of the nearest-neighbor pairs. Thus we can define a centrosymmetry parameter which is zero for a centrosymmetric material under any homogeneous elastic deformation but nonzero for any plastic deformation of the material. The centrosymmetry parameter for each atom is defined as follows [103]:

$$CS = \sum_{i=1}^{N/2} \mid \mathbf{R}_i + \mathbf{R}_{i+N/2} \mid^2 \tag{7.23}$$

where N is the number of nearest neighbours, $\mathbf{R}_i$ and $\mathbf{R}_{i+N/2}$ are vectors from the central atom to a particular pair of nearest neighbors. For an atom on a lattice site, surrounded by atoms on a perfect lattice, the centrosymmetry parameter will be 0. It will be near 0 for small thermal perturbations of a perfect lattice. If a point defect exists, the symmetry is broken, and the parameter will be a larger positive value. An atom at a surface will have a large positive parameter. Fig. 7.12 (b) displays the indentation shape and dislocation distribution in the single crystal of copper. As can be seen from Fig. 7.12 (b), indentation shape of the $9nm$ radius spherical indenter is shown by green line and edge dislocation by a blue line.

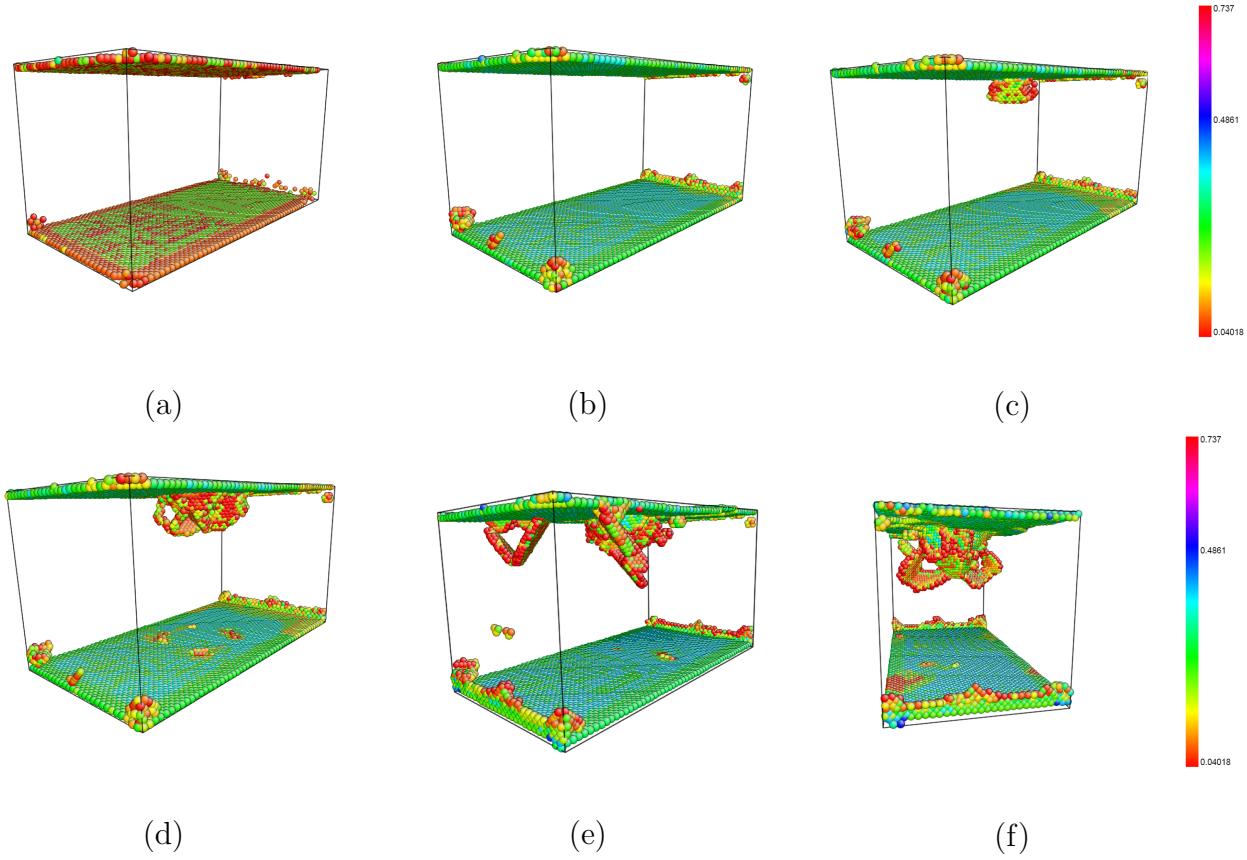

Figure 7.15: Formation and movement of dislocation loops and crystal slips beneath the indenter.

In Fig. 7.15, the process for the formation and movement of the dislocations beneath the indenter is shown by using the software Atomeye [82]. In this figure, only the atoms for which the number of neighbors does not correspond to that of a perfect FCC crystal are plotted. The atoms are colored according to the value of the centrosymmetry parameter with range $0.040 \sim 0.74$. After an elastic deformation of the volume (Fig. 7.15 (a) and(b)), defects appear beneath the indenter (Fig. 7.15 (c)). This structure is unstable and rapidly

transforms into intrinsic defects (see: Fig. 7.15 (d)) finally becomes several distinct loops of dislocations (see: Fig. 7.15 (e) and(f)).
In Fig. 7.16, the load displacement curves for nanoindentation in single crystal copper is compared with that of molecular dynamics. Sudden drops in load value can be attributed to the nucleation of dislocation. The comparison curve shows a good agreement in general, which reveals that MCDD can predict dislocation nucleation induced elastic instability just as MD simulations. It is noticed that several other factors will also have influences on the dislocation nucleation of nanoindentation [98], such as surface orientation effects, indentation depth and initial density effects, which will be investigated in the following work.

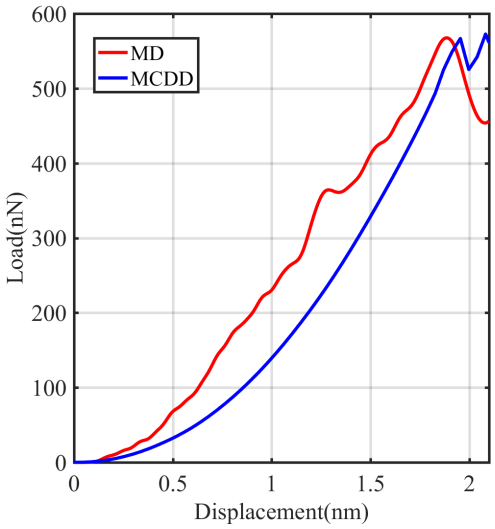

Figure 7.16: Comparison of load-displacement curves obtained from MCDD and MD simulations of nanoindentation in copper.

7.4 Crystal Slip and Dislocation Nucleation around a Void

In this numerical example, the MCDD method is employed to simulate the three-dimensional dislocation motion and crystal slip around a void in a copper specimen.

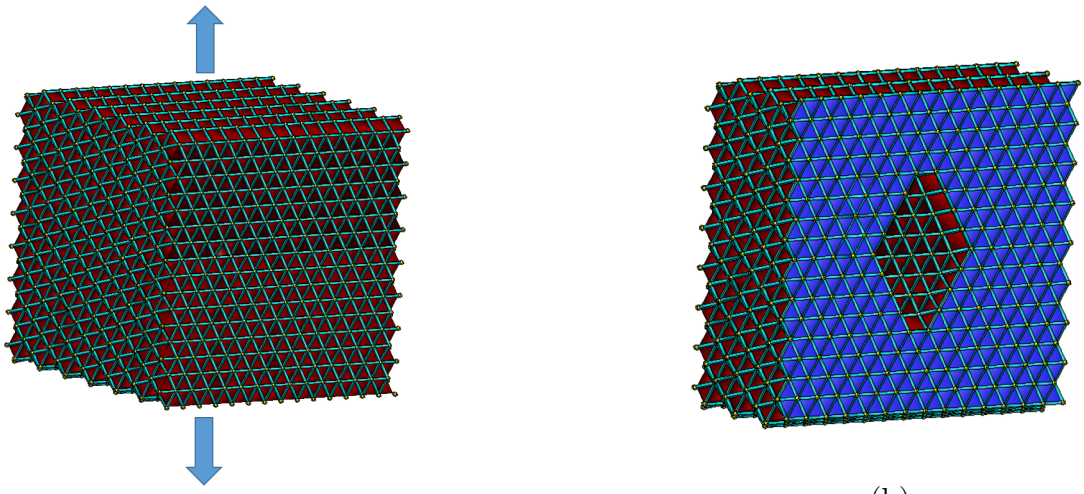

(a) (b)

Figure 7.17: Schematic of single crystal copper specimen: (a)the view of uniaxial tension and (b) half mesh with a rhombohedral void.

Fig. 7.17 presents the MCDD models of single crystal copper specimens with a rhombohedral void initially introduced in the interior. The dimension of copper is $50nm \times 50nm \times 50nm$ in copper, which contains about 43 million atoms. The dimension of the void is $13nm \times 13nm \times 9nm$. The FEM mesh comprises 54468 bulk elements(0th-order process zone), 30118 wedge elements(first-order process zone), 25603 prism elements (second-order process zone), and 4797 rhombic dodecahedron elements(third-order process zone). The EAM Mishin potential [100] is adopted for modelling copper, which is the same potential used in the indentation example of this chapter. The view of this model with the displacement controlled boundary conditions applied at the bottom and top boundary is shown in Fig. 7.17(a). The displacement is applied at a constant velocity of $100m/s$. Fig. 7.18 shows the dislocation and stacking fault of copper in MCDD simulations, which has similar dislocation shape as shown in [105]. Fig. 7.19 shows the load displacement curve of uniaxial tension in copper. This curve has obvious linear elastic range, yielding stage, and work-harding range, which shows the characteristics of ductile material.

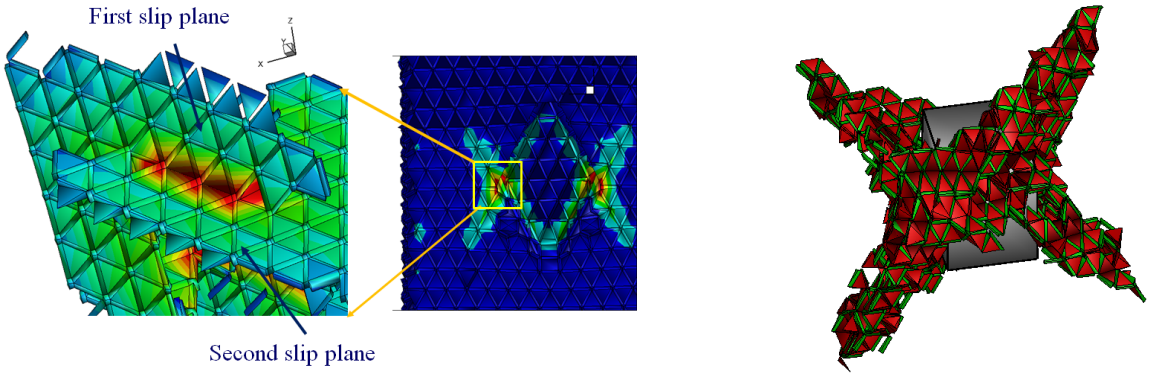

(a) (b)

Figure 7.18: MCDD simulation results: (a) slip planes and (b) dislocation loops in the copper specimen.

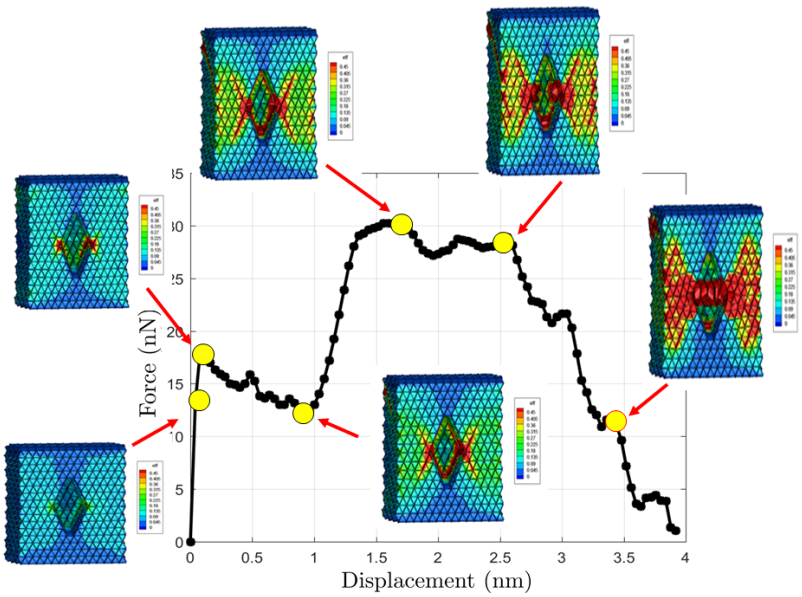

Figure 7.19: Load-displacement curve of uniaxial tension of a copper specimen with an inside void.

7.5 Crystal Orientation Effects on Dislocation Nucleation at Grain Scale

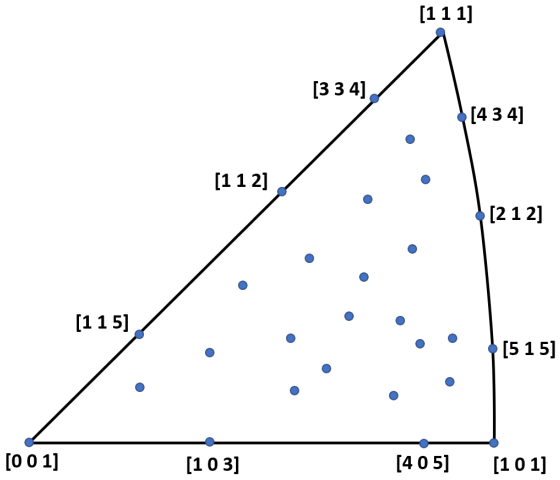

Figure 7.20: Stereographic triangle showing the 29 crystallographic orientations. Each direction represents the uniaxial loading axis for single crystal deformation simulation.

To demonstrate MCDD is an atomistically-determinant crystal plasticity theory, MCDD is employed to simulate anisotropic plasticity at grain scale and to study the influence of crystal orientation on dislocation nucleation and slip system activation.
Crystal plasticity is a theory of anisotropic inelastic deformation theory, and crystal material behaviors depend on crystal microstructure and hence external load axis orientation. In the classical Taylor crystal plasticity, dislocation motion in single crystals is thought to be governed by the critical resolved shear stress (CRSS) via Schmids law [106]. However, Taylor crystal plasticity theory may still be considered as a phenomenological theory because the value of CRSS is either given on an empirical base, or taken from the fine scale first principle simulation, and it is not within the framework of crystal plasticity itself. Moreover, the classical plasticity may not be able to capture some fundamental aspects of the physical phenomenon, i.e. the non-Schimid stress.
In this work, 3D computational model is used to investigate crystal plasticity and dislocation nucleation in single crystal copper under uniaxial tension and compression(Fig. 7.20). A constant strain rate of $10^9/s$ is applied in the loading direction. The dimensions are chose with a minimum length of $16nm$ to reduce the effects of boundary conditions [107, 108, 109].

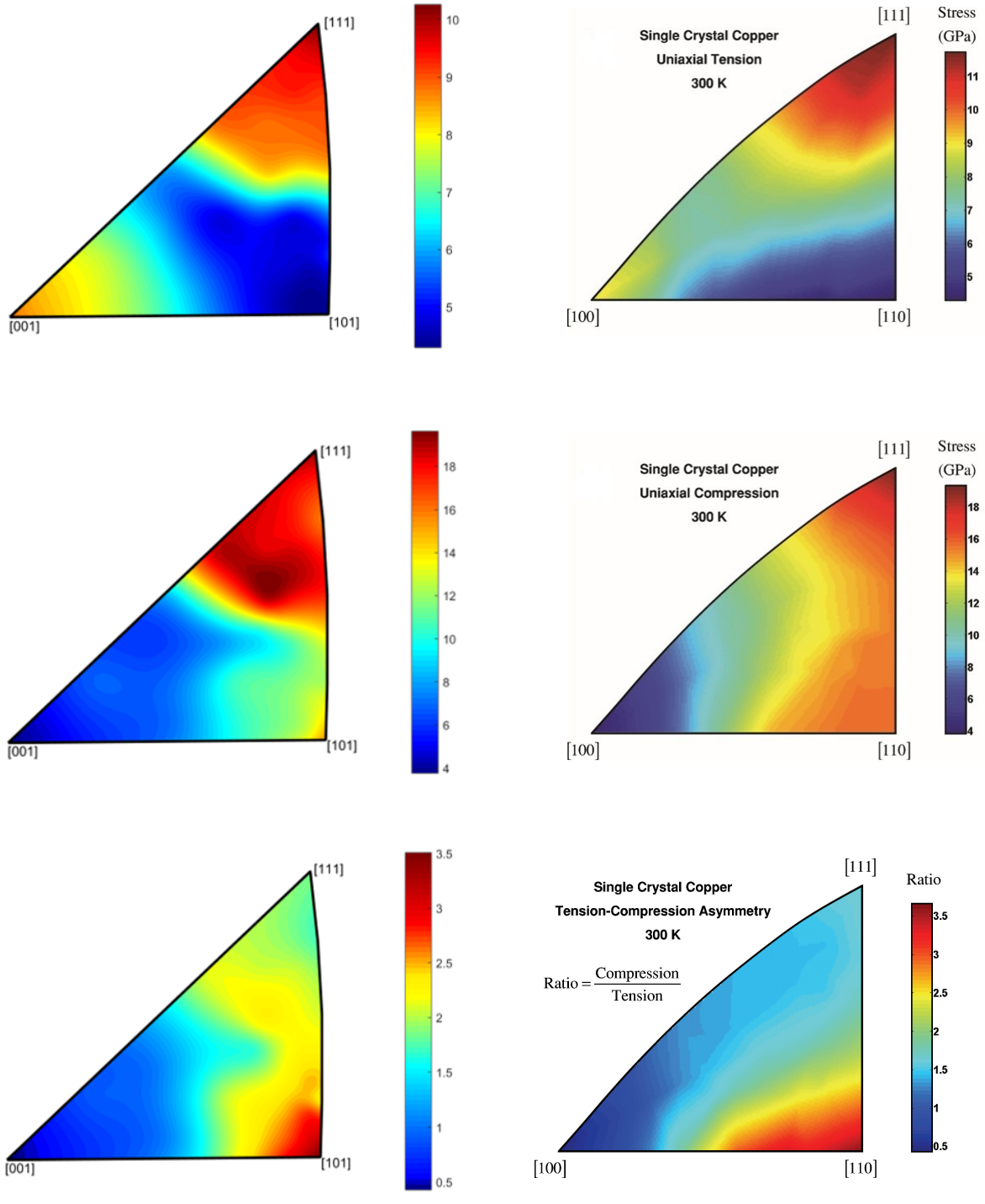

(a) (b)

Figure 7.21: Comparison of contour plots of tensile stress, compressive stress and the ratio of compressive stress and tensile stress: (a)results of MCDD and (b) MD results[107]. (Reuse permission by AIP Publishing LLC: License Number 4324321505819)

Fig. 7.21(a) displays the results of molecular dynamics simulations of crystal plasticity, in which the yield stress and ratio of compression with tension over different crystal orientations under tensile/compression loadings are plotted, which are related to the tensile and compression stress required for homogeneous dislocation nucleation at different loading orientations. Fig. 7.21(b) displays the MD simulation of the crystallographic orientation [107], which shows good agreement with that of MCDD. This example shows that MCDD is capable of simulating atomistically-determinant crystal plasticity.

7.6 Shear Band Formulation with Uniaxial Loading

To simulate the formulation of shear band, a copper specimen with size $16nm \times 16nm \times 40nm$ is investigated. A constant velocity (corresponding to a strain rate on the order of $10^{10}/s$)is applied at the top and bottom boundary along the [001] direction Fig. 7.22(a).Strain is defined as a nominal quantity based on the overall imposed specimen displacement and comparison is conducted with full MD simulation. As shown in Fig. 7.22(b), both MCDD and MD simulation shows that dislocation nucleation occurs at around strain 12% and stress $10GPa$. In addition, Fig. 7.23 shows the formulation of shear band in (111) plane, which is the corresponding slip plane for FCC crystal. This example shows that MCDD has the ability to simulate dislocation nucleation and shear band formulation.

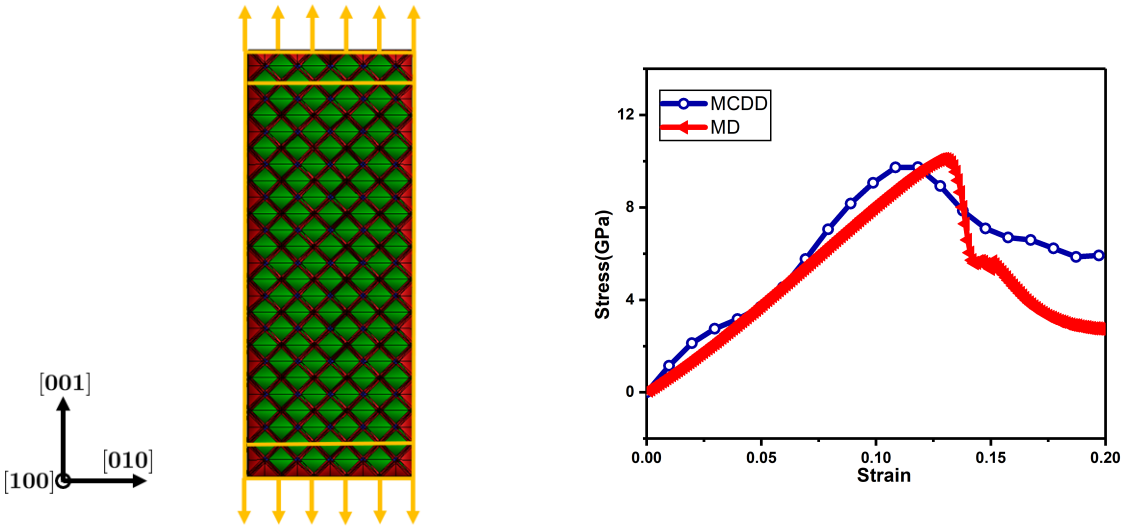

(a) (b)

Figure 7.22: (a)Mesh of column and (b)strain-stress curve with uniaxial loading.

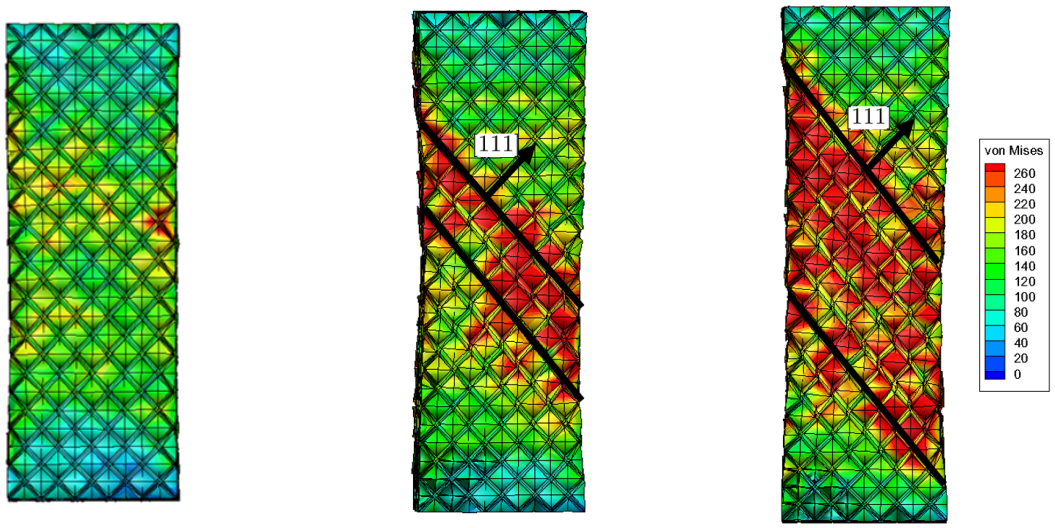

(a) (b) (c)

Figure 7.23: Formulation process of shear band in (111) plane with strain (a) 2%, (b)15%, (c)15%, and (d)25%.

Chapter 8

Conclusions and Outlook

In this dissertation, a novel multiscale crystal defect dynamics (MCDD) model is proposed. The MCDD model can directly link atomistic information with long-range order dislocation pattern dynamics, so that it allows us to establish an atomistically-determined crystal plasticity theory based on microstructures and dislocation pattern dynamics of the original perfect crystal.

The multiscale crystal defect dynamics (MCDD) model only considers the motions of all the geometrically admissible defects in a given crystal based on its microstructure. This is a much focused, exclusive, and disruptive approach. The philosophy of MCDD model is that not every defect will present in a given crystal, and we only need to study a few types of defects that are related to the microstructure of the crystal. More precisely speaking, for a given crystal, it is only prone to a few types of defects that are related to their microstructure, and if we embed those few types of defect modes as defect process zones into a multiscale finite element model, we may predict material responses based on multiscale simulations.

Moreover, there are a few advantages of MCDD method over some other defect mechanics models, e.g. dislocation dynamics. For instance, formation of voids is a well known consequence of radiation damage in materials, and these voids can pin down the motion of dislocations. Thus interaction between voids and dislocation plays a vital role in dictating the mechanical behaviour of crystalline solids (e.g. [110]). On the other hand, work hardening during plastic deformation of a crystal is associated with significant changes in dislocation microstructure. The increase in dislocation density on the specimen is accompanied by the spontaneous emergence of regions of low dislocation density and clusters of high dislocation density which to a large extent persist upon unloading. These metastable structures are denoted as dislocation patterns. The fundamental hypothesis of MCDD is that these dislocation microstructure depend on the original crystal microstructure, and one may identify possible defect pattern regions by geometrical analysis of the original crystal lattice.

The use of discrete exterior calculus and algebraic topology to study crystal defects is not new [26, 111]. One of the motives of the previous discrete lattice mechanics is to utilize lattice complex cell structure to provide the lower order defect models, i.e. 0-cell (void), 1-cell

(dislocation), and 2-cell (slip plane). In this work, we take a completely different approach, and we view all defects as three-dimensional objects. Nevertheless, we employ the discrete exterior calculus and algebraic topology to study the super lattice of the original crystal structure to classify all the admissible three-dimensional defects. The most dual lattices of the 3D Bravais lattice structure are Bravais lattices, but the coarse-grained super lattice proposed in this work is not a Bravais lattice, because it uses the vertices of the dual cell as the motif to form a non-Bravais lattice. We believed that the non-Bravais super lattice structure may represent the physical microstructure of the defects in real crystal lattice. Since the microstructure of the dual-lattice depends on the microstructure of the original perfect lattice, there are only a limited types of defects that are geometrically admissible to a given crystal. From this perspective, we may view the microstructure of the non-Bravais super lattice as the possible defected "genes" for a given crystalline material. If we can model the evolution of these "genetic" defects, we can then predict the material properties of the crystal at macroscale. In fact, as the coarse-graining parameters $\beta_1 \to 1$ and $\beta_2 \to 0$, the present lattice defect model will degenerate to that proposed in [26, 111].

MCDD can relate the size-dependent plastic deformation to fundamental physics of defects, i.e. nucleation, multiplication, annihilation, interactions and transport of dislocations and vacancies. It is an atomistically-determined formulation while preserving the continuum character. MCDD model transcends length scale directly from nano meter scale to millimeter scale, which does not need any hierarchical modeling and computations.

As an atomistic-informed continuum formulation, MCDD preserves the well-possed mathematical structure of continuum physics by describing the problem as a rigorous initial-boundary value problem in terms of partial differential equations. Moreover, MCDD multiscale formulation minimizes ad-hoc assumptions and free parameters as used extensively in strain-gradient and other scale-dependent plasticity theories

The spontaneous emergence of heterogeneous dislocation patterns is a conspicuous feature of plastic deformation and strain hardening of crystalline solids. Currently, almost all dislocation pattern theories are empirical continuum theory. The proposed multiscale crystal defect dynamics theory is derived based on atomistic molecular dynamics through systematic coarse graining procedures, and hence its physical modeling fidelity is significantly improved over other dislocation pattern models as well as discrete dislocation dynamics, while retaining almost the same or even less computation cost.

Last, we would like to stress that the proposed MCCD theory is a coarse graining defect model, which is formulated in a non-Bravais super lattice. However, the underline crystal (physical) lattice is still Bravais, as we have studied so far. One can easily extend the proposed MCDD formulation to non-Bravais physical lattices by employing the corresponding Cauchy-Born rule for the non-Bravais lattice [112, 113].

Of course, there are a few aspects that need further investigation. The first one is the modelling of thermally-activated plastic flow. It is directly related to plasticity dissipation mechanism, high temperature creep fatigue mechanism, which has broader applications in high temperature materials and material failure under high strain rates. In order to couple the mechanical field with temperature, the harmonic approximation based thermal mechani-

cal Cauchy-Born rule may be adopted [114]. In addition, the proposed MCDD model can be extended to model polycrystalline solids, which requires the consideration of grain boundary. In each single grain, we shall use the standard MCDD formulation outlined in previous section, in which the high-order Cauchy-Born rules are used to evaluated stresses in different process zones. What is new in this case is the grain boundary element. In these elements, the Cauchy-Born rules can be applied to evaluate stresses. However, the underline lattice cell will not be the original crystal lattice, but a quasi-crystal lattice structure that can accommodate the perfect crystal at both sides of the grain boundary, which usually have different orientations. Experimental and theoretical evidences have suggested that the structures of many grain boundaries are quasicrystals, consisting of an aperiodic sequence of structural units which have a deflation symmetry[115]. The Cauchy-Born rule can be extended to quasicrystal or non-crystalline amorphous solids to model the grain boundary [116, 85].

Bibliography

[1] J.P. Sethna, M.K. Bierbaum, K.A. Dahmen, C.P. Goodrich, J.R. Greer, L.X. Hayden, J.P. Kent-Dobias, E.D. Lee, D.B. Liarte, X. Ni, et al. Deformation of crystals: Connections with statistical physics. *Annual Review of Materials Research*, 47, 2017.

[2] R.I. Stephens, A. Fatemi, R.R. Stephens, and H.O. Fuchs. *Metal fatigue in engineering*. John Wiley & Sons, 2000.

[3] M.P. Groover. *Fundamentals of modern manufacturing: materials processes, and systems*. John Wiley & Sons, 2007.

[4] J. Schiøtz and K.W. Jacobsen. A maximum in the strength of nanocrystalline copper. *Science*, 301(5638):1357–1359, 2003.

[5] H. Lv, H. Jiang, H. Liu, and J. Shi. Boundary effect on the plasticity and stress of lithiated silicon: First-principles calculations. *Journal of Applied Physics*, 112(10):103509, 2012.

[6] I. Shin and E.A. Carter. First-principles simulations of plasticity in body-centered-cubic magnesium–lithium alloys. *Acta Materialia*, 64:198–207, 2014.

[7] Z. Yuan, H. Cui, and X. Guo. First-principle calculation on mechanical and thermal properties of b2-nisc with point defects. *Journal of Semiconductors*, 38(1):012001, 2017.

[8] V. Dupont and F. Sansoz. Molecular dynamics study of crystal plasticity during nanoindentation in ni nanowires. *Journal of Materials Research*, 24(3):948–956, 2009.

[9] T. Fu, X. Peng, C. Wan, Z. Lin, X. Chen, N. Hu, and Z. Wang. Molecular dynamics simulation of plasticity in vn (001) crystals under nanoindentation with a spherical indenter. *Applied Surface Science*, 392:942–949, 2017.

[10] S. Chandra, M.K. Samal, V.M. Chavan, and R.J. Patel. Multiscale modeling of plasticity in a copper single crystal deformed at high strain rates. *Plasticity and Mechanics of Defects*, 1(1), 2015.

[11] J.D. Clayton. Continuum multiscale modeling of finite deformation plasticity and anisotropic damage in polycrystals. *Theoretical and Applied Fracture Mechanics*, 45(3):163–185, 2006.

[12] Y. Aoyagi and K. Shizawa. Multiscale crystal plasticity modeling based on geometrically necessary crystal defects and simulation on fine-graining for polycrystal. *International Journal of Plasticity*, 23(6):1022–1040, 2007.

[13] Y. Aoyagi. Multiscale crystal plasticity modeling considering nucleation of dislocations based on thermal activation process on ultrafine-grained aluminum. *IOP Conference Series: Materials Science and Engineering*, 194:012048, 2017.

[14] D. Weygand, M. Mrovec, T. Hochrainer, and P. Gumbsch. Multiscale simulation of plasticity in bcc metals. *Annual Review of Materials Research*, 45:369–390, 2015.

[15] M. Wallin, W.A. Curtin, M. Ristinmaa, and A. Needleman. Multi-scale plasticity modeling: Coupled discrete dislocation and continuum crystal plasticity. *Journal of the Mechanics and Physics of Solids*, 56(11):3167–3180, 2008.

[16] V. Bulatov, F. F. Abraham, L. Kubin, B. Devincre, and S. Yip. Connecting atomistic and mesoscale simulations of crystal plasticity. *Nature*, 391(6668):669–672, 1998.

[17] D. L. McDowell. Viscoplasticity of heterogeneous metallic materials. *Materials Science and Engineering R: Reports*, 62(3):67–123, 2008.

[18] H. M. Zbib and T. Diaz de la Rubia. A multiscale model of plasticity. *International Journal of Plasticity*, 18(9):1133–1163, 2002.

[19] L. E. Shilkrot, R. E. Miller, and W. A. Curtin. Coupled atomistic and discrete dislocation plasticity. *Physical review letters*, 89(2):025501, 2002.

[20] L. E. Shilkrot, W. A. Curtin, and R. E. Miller. A coupled atomistic/continuum model of defects in solids. *Journal of the Mechanics and Physics of Solids*, 50(10):2085–2106, 2002.

[21] L. E. Shilkrot, R. E. Miller, and W. A. Curtin. Multiscale plasticity modeling: Coupled atomistics and discrete dislocation mechanics. *Journal of the Mechanics and Physics of Solids*, 52(4):755–787, 2004.

[22] M. Dewald and W. A. Curtin. Analysis and minimization of dislocation interactions with atomistic/continuum interfaces. *Modelling and Simulation in Materials Science and Engineering*, 14(3):497–514, 2006.

[23] R. E. Miller, L. E. Shilkrot, and W. A. Curtin. A coupled atomistics and discrete dislocation plasticity simulation of nanoindentation into single crystal thin films. *Acta Materialia*, 52(2):271–284, 2004.

[24] B. Devincre and M. Condat. Model validation of a 3D simulation of dislocation dynamics:Discretization and linear tension effects. *Acta Metallurgica et Materialia*, 40:2629–2637, 1992.

[25] N. Ghoniem, S.-H. Tong, and L. Sun. Parametric dislocation dynamics: A thermodynamics-based approach to investigations of mesoscopic plastic deformation. *Physical Review B*, 61:913–927, 2000.

[26] M.P. Ariza and M. Ortiz. Discrete crystal elasticity and discrete dislocations in crystals. *Archival Rational Mechanics and Analysis*, 178:149–226, 2005.

[27] S. Li, B. Ren, and H. Minaki. Multiscale crystal defect dynamics: a dual-lattice process zone model. *Philosophical Magazine*, 94(13):1414–1450, apr 2014.

[28] X. Zeng and S. Li. A multiscale cohesive zone model and simulations of fractures. *Computer Methods in Applied Mechanics and Engineering*, 199(9-12):547–556, 2010.

[29] J. Qian and S. Li. Application of Multiscale Cohesive Zone Model to Simulate Fracture in Polycrystalline Solids. *Journal of Engineering Materials and Technology*, 133(1):11010, 2011.

[30] S. Li, X. Zeng, B. Ren, J. Qian, J. Zhang, and A. K. Jha. An atomistic-based interphase zone model for crystalline solids. *Computer Methods in Applied Mechanics and Engineering*, 229-232:87–109, 2012.

[31] M. He and S. Li. An embedded atom hyperelastic constitutive model and multiscale cohesive finite element method. *Computational Mechanics*, 49 (3):337–355, 2012.

[32] H. Fan and S. Li. Computational modelling of fracture in polycrystalline materials. *Gesellschaft für Angewandte Mathematik und Mechanik (GAMM)*, 38:268–284, 2015.

[33] D. Lyu, H. Fan, and S. Li. A hierarchical multiscale cohesive zone model and simulation of dynamic fracture in metals. *Engineering Fracture Mechanics*, 163:327–347, 2016.

[34] B. Devincre and R. Gatti. Physically justified models for crystal plasticity developed with dislocation dynamics simulations. *AerospaceLab*, (9):p–1, 2015.

[35] J. Kratochvil. Dislocation pattern formation in metals. *Revue de physique appliquée*, 23(4):419–429, 1988.

[36] S. Sandfeld and M. Zaiser. Pattern formation in a minimal model of continuum dislocation plasticity. *Modelling and Simulation in Materials Science and Engineering*, 23(6):065005, 2015.

[37] E.C. Aifantis. On the dynamical origin of dislocation patterns. *Materials Science and Engineering*, 81:563–574, 1986.

[38] E.C. Aifantis. *Patterns, Defects and Materials Instabilities*. Springer, 1990.

[39] E.C. Aifantis. On the gradient approach to deformation patterning and fracture. *Solid State Phenomena*, 23:355–368, 1992.

[40] J.M. Salazar, R. Fournet, and N. Banal. Dislocation patterns from reaction-diffusion models. *Acta metallurgica et materialia*, 43(3):1127–1134, 1995.

[41] A.D. Rollett and U.F. Kocks. A review of the stages of work hardening. *Solid State Phenomena*, 35:1–18, 1993.

[42] C. Schiller and D. Walgraef. Numerical simulation of persistent slip band formation. *Acta Metallurgica*, 36(3):563–574, 1988.

[43] G. Schoeck and R. Frydman. The contribution of the dislocation forest to the flow stress. *Physica status solidi (b)*, 53(2):661–673, 1972.

[44] A.A. Shtolberg. A method for computation of equilibrium dislocation configurations. *physica status solidi (b)*, 43(2):523–532, 1971.

[45] D. Walgraef, C. Schiller, and E.C. Aifantis. *Reaction-diffusion approach to dislocation patterns*. Springer, 1987.

[46] C. Buque. Dislocation structures and cyclic behaviour of [011] and [111]-oriented nickel single crystals. *International Journal of Fatigue*, 23(8):671 – 678, 2001.

[47] H. Mughrabi. Cyclic plasticity of matrix and persistent slip bands in fatigued metals. *Continuum Models of Discrete Systems*, 4(0):24l–257, 1981.

[48] H. Mughrabi. Dislocation wall and cell structures and long-range internal stresses in deformed metal crystals. *Acta metallurgica*, 31(9):1367–1379, 1983.

[49] P. Li, S. Li, Z. Wang, and Z. Zhang. Formation mechanisms of cyclic saturation dislocation patterns in [0 0 1],[0 1 1] and [$\bar{1}$11] copper single crystals. *Acta Materialia*, 58(9):3281–3294, 2010.

[50] G. Zhang, R. Schwaiger, C. Volkert, and O. Kraft. Effect of film thickness and grain size on fatigue-induced dislocation structures in cu thin films. *Philosophical Magazine Letters*, 83(8):477–483, 2003.

[51] Y. Kawasaki and T. Takeuchi. Cell structures in copper single crystals deformed in the [001] and [111] axes. *Scripta Metallurgica*, 14(2):183–188, 1980.

[52] I. Groma, M. Zaiser, and P. D. Ispánovity. Dislocation patterning in a two-dimensional continuum theory of dislocations. *Physical Review B*, 93(21):214110, 2016.

[53] A. Schwab, J. Bretschneider, C. Buque, C. Blochwitz, and C. Holste. Application of electron channelling contrast to the investigation of strain localization effects in cyclically deformed fcc crystals. *Philosophical magazine letters*, 74(6):449–454, 1996.

[54] D. Melisova, B. Weiss, and R. Stickler. Nucleation of persistent slip bands in cu single crystals under stress controlled cycling. *Scripta materialia*, 36(9):1061–1066, 1997.

[55] P. Li, S. Li, Z. Wang, and Z. Zhang. Unified factor controlling the dislocation evolution of fatigued face-centered cubic crystals. *Acta Materialia*, 129:98–111, 2017.

[56] C. Buque, J. Bretschneider, A. Schwab, and C. Holste. Effect of grain size and deformation temperature on the dislocation structure in cyclically deformed polycrystalline nickel. *Materials Science and Engineering: A*, 319:631–636, 2001.

[57] M. Brede. The brittle-to-ductile transition in silicon. *Acta Metallurgica et materialia*, 41(1):211–228, 1993.

[58] H. Matsui and H. Kimura. Anomalous {110} slip and the role of co-planar double slip in bcc metals. *Scripta Metallurgica*, 9(9):971–978, 1975.

[59] H. Matsui and H. Kimura. Anomalous {110} slip in high-purity molybdenum single crystals and its comparison with that in v(a) metals. *Materials Science and Engineering*, 24(2):247–256, 1976.

[60] V.V. Bulatov, J.F. Justo, W. Cai, and S. Yip. Kink asymmetry and multiplicity in dislocation cores. *Physical review letters*, 79(25):5042, 1997.

[61] W. Cai. *Atomistic and Mesoscale Modelling of Dislocation Mobility*. PhD dissertation, Massachusetts Institute of Technology, 2001.

[62] W. Cai, V.V. Bulatov, J. Chang, J. Li, and S. Yip. Anisotropic elastic interactions of a periodic dislocation array. *Physical Review Letters*, 86(25):5727, 2001.

[63] V.V. Bulatov and W. Cai. Nodal effects in dislocation mobility. *Physical review letters*, 89(11):115501, 2002.

[64] S. Shao, J. Wang, and A. Misra. Energy minimization mechanisms of semi-coherent interfaces. *Journal of Applied Physics*, 116(2):023508, 2014.

[65] S. Shao, J. Wang, A. Misra, and R.G. Hoagland. Spiral patterns of dislocations at nodes in (111) semi-coherent fcc interfaces. *Scientific reports*, 3:2448, 2013.

[66] S. Shao and J. Wang. Relaxation mechanisms, structure and properties of semi-coherent interfaces. *Metals*, 5(4):1887–1901, 2015.

[67] S. Shao and J. Wang. Relaxation, structure, and properties of semicoherent interfaces. *JOM*, 68(1):242–252, 2016.

[68] E. Martinez, J. Marian, A. Arsenlis, M. Victoria, and J.M. Perlado. Atomistically informed dislocation dynamics in fcc crystals. *Journal of the Mechanics and Physics of Solids*, 56(3):869–895, 2008.

[69] L.P. Kubin, G. Canova, M. Condat, B. Devincre, V. Pontikis, and Y. Bréchet. *Dislocation microstructures and plastic flow: a 3D simulation*. 1992.

[70] B. Devincre and L.P. Kubin. Mesoscopic simulations of dislocations and plasticity. *Materials Science and Engineering: A*, 234:8–14, 1997.

[71] L.P. Kubin, B. Devincre, and M. Tang. Mesoscopic modelling and simulation of plasticity in fcc and bcc crystals: Dislocation intersections and mobility. *Journal of computer-aided materials design*, 5(1):31–54, 1998.

[72] H.M. Zbib, M. Rhee, and J.P. Hirth. On plastic deformation and the dynamics of 3d dislocations. *International Journal of Mechanical Sciences*, 40(2-3):113–127, 1998.

[73] H.M. Zbib, T. de la Rubia, M. Rhee, and J.P. Hirth. 3d dislocation dynamics: stress–strain behavior and hardening mechanisms in fcc and bcc metals. *Journal of Nuclear Materials*, 276(1-3):154–165, 2000.

[74] N.M. Ghoniem and L.Z. Sun. Fast-sum method for the elastic field of three-dimensional dislocation ensembles. *Physical Review B*, 60(1):128, 1999.

[75] M. Rhee, H.M. Zbib, J.P. Hirth, H. Huang, and T. De la Rubia. Models for long-/short-range interactions and cross slip in 3d dislocation simulation of bcc single crystals. *Modelling and Simulation in Materials Science and Engineering*, 6(4):467, 1998.

[76] R. Madec, B. Devincre, and L.P. Kubin. Simulation of dislocation patterns in multislip. *Scripta materialia*, 47(10):689–695, 2002.

[77] M. Sauzay and L.P. Kubin. Scaling laws for dislocation microstructures in monotonic and cyclic deformation of fcc metals. *Progress in Materials Science*, 56(6):725–784, 2011.

[78] J. R. Munkres. *Elements of Algebraic Topology*. Perseus Publishing, 1984.

[79] A. Hatcher. *Algebraic Topology*. Tsinghau University Press, 2002.

[80] A.N. Hirani. *Discrete Exterior Calculus*. PhD thesis, California Institute of Technology, 2003.

[81] F. Meunier. Polytopal complexes: maps, chain complexes and necklaces. *Electronic Notes in Discrete Mathematics*, 31:183–188, 2008.

[82] J. Li. Atomeye: an efficient atomistic configuration viewer. *Modelling and Simulation in Materials Science and Engineering*, 11(2):173, 2003.

[83] H. Gao and P. Klein. Numerical simulation of crack growth in an isotropic solid with randomized internal cohesive bonds. *Journal of the Mechanics and Physics of Solids*, 46(2):187–218, 1998.

[84] T. J. Hughes. *The finite element method: linear static and dynamic finite element analysis*. Courier Dover Publications, 2012.

[85] S. Urata and S. Li. Higher order cauchy–born rule based multiscale cohesive zone model and prediction of fracture toughness of silicon thin films. *International Journal of Fracture*, 203(1-2):159–181, 2017.

[86] T. Belytschko, J. S.J. Ong, W. K. Liu, and J. M. Kennedy. Hourglass control in linear and nonlinear problems. *Computer Methods in Applied Mechanics and Engineering*, 43(3):251–276, 1984.

[87] M. S. Floater, G. Kós, and M. Reimers. Mean value coordinates in 3D. *Computer Aided Geometric Design*, 22:623–631, 2005.

[88] M. S. Floater. Mean value coordinates. *Computer Aided Geometric Design*, 20(1):19–27, 2003.

[89] B. L. Holian. Fracture simulations using large-scale molecular dynamics. *Physical Review B*, 51(17):11275, 1995.

[90] M.S. Daw and M.I. Baskes. Embedded-atom method: Derivation and application to impurities, surfaces, and other defects in metals. *Physical Review B*, 29:6443, 1984.

[91] M. M. Choy, W. R. Cook, R.F.S. Hearmon, J. Jaff, J. Jerphagnon, S. K. Kurtz, S.T. Liu, and D. F. Nelson. *Group III: Crystal and Solid State Physics, Elastic, Piezoelectric, Pyroelectric, Piezooptic, Electrooptic Constants, and Nonlinear Dielectric Susceptibilities of Crystals*. Springer-Verlag Berlin, 1971.

[92] C. Talischi, G. H. Paulino, and C. H. Le. Honeycomb Wachspress finite elements for structural topology optimization. *Structural and Multidisciplinary Optimization*, 37(6):569–583, 2008.

[93] J.N. Lyness and G. Monegato. Quadrature rules for regions having regular hexagonal symmetry. *SIAM Journal on Numerical Analysis*, 14(2), 1977.

[94] L. B. Freund. *Dynamic fracture mechanics*. Cambridge university press, 1998.

[95] C. Linder and F. Armero. Finite elements with embedded branching. *Finite Elements in Analysis and Design*, 45(4):280–293, 2009.

[96] F. Armero and C. Linder. Numerical simulation of dynamic fracture using finite elements with embedded discontinuities. *International Journal of Fracture*, 160(2):119, 2009.

[97] M.L. Falk, A. Needleman, and J.R. Rice. A critical evaluation of cohesive zone models of dynamic fractur. *Le Journal de Physique IV*, 11(PR5):Pr5–43, 2001.

[98] T. Zhu, J. Li, K. J. Van Vliet, S. Ogata, S. Yip, and S. Suresh. Predictive modeling of nanoindentation-induced homogeneous dislocation nucleation in copper. *Journal of the Mechanics and Physics of Solids*, 52(3):691–724, 2004.

[99] Y. Zhong and T. Zhu. Simulating nanoindentation and predicting dislocation nucleation using interatomic potential finite element method. *Computer Methods in Applied Mechanics and Engineering*, 197:3174–3181, 2008.

[100] Y. Mishin, M. J. Mehl, D. A. Papaconstantopoulos, A. F. Voter, and J. D. Kress. Structural stability and lattice defects in copper: Ab initio, tight-binding, and embedded-atom calculations. *Physical Review B*, 63(22):224106, 2001.

[101] H. Fan and S. Li. A three-dimensional surface formulation for adhesive contact in finite deformation. *International Journal for Numerical Methods in Engineering*, 107:252–270, 2015.

[102] H. Fan. *A multiscale moving contact line theory and its applications on the simulations of dynamic droplet wetting and cell motility on soft substrates*. PhD dissertation, University of California, Berkeley, 2014.

[103] S. Plimpton. Fast parallel algorithms for short-range molecular dynamics. *Journal of computational physics*, 117:1–42, 1995.

[104] C. L. Kelchner. Dislocation nucleation and defect structure during surface indentation. *Phys. Rev. B*, 58(17):85–88, 1998.

[105] L. Xiong, D. L. McDowell, and Y. Chen. Nucleation and growth of dislocation loops in cu, al and si by a concurrent atomistic-continuum method. *Scripta Materialia*, 67:633–636, 2012.

[106] J.P. Hirth and J. Lothe. *Theory of Dislocations*. Krieger Publishing Company, 1982.

[107] M.A. Tschopp and D.L. Mcdowell. Influence of single crystal orientation on homogeneous dislocation nucleation under uniaxial loading. *Journal of the Mechanics and Physics of Solids*, 56:1806–1830, 2008.

[108] M.A. Tschopp and D.L. Mcdowell. Tension-compression asymmetry in homogeneous dislocation nucleation in single crystal copper. *Applied physics letters*, 90(12):121916, 2007.

[109] I. Salehinia and D.F. Bahr. Crystal orientation effect on dislocation nucleation and multiplication in FCC single crystal under uniaxial loading. *International Journal of Plasticity*, 52:133–146, 2014.

[110] R.O. Scattergood and D.J. Bacon. The strengthening effect of voids. *Acta Metallurgica*, 30(8):1665–1677, 1982.

[111] A. Ramasubramaniam, M.P. Ariza, and M. Ortiz. A discrete mechanics approach to dislocation dynamics in bcc crystals. *Journal of the Mechanics and Physics of Solids*, 55(3):615–647, 2007.

[112] X. Liu, J. Gu, Y. Shen, J. Li, and C. Chen. Lattice dynamical finite-element method. *Acta Materialia*, 58:510–523, 2010.

[113] J.D. Clayton. *Nonlinear Mechanics of Crystals*. Springer, Dordrecht, 2011.

[114] L. Liu and S. Li. A Finite Temperature Multiscale Interphase Zone Model and Simulations of Fracture. *Journal of Engineering Materials and Technology*, 134(3):31014, 2012.

[115] N. Rivier and A. Lawrence. Quasicrystals at grain boundaries. *Physica B+ C*, 150(1-2):190–202, 1988.

[116] S. Urata and S. Li. A multiscale model for amorphous materials. *Computational Materials Science*, 135:64–77, 2017.

[117] L. Liu and S. Li. *Multiscale Simulations and Mechanics of Biological Materials*. John Wiley Sons Ltd, 2013.

Appendix A

Derivatives of the Six-node Honeycomb Wachspress Shape Function

In this appendix, the third order derivatives of the six-node honeycomb Wachspress shape function are provided. For the first order and second order derivatives of the six-node honeycomb Wachspress shape function, the readers may consult [117].

$$\begin{aligned}\frac{\partial^3 N_1}{\partial \xi^3} =& -2h(\xi,\eta)\eta[-9+4\eta^2)(9\sqrt{3}+\sqrt{3}\eta^4+36\xi-4\eta^3\xi+18\sqrt{3}\xi^2\\ &+12\xi^3+\sqrt{3}\xi^4+4\eta\xi(3+\xi^2)-6\eta^2(\sqrt{3}+2\xi+\sqrt{3}\xi^2)]\end{aligned}$$

$$\begin{aligned}\frac{\partial^3 N_1}{\partial \xi^2\eta} =& 2h(\xi,\eta)[4\eta^4(1+\sqrt{3}\xi)-2\eta^5(-5+8\xi^2)-18\eta(-3-2\xi^2+\xi^4)\\ &-3(-3+\xi^2)(9+9\sqrt{3}\xi+9\xi^2+\sqrt{3}\xi^3)+16\eta^3(-3+\xi^2+\xi^4)\\ &+\eta^2(-54-54\sqrt{3}\xi+90\xi^2+66\sqrt{3}\xi^3+36\xi^4+4\sqrt{3}\xi^5)\\ &-\eta^4(3+3\sqrt{3}\xi+56\xi^2+24\sqrt{3}\xi^3)]\end{aligned}$$

$$\begin{aligned}\frac{\partial^3 N_1}{\partial \xi\eta^2} =& -2h(\xi,\eta)[16\eta^2\xi^3(-3+\xi^2)-6\xi(-3+\xi^2)(-3+\xi^2)\\ &+\eta^4(30\xi-16\xi^3)+\eta^3(-6\sqrt{3}+84\xi+38\sqrt{3}\xi^2-64\xi^3-24\sqrt{3}\xi^4)\\ &+\eta(-3+\xi^2)(-9\sqrt{3}+36\xi+27\sqrt{3}\xi^2+24\xi^3+4\sqrt{3}\xi^4)\\ &+\eta^5(-\sqrt{3}+8\xi+4\sqrt{3}\xi^2)]\end{aligned}$$

$$\begin{aligned}\frac{\partial^3 N_1}{\partial \eta^3} =& 2h(\xi,\eta)(-3+4\xi^2)[\eta^4(3+\sqrt{3}\xi)-4\eta^3(-3+\xi^2)\\ &+4\eta(-3+\xi^2)(-3+\xi^2)+(3+\sqrt{3}\xi)(-3+\xi^2)(-3+\xi^2)\\ &-6\eta^2(3+\sqrt{3}\xi)(-3+\xi^2)]\end{aligned}$$

$$\frac{\partial^3 N_2}{\partial \xi^3} = -h(\xi,\eta)[(8\eta(-3+2\eta)(3+2\eta)(3+2\eta)\xi(-3+\eta^2-\xi^2)]$$

$$\begin{aligned}\frac{\partial^3 N_2}{\partial \xi^2 \eta} =& -2h(\xi,\eta)(3+2\eta)[2\eta^5+\eta^4(7-16\xi^2)-4\eta^3(3+\xi^2)\\ &-9(-3-2\xi^2+\xi^4)-6\eta(-3-2\xi^2+\xi^4)\\ &+2\eta^2(-15+11\xi^2+8\xi^4)]\end{aligned}$$

$$\begin{aligned}\frac{\partial^3 N_2}{\partial \xi \eta^2} =& 8h(\xi,\eta)\xi[2\eta^5+\eta^3(21-16\xi^2)+\eta^4(15-8\xi^2)+8\eta^2\xi^2(-3+\xi^2)\\ &-3(-3+\xi^2)(-3+\xi^2)+3\eta(-9-3\xi^2+2\xi^4)]\end{aligned}$$

$$\begin{aligned}\frac{\partial^3 N_2}{\partial \eta^3} =& -h(\xi,\eta)[(2(-3+4\xi^2)(3\eta^4-18\eta^2(-3+\xi^2)-8\eta^3(-3+\xi^2)\\ &+3(-3+\xi^2)(-3+\xi^2)+8\eta(-3+\xi^2)(-3+\xi^2)]\end{aligned}$$

$$\begin{aligned}\frac{\partial^3 N_3}{\partial \xi^3} =& 2h(\xi,\eta)\eta(-9+4\eta^2)[9\sqrt{3}+\sqrt{3}\eta^4-36\xi+4\eta^3\xi+18\sqrt{3}\xi^2\\ &-12\xi^3+\sqrt{3}\xi^4-4\eta\xi(3+\xi^2)-6\eta^2(\sqrt{3}-2\xi+\sqrt{3}\xi^2)]\end{aligned}$$

$$\begin{aligned}\frac{\partial^3 N_3}{\partial \xi^2 \eta} =& -2h(\xi,\eta)[4\eta^4(-1+\sqrt{3}\xi)+2\eta^5(-5+8\xi^2)+18\eta(-3-2\xi^2+\xi^4)\\ &+\eta^2(54-54\sqrt{3}\xi-90\xi^2+66\sqrt{3}\xi^3-36\xi^4+4\sqrt{3}\xi^5)\\ &-3(-3+\xi^2)(-9+9\sqrt{3}\xi-9\xi^2+\sqrt{3}\xi^3)\\ &+\eta^4(3-3\sqrt{3}\xi+56\xi^2-24\sqrt{3}\xi^3)-16\eta^3(-3+\xi^2+\xi^4)]\end{aligned}$$

$$\begin{aligned}\frac{\partial^3 N_3}{\partial \xi \eta^2} =& 2h(\xi,\eta)[-16\eta^2\xi^3(-3+\xi^2)+6\xi(-3+\xi^2)(-3+\xi^2)\\ &+\eta^3(-6\sqrt{3}-84\xi+38\sqrt{3}\xi^2+64\xi^3-24\sqrt{3}\xi^4)\\ &+\eta(-3+\xi^2)(-9\sqrt{3}-36\xi+27\sqrt{3}\xi^2-24\xi^3+4\sqrt{3}\xi^4)\\ &+2\eta^4\xi(-15+8\xi^2)+\eta^5(-\sqrt{3}-8\xi+4\sqrt{3}\xi^2)]\end{aligned}$$

$$\begin{aligned}\frac{\partial^3 N_3}{\partial \eta^3} =& -2h(\xi,\eta)(-3+4\xi^2)[\eta^4(-3+\sqrt{3}\xi)+4\eta^3(-3+\xi^2)\\ &-4\eta(-3+\xi^2)(-3+\xi^2)+(-3+\sqrt{3}\xi)(-3+\xi^2)(-3+\xi^2)\\ &-6\eta^2(-3+\sqrt{3}\xi)(-3+\xi^2)]\end{aligned}$$

$$\begin{aligned}\frac{\partial^3 N_4}{\partial \xi^3} =& -2h(\xi,\eta)\eta(-9+4\eta^2)[9\sqrt{3}+\sqrt{3}\eta^4-36\xi-4\eta^3\xi+18\sqrt{3}\xi^2\\ &-12\xi^3+\sqrt{3}\xi^4+4\eta\xi(3+\xi^2)-6\eta^2(\sqrt{3}-2\xi+\sqrt{3}\xi^2)]\end{aligned}$$

$$\begin{aligned}\frac{\partial^3 N_4}{\partial\xi^2\eta} =& 2h(\xi,\eta)(4\eta^4[-1+\sqrt{3}\xi) - 2\eta^5(-5+8\xi^2) - 18\eta(-3-2\xi^2+\xi^4)\\ &- 3(-3+\xi^2)(-9+9\sqrt{3}\xi-9\xi^2+\sqrt{3}\xi^3) + 16\eta^3(-3+\xi^2+\xi^4)\\ &+ \eta^2(54-54\sqrt{3}\xi-90\xi^2+66\sqrt{3}\xi^3-36\xi^4+4\sqrt{3}\xi^5)\\ &+ \eta^4(3-3\sqrt{3}\xi+56\xi^2-24\sqrt{3}\xi^3)]\end{aligned}$$

$$\begin{aligned}\frac{\partial^3 N_4}{\partial\xi\eta^2} =& -2h(\xi,\eta)[-16\eta^2\xi^3(-3+\xi^2) - 6\xi(-3+\xi^2)(-3+\xi^2)\\ &+ \eta^4(30\xi-16\xi^3) + \eta^3(-6\sqrt{3}-84\xi+38\sqrt{3}\xi^2+64\xi^3-24\sqrt{3}\xi^4)\\ &+ \eta(-3+\xi^2)(-9\sqrt{3}-36\xi+27\sqrt{3}\xi^2-24\xi^3+4\sqrt{3}\xi^4)\\ &+ \eta^5(-\sqrt{3}-8\xi+4\sqrt{3}\xi^2)]\end{aligned}$$

$$\begin{aligned}\frac{\partial^3 N_4}{\partial\eta^3} =& 2h(\xi,\eta)(-3+4\xi^2)[\eta^4(-3+\sqrt{3}\xi) - 4\eta^3(-3+\xi^2)\\ &+ 4\eta(-3+\xi^2)(-3+\xi^2) + (-3+\sqrt{3}\xi)(-3+\xi^2)(-3+\xi^2)\\ &- 6\eta^2(-3+\sqrt{3}\xi)(-3+\xi^2)]\end{aligned}$$

$$\frac{\partial^3 N_5}{\partial\xi^3} = -h(\xi,\eta)[(8(3-2\eta)(3-2\eta)\eta(3+2\eta)\xi(-3+\eta^2-\xi^2)]$$

$$\begin{aligned}\frac{\partial^3 N_5}{\partial\xi^2\eta} =& 2h(\xi,\eta)(-3+2\eta)[2\eta^5 - 4\eta^3(3+\xi^2) + \eta^4(-7+16\xi^2)\\ &- 6\eta(-3-2\xi^2+\xi^4) - 2\eta^2(-15+11\xi^2+8\xi^4)\\ &+ 9(-3-2\xi^2+\xi^4)]\end{aligned}$$

$$\begin{aligned}\frac{\partial^3 N_5}{\partial\xi\eta^2} =& 8h(\xi,\eta)\xi[-2\eta^5 + \eta^4(15-8\xi^2) - 3(-3+\xi^2)(-3+\xi^2)\\ &+ \eta^3(-21+16\xi^2) + \eta(27+9\xi^2-6\xi^4)\\ &+ 8\eta^2\xi^2(-3+\xi^2)]\end{aligned}$$

$$\begin{aligned}\frac{\partial^3 N_5}{\partial\eta^3} =& 2h(\xi,\eta)[(-3+4\xi^2)(3\eta^4 - 18\eta^2(-3+\xi^2) + 8\eta^3(-3+\xi^2)\\ &+ 3(-3+\xi^2)(-3+\xi^2) - 8\eta(-3+\xi^2)(-3+\xi^2)]\end{aligned}$$

$$\begin{aligned}\frac{\partial^3 N_6}{\partial\xi^3} =& 2h(\xi,\eta)\eta(-9+4\eta^2)[9\sqrt{3}+\sqrt{3}\eta+36\xi+4\eta^3\xi+18\sqrt{3}\xi^2\\ &- 4\eta\xi(3+\xi^2) - 6\eta^2(\sqrt{3}+2\xi+\sqrt{3}\xi^2) + 12\xi^3+\sqrt{3}\xi^4]\end{aligned}$$

$$\begin{aligned}
\frac{\partial^3 N_6}{\partial \xi^2 \eta} =& -2h(\xi,\eta)[4\eta^4(1+\sqrt{3}\xi)+2\eta^5(-5+8\xi^2)+36\xi^4+4\sqrt{3}\xi^5) \\
&-\eta^4(3+3\sqrt{3}\xi+56\xi^2+24\sqrt{3}\xi^3)+18\eta(-3-2\xi^2+\xi^4) \\
&-16\eta^3(-3+\xi^2+\xi^4)-3(-3+\xi^2)(9+9\sqrt{3}\xi+9\xi^2+\sqrt{3}\xi^3) \\
&+\eta^2(-54-54\sqrt{3}\xi+90\xi^2+66\sqrt{3}\xi^3] \\
\frac{\partial^3 N_6}{\partial \xi \eta^2} =& 2h(\xi,\eta)[-16\eta^2\xi^3(-3+\xi^2)+6\xi(-3+\xi^2)(-3+\xi^2)+4\sqrt{3}\xi^2) \\
&+\eta^3(-6\sqrt{3}+84\xi+38\sqrt{3}\xi^2-64\xi^3-24\sqrt{3}\xi^4) \\
&+\eta(-3+\xi^2)(-9\sqrt{3}+36\xi+27\sqrt{3}\xi^2+24\xi^3+4\sqrt{3}\xi^4) \\
&+\eta^5(-\sqrt{3}+8\xi+2\eta^4\xi(-15+8\xi^2)] \\
\frac{\partial^3 N_6}{\partial \eta^3} =& -2h(\xi,\eta)(-3+4\xi^2)[\eta^4(3+\sqrt{3}\xi)+4\eta^3(-3+\xi^2) \\
&-4\eta(-3+\xi^2)(-3+\xi^2)+(3+\sqrt{3}\xi)(-3+\xi^2)(-3+\xi^2) \\
&-6\eta^2(3+\sqrt{3}\xi)(-3+\xi^2)],
\end{aligned}$$

where $h(\xi,\eta)=\frac{1}{3}(\xi^2+\eta^2-3)^{-4}$.

Appendix B

Derivatives of Shape Functions

In this appendix, the higher order Cauchy-Born rule in the Finite Element Method is discussed. The first, second and third order derivative of shape functions are derived.

B.1 The First Order Derivative of Shape Functions

By using the chain rule, the first order derivative of shape functions with respect to the natural coordinates ξ in index notation can be written as

$$\frac{\partial N_I}{\partial \xi_i} = \frac{\partial N_I}{\partial X_j}\frac{\partial X_j}{\partial \xi_i} \tag{B.1}$$

Thus

$$\frac{\partial N_I}{\partial X_j} = \frac{\partial N_I}{\partial \xi_i}\frac{\partial \xi_i}{\partial X_j} \tag{B.2}$$

where

$$\frac{\partial \xi_i}{\partial X_j} = J^{-1}_{ji} \tag{B.3}$$

and the Jacobian matrix **J** is

$$J_{ij} = \sum_{J}^{nnode} \frac{\partial N^J}{\partial \xi_j} X_i^J \tag{B.4}$$

B.2 The Second Order Derivative of Shape Functions

Similarly, the second order derivative of shape functions with respect to the natural coordinates ξ can be expressed as

$$\frac{\partial^2 N_I}{\partial \xi_i \partial \xi_j} = \frac{\partial^2 N_I}{\partial X_m \partial X_k}\frac{\partial X_m}{\partial \xi_i}\frac{\partial X_k}{\partial \xi_j} + \frac{\partial N_I}{\partial X_l}\frac{\partial^2 X_l}{\partial \xi_i \partial \xi_j} \tag{B.5}$$

Thus

$$\frac{\partial^2 N_I}{\partial X_m \partial X_k} = (\frac{\partial^2 N_I}{\partial \xi_i \partial \xi_j} - \frac{\partial N_I}{\partial X_l}\frac{\partial^2 X_l}{\partial \xi_i \partial \xi_j})\frac{\partial \xi_i}{\partial X_m}\frac{\partial \xi_j}{\partial X_k} \tag{B.6}$$

where

$$\frac{\partial^2 X_l}{\partial \xi_i \partial \xi_j} = \sum_J^{nnode} \frac{\partial^2 N^J}{\partial \xi_i \partial \xi_j} X_l^J \tag{B.7}$$

B.3 The Third Order Derivative of Shape Functions

Similarly, the third order derivative of shape functions with respect to the natural coordinates ξ can be expressed as

$$\begin{aligned}\frac{\partial^3 N_I}{\partial \xi_i \partial \xi_j \partial \xi_k} = &\frac{\partial^3 N_I}{\partial X_n \partial X_m \partial X_l}\frac{\partial X_n}{\partial \xi_i}\frac{\partial X_m}{\partial \xi_j}\frac{\partial X_k}{\partial \xi_k} + \frac{\partial^2 N_I}{\partial X_m \partial X_l}\frac{\partial^2 X_m}{\partial \xi_i \partial \xi_j}\frac{\partial X_l}{\partial \xi_k} + \frac{\partial^2 N^I}{\partial X_m \partial X_l}\frac{\partial X_m}{\partial \xi_j}\frac{\partial^2 X_l}{\partial \xi_i \partial \xi_k} \\ &+ \frac{\partial^2 N^I}{\partial X_n \partial X_m}\frac{\partial X_n}{\partial \xi_i}\frac{\partial^2 X_m}{\partial \xi_j \partial \xi_k} + \frac{\partial N^I}{\partial X_m}\frac{\partial^3 X_m}{\partial \xi_i \partial \xi_j \partial \xi_k}\end{aligned} \tag{B.8}$$

Thus

$$\begin{aligned}\frac{\partial^3 N_I}{\partial X_i \partial X_j \partial X_k} = &\frac{\partial^3 N_I}{\partial \xi_i \partial \xi_j \partial \xi_k}\frac{\partial \xi_n}{\partial X_i}\frac{\partial \xi_m}{\partial X_j}\frac{\partial \xi_l}{\partial X_k} - \frac{\partial^2 N_I}{\partial \xi_l \partial \xi_k}\frac{\partial^2 X_l}{\partial \xi_n \xi_m}\frac{\partial \xi_n}{\partial X_i}\frac{\partial \xi_m}{\partial X_j} \\ &- \frac{\partial^2 N_I}{\partial \xi_j \partial \xi_m}\frac{\partial^2 X_m}{\partial \xi_n \xi_l}\frac{\partial \xi_n}{\partial X_i}\frac{\partial \xi_l}{\partial X_k} - \frac{\partial^2 N_I}{\partial \xi_i \partial \xi_n}\frac{\partial^2 X_n}{\partial \xi_m \xi_l}\frac{\partial \xi_m}{\partial X_j}\frac{\partial \xi_l}{\partial X_k} \\ &- \frac{\partial N_I}{\partial X_o}\frac{\partial^3 X_o}{\partial \xi_n \xi_m \xi_l}\frac{\partial \xi_n}{\partial X_i}\frac{\partial \xi_m}{\partial X_j}\frac{\partial \xi_l}{\partial X_k}\end{aligned} \tag{B.9}$$

where

$$\frac{\partial^3 X_o}{\partial \xi_n \partial \xi_m \partial \xi_l} = \sum_J^{nnode} \frac{\partial^3 N^J}{\partial \xi_n \partial \xi_m \partial \xi_l} X_o^J \tag{B.10}$$

Appendix C

Finite Element Interpolation Functions for Rhombic Dodecahedron

In this appendix, the shape functions of the 14-node rhombic dodecahedron are provided. The shape function λ_i for node i is defied by

$$\lambda_i = \frac{w_i}{\sum_{j=1}^{14} w_j}$$

where the weight function w_i is given by

$$w_i = \frac{1}{r_i} \sum_{T \ni \mathbf{v}_i} \mu_{i,T} \ ,$$

in which $\mu_{i,T}$ is defined as

$$\mu_{i,T} = \frac{\beta_{jk} + \beta_{ij}\mathbf{n}_{ij} \cdot \mathbf{n}_{jk} + \beta_{ki}\mathbf{n}_{ki} \cdot \mathbf{n}_{jk}}{2\mathbf{e}_i \cdot \mathbf{n}_{jk}}$$

The coordinates of 14 nodes in the reference coordinates are given in Table C.1

Table C.1: Coordinates of 14 nodes in the reference coordinates

Node	ξ	η	ζ
1	0.25	0.25	0.25
2	-0.25	0.25	0.25
3	0.25	-0.25	0.25
4	-0.25	-0.25	0.25
5	0.25	0.25	-0.25
6	-0.25	0.25	-0.25
7	0.25	-0.25	-0.25
8	-0.25	-0.25	-0.25
9	0.0	0.0	0.5
10	0.0	0.0	-0.5
11	0.0	0.5	0.0
12	0.0	-0.5	0.0
13	0.5	0.0	0.5
14	-0.5	0.0	0.5

The vector between the i^{th} node with the Gaussian point (ξ, η, ζ) is given by

$$\mathbf{r}_i = [\xi_i - \xi, \eta_i - \eta, \zeta_i - \zeta]$$

with

$$r_i = \sqrt{(\xi_i - \xi)^2 + (\eta_i - \eta)^2 + (\zeta_i - \zeta)^2}$$

where ξ_i, η_i, ζ_i denote the coordinates of i^{th} node as shown in Table C.1.

$$\beta_{ij} = \arccos\left[\frac{(\xi_i - \xi)(\xi_j - \xi) + (\eta_i - \eta)(\eta_j - \eta) + (\zeta_i - \zeta)(\zeta_j - \zeta)}{\mathbf{r}_i \cdot \mathbf{r}_j}\right]$$

$$\beta_{jk} = \arccos\left[\frac{(\xi_j - \xi)(\xi_k - \xi) + (\eta_j - \eta)(\eta_k - \eta) + (\zeta_j - \zeta)(\zeta_k - \zeta)}{\mathbf{r}_j \cdot \mathbf{r}_k}\right]$$

$$\beta_{ki} = \arccos\left[\frac{(\xi_k - \xi)(\xi_i - \xi) + (\eta_k - \eta)(\eta_i - \eta) + (\zeta_k - \zeta)(\zeta_i - \zeta)}{\mathbf{r}_k \cdot \mathbf{r}_i}\right]$$

$$\mathbf{e}_i = \frac{[\xi_i - \xi, \eta_i - \eta, \zeta_i - \zeta]}{r_i}$$

$$\begin{aligned}\mathbf{n}_{ij} = [&- \eta_i\zeta + \eta_j\zeta + \eta\zeta_i - \eta_j\zeta_i - \eta\zeta_j + \eta_i\zeta_j, \\ &\xi_i\zeta - \xi_j\zeta - \xi\zeta_i + \xi_j\zeta_i + \xi\zeta_j - \xi_i\zeta_j, \\ &- \xi_i\eta + \xi_j\eta + \xi\eta_i - \xi_j\eta_i - \xi\eta_j + \xi_i\eta_j]/L_{ij}\end{aligned}$$

with

$$\begin{aligned} L_{ij} =& \sqrt{((-\xi_i\eta + \xi_j\eta + \xi\eta_i - \xi_j\eta_i - \xi\eta_j + \xi_i\eta_j)^2} \\ &+ (\xi_i\zeta - \xi_j\zeta - \xi\zeta_i + \xi_j\zeta_i + \xi\zeta_j - \xi_i\zeta_j)^2 \\ &+ (-\eta_i\zeta + \eta_j\zeta + \eta\zeta_i - \eta_j\zeta_i - \eta\zeta_j + \eta_i\zeta_j)^2) \end{aligned}$$

Similarly,

$$\begin{aligned} \mathbf{n}_{jk} = [&- \eta_j\zeta + \eta_k\zeta + \eta\zeta_j - \eta_k\zeta_j - \eta\zeta_k + \eta_j\zeta_k, \\ &\xi_j\zeta - \xi_k\zeta - \xi\zeta_j + \xi_k\zeta_j + \xi\zeta_k - \xi_j\zeta_k, \\ &- \xi_j\eta + \xi_k\eta + \xi\eta_j - \xi_k\eta_j - \xi\eta_k + \xi_j\eta_k]/L_{jk} \end{aligned}$$

with

$$\begin{aligned} L_{jk} =& \sqrt{((-\xi_j\eta + \xi_k\eta + \xi\eta_j - \xi_k\eta_j - \xi\eta_k + \xi_j\eta_k)^2} \\ &+ (\xi_j\zeta - \xi_k\zeta - \xi\zeta_j + \xi_k\zeta_j + \xi\zeta_k - \xi_j\zeta_k)^2 \\ &+ (-\eta_j\zeta + \eta_k\zeta + \eta\zeta_j - \eta_k\zeta_j - \eta\zeta_k + \eta_j\zeta_k)^2) \end{aligned}$$

$$\begin{aligned} \mathbf{n}_{ki} = [&- \eta_k\zeta + \eta_i\zeta + \eta\zeta_k - \eta_i\zeta_k - \eta\zeta_i + \eta_k\zeta_i, \\ &\xi_k\zeta - \xi_i\zeta - \xi\zeta_k + \xi_i\zeta_k + \xi\zeta_i - \xi_k\zeta_i, \\ &- \xi_k\eta + \xi_i\eta + \xi\eta_k - \xi_i\eta_k - \xi\eta_i + \xi_k\eta_i]/L_{ki}, \end{aligned}$$

with

$$\begin{aligned} L_{ki} =& \sqrt{((-\xi_k\eta + \xi_i\eta + \xi\eta_k - \xi_i\eta_k - \xi\eta_i + \xi_k\eta_i)^2} \\ &+ (\xi_k\zeta - \xi_i\zeta - \xi\zeta_k + \xi_i\zeta_k + \xi\zeta_i - \xi_k\zeta_i)^2 \\ &+ (-\eta_k\zeta + \eta_i\zeta + \eta\zeta_k - \eta_i\zeta_k - \eta\zeta_i + \eta_k\zeta_i)^2) \ . \end{aligned}$$